Experimental Investigation of Near-well Fluid Mechanics on the Scaling Mechanism in Narrow Rectangular Slots

by

Pavan Kamble

A thesis submitted in partial fulfillment of the requirements for the degree of

Master of Science

Department of Mechanical Engineering
University of Alberta

ABSTRACT

This experimental study investigates the effect of near-well fluid mechanics on the scaling failure mechanism specific to SAGD production well. The scaling failure mechanism can be triggered by the pressure drop phenomenon and causes the plugging of the slots in the oilfields. The scale formation process has been previously studied to understand the effect of thermodynamic parameters. However, there are very few studies which tried to understand the effect of flow related aspects on the scale formation. Also, an image acquisition system has been rarely used in a dynamic flow and in-situ conditions to monitor the calcium carbonate scale growth, and investigate the pressure loss characteristics. An experimental set-up was developed to simulate the formation and growth of the calcium carbonate as well as to visualize the flow related phenomenon in the narrow rectangular slot. To undertake this, two experimental measurements are needed. Monitoring the growth of the calcium carbonate and measure the subsequent changes in differential pressure during the scaling experiment, and determination of the pressure field from the velocity data using particle shadowgraph velocimetry technique. The experimental set-up mimics the flow through a single rectangular slot of the actual slotted liner design used in SAGD.

The scaling performances of industrial slotted liner designs i.e. straight, seamed and keystone were investigated to understand their efficacy in mitigating the scaling issues. The slot width reduces due to calcium carbonate scale formation and subsequent crystal growth. The scale growth is concentrated at the slot entrance

where there is a change to a low pressure region. Based on the comparison of the geometries, the keystone design is a superior design to mitigate the scale problems. The study hypothesizes that the cycle of calcium carbonate growth and pressure drop continues until the plugging of the slots. The effect of inlet geometry profile was also assessed on the calcium carbonate scale formation and growth by considering a straight channel with and without a rounded entrance. The flow developed slowly for the rounded slot design indicating a reduction in flow resistance. The pressure loss characteristics for the straight and rounded design were also investigated. The study confirmed that the gradual change at the entrance by rounding the sharp edges reduces the tendency for scaling. Also, an increase in the flow rate in both geometries accelerated the scale formation process. The scale formation and growth mechanism affected the static pressure loss due to a subsequent increase in the kinetic energy and flow convergence.

PREFACE

This thesis is an original work by Pavan Kamble. Part of Chapter 4 have been published as Kamble, P., Ansari, S. and Nobes, D.S. (2019) 'Prediction of the calcium carbonate growth rate in a vertical slot due to the effect of pressure drop' in 13th International Symposium on Particle Image Velocimetry – ISPIV 2019, Munich, Germany, July 22-24, 2019 and presented as Kamble, P. and Nobes, D.S. (2019) 'Investigation of the effect of pressure drop on calcium carbonate deposition rate in a vertical slot' at Proceedings of the 4th Thermal and Fluid Engineering Conference, TFEC-2019-28079, Las Vegas, USA, April 14-17, 2019.

This dissertation is dedicated to my mom, late grandma and to all my family members.

“It is not the mountain we conquer, but ourselves”

- Sir Edmund Hillary

ACKNOWLEDGEMENTS

My research experience has been very gratifying and I would like to thank number of people without whom this work was not possible during my MSc studies.

First of all, I am very grateful to my supervisor Professor David S. Nobes. I would like to thank him for all the help, knowledge and support. His enthusiasm for achieving higher goals has given me the inspiration to aim for the best. I will also continue to benefit from his mentorship in my future career.

I have been very fortunate to work with awesome colleagues. I would like to thank Yishak Yusuf for his help in establishing pressure measurement set-up, Reza Azhadi and Shadi Ansari for the pressure code, David Miller for the acrylic windows slot milling and Lisa Kinsale for the help with the thesis formatting and useful tips. They also provided important suggestions from time to time.

I take this opportunity to thank mechanical engineering officials and machine shop technicians for their timely help and support.

I would like to thank my family members for their unconditional love and support. They have always inspired and never stopped me from pursuing my goals, and I will forever be grateful to them.

I gratefully acknowledge the financial support from RGL reservoir management, and Natural Sciences and Research Council (NSERC) of Canada.

TABLE OF CONTENTS

LIST OF TABLES

LIST OF FIGURES

LIST OF SYMBOLS AND ACRONYMS

Symbol/Acronyms	Description	Unit
d	Slot depth	mm
ΔP	Pressure drop	kPa
D_h	Hydraulic diameter	mm
d_p	Diameter of tracer particles	mm
EOR	Enhanced oil recovery	-
FOV	Field of view	mm × mm
g	Gravity	m/s^2
ICP-MS	Inductively coupled plasma mass spectrometry	-
h_L	Head loss	m
K	Loss coefficient	-
K_{sp}	Solubility product constant	-
L	Slot length	mm
L_e	Entrance length	mm
L_{max}	Local intensity maximum	-
L_{min}	Local intensity minimum	-
N	Sample size	-
p	Static pressure	kPa
PSV	Particle shadow velocimetry	-
PIV	Particle image velocimetry	-
Q	Flow rate	ml/hr
QCM	Quartz crystal microbalance	-

Re	Reynolds number	-
SAGD	Steam Assisted gravity drainage	-
SD	Standard deviation	-
$s_{\bar{x}}$	Standard error	-
t_s	Scaling time	hrs
SR	Saturation ratio	-
V	Fluid velocity	mm/s
v_s	Settling velocity	mm/s
V_{theory}	Theoretical velocity	mm/s
w_o	Original width at t=0	mm
w_{oi}	Original width at the inlet	mm
$w(t)$	Width in current time	mm
x	Horizontal dimension	mm
y	Vertical dimension	mm
Z	Elevation datum	mm
	Greek letters	
θ	Contact angle	Degrees
σ	Interfacial energy	N/m
μ	Fluid viscosity	Pa.s
ρ	Density	Kg/m^3
β	Geometry contraction ratio	-

1 INTRODUCTION

1.1 Steam Assisted Gravity Drainage (SAGD)

Alberta province of Canada holds the third largest reserve of oil with a production estimate of about 1.7 to 2.5 trillion barrels [1], and are only accessible by surface mining and in-situ techniques [2]. However, 80% of the oil sands cannot be extracted using conventional method of surface mining [2]. In 1978, Butler [3] developed an unconventional in-situ method known as steam assisted gravity drainage (SAGD) to produce bitumen from the oil sands. The SAGD method was successfully deployed in Athabasca oil sands by year 1997. It is a thermal injection based enhanced oil recovery (EOR) method as it utilizes the principle of latent heat exchange [4]. The other two primary techniques of EOR are, gas injection and chemical injection.

In SAGD technology, two horizontal wells are drilled parallel to each other at an approximate depth of 400 m as shown in Figure 1. The two wells are 750-1000 m in length having a vertical distance of 5 m in between them. The hot steam is continuously injected in upper injection well at high pressure which subsequently heats and increases the mobility of bitumen. As a result, the viscosity of bitumen reduces from ~1 million centipoises at ambient reservoir conditions to 10 centipoise at 200 °C. Under the influence of gravity, this lower viscosity bitumen flows into the lower production well through narrow rectangular slots. It is then pumped upwards on ground for the purpose of storage and transport [2–6].

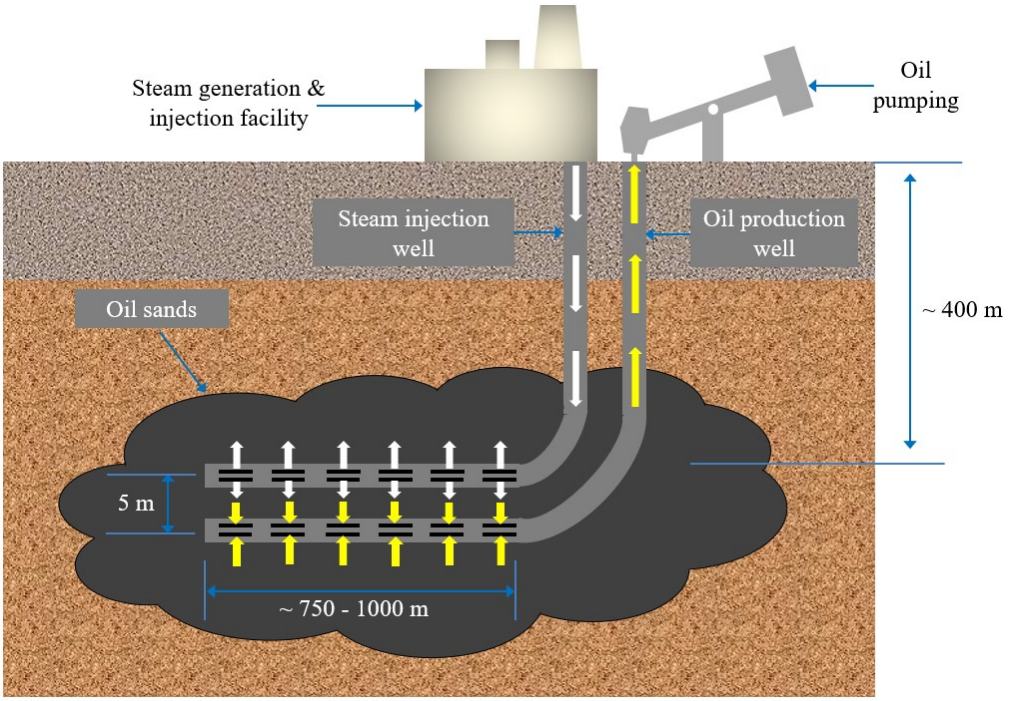

Figure 1: Schematic of a typical SAGD plant

The two major advantages of SAGD technique are that less surface land is affected as it is an underground process, and also provides access to oil sands that cannot be reached economically by surface mining [7]. However, its biggest limitation is that water recycling consumes significant energy [7].

1.1.1 Slotted liner design

The oil sands located in Alberta are unconsolidated formations with a typical mixture of sand, clay, bitumen and water [2,8]. Therefore, sand production has been a major issue in the SAGD process employed in these oil sands and requires sand control devices to retain sand particles, fines as well as other foreign particles. There are three common slotted liner designs [9] used as sand control devices namely straight, seamed and keystone as shown in Figure 2. They are mainly used due to their simple design, reasonable cost and excellent rigidity in comparison to other sand-control methods [9]. The traditional straight slotted design has uniform width

across its length and is manufactured using a single machining cut as shown in Figure 2a. A keystone design has narrow width at the opening and gets wider towards the base side at a definite angle as shown in Figure 2b. The keystone slot is manufactured with two individual cutting blades to form a single slot [9]. For the seamed slot also known by rolled design, the opening of the slot is cold rolled which deforms the opening inwards to a certain extent as shown in Figure 2c[9].

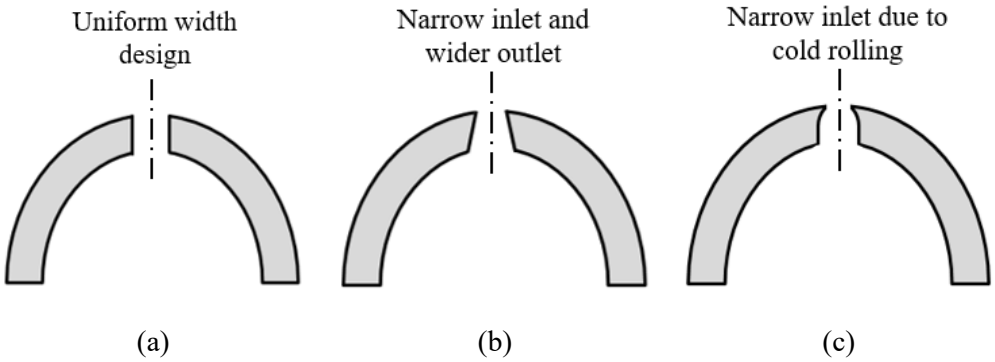

Figure 2: Slotted liner designs, a) straight, b) keystone and c) seamed/rolled

The slotted liner designs described so far have narrow rectangular slots as shown in Figure 3. The slots are cut longitudinally with a width of 0.2 to 6.35 mm and length of 38 to 76 mm along the periphery of a circular pipe [10].

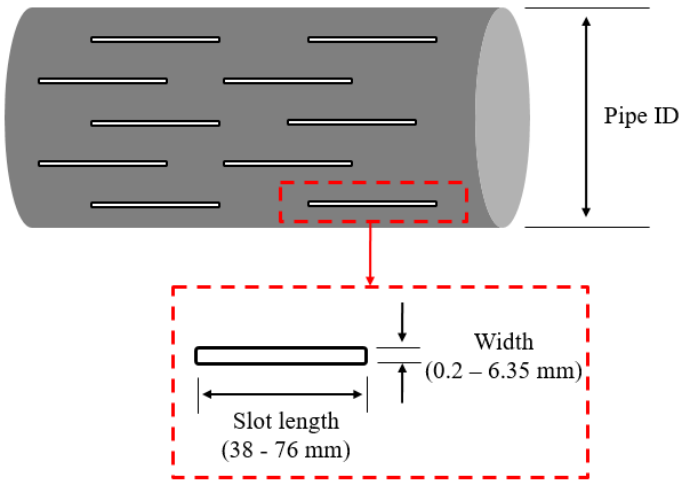

Figure 3: Narrow rectangular slots

The important design parameters of a slotted liner considered before a well-completion are slot width, slot length and slot density. The slot width is typically decided based on the particle size distribution (PSD) of the oil sands in which the sand control devices are employed to retain the sand before it enters the production well [9,11,12]. Although the main requirement of the slotted liner design is to retain the sand, a better tradeoff is required to ensure sufficient open flow area in comparison to better structural integrity. The higher flow area will ensure maximum oil production but it will also compromise the structural strength and vice-versa. Also, a narrow slot width would provide better sand retention but it will also increase the pressure drop which maintains a specific flow rate [12].

1.1.2 Failure mechanisms

In SAGD technology, the slotted liners are susceptible to major failures such as plugging and scaling [9]. These reduces the performance of oil wells and subsequently halts the oil production if the failure mode persists. These failures are primarily governed by the design parameters of slotted liner i.e. slot width and slot profile, and geological factors such as clay concentration, rock properties, grain size and mineral content [13]. Therefore, these engineering and environmental factors are taken into consideration before a wellbore is completed in order to maximize the desired production at minimum operating costs.

In plugging failure mode, the fine particles in unconsolidated formulations become moveable due to shearing forces exerted by the fluid [5]. The sand grains flow and enter the slot, and get stuck at the throat [14]. The particles in the fluid form a bridge at the slot entrance and obstruct the flow. It generates porous structure and represents Darcy flow like behavior instead of an internal flow, and results in

additional losses [14]. The slot may get completely plugged over the period of time due to combined effect of clay and sand building within the slot. It has been observed that the plugging always starts at the top i.e. the slot entrance [9]. The plugging phenomenon ultimately affects the wellbore permeability causing the increase in pressure drop and reduction in the flow rate of oil [13].

Comparative studies [8,9] have showed that the seamed and keystone designs perform better from sand-retention perspective over the straight design. Also they provide superior anti-plugging performance because they allow free movement of sand particles or fines which may enter the slot with the flow.

The scaling failure mode occurs as oilfields are rich in minerals such as calcium, iron, sulfate, bicarbonate. Calcium carbonate is the most extensive scale witnessed in the oilfields [15]. This failure mode is also encountered in other industries such as desalination, energy and steam power plants [15]. Scaling is the process of scale formation or deposition of salts on industrial equipments. It causes deleterious effects such as the reduction of pipe diameter and increased wall roughness leading to increased flow friction and power consumption as well as diminished heat transfer efficiency through low thermal conductivity. It also causes the plugging of the slots in the oilfields and reduces the oil production [15–17].

In SAGD, water condenses from hot steam and becomes saturated with the mineral ions as it flows towards the production well [15]. It may also carry trapped gases generated from the fossils buried underground. A pressure drop occurs as the oil-water mixture passes through the production well which releases the CO_2 from the solution [6,18]. It changes the bicarbonate-carbonate equilibrium towards the

carbonate equilibrium leading to calcium carbonate precipitation along with the change in pH as given by [6]:

$$Ca^{2+}_{(aq)} + 2HCO^{-}_{3(aq)} \leftrightarrow CaCO_{3(s)} + CO_{2(s)} + H_2O_{(l)} \quad (1)$$

There are several methods [19] currently in use to treat the scale deposited on industrial equipments such as periodic wash with the acids and surface scrapping by mechanical tools. However, these methods are time consuming, repetitive and economically inviable. Therefore scale inhibitors are prevalent scale treatment methods in oil and gas industry to prevent or delay growth of inorganic scales. Scale inhibitors include polyvinyl sulfonate, phosphino-polycarboxylic acid (PPCA) and di-ethylenetriamine penta (methylene phosphonic acid) or DETPMP [20–22].

1.2 Research objectives

This study focuses on the scaling failure mode specific to a SAGD production well. Slotted liner designs are employed as prominent sand control methods since the oil sands are mostly unconsolidated formations. Based on the discussion so far it is evident that scale formation process could be triggered by the pressure drop phenomenon as the oil-water mixture supersaturated with mineral ions passes through SAGD production well. This causes deleterious effects and also affects the performance of the industrial equipments. Based on this potential effect the overall objectives behind this work are,

- To monitor and predict the scale growth rate and scaling time for key slotted liner designs, and observe the locations where the scaling occurs.

- To investigate the scaling performance of different slot designs i.e. straight, seamed and keystone.

- To validate the effect of pressure drop and flow convergence on the scale formation process.

- To investigate the effect of flow parameters on calcium carbonate precipitation and growth rate.

- To investigate the effect of inlet geometry profile on the pressure loss characteristics, growth rate and scaling time.

1.3 Thesis outline

The thesis is organized in six chapters as described below,

Chapter 1 gives the general overview of the SAGD technology and relevant failure modes associated with it. It underlines the objectives and necessities behind the work, and also provides the document framework.

Chapter 2 provides the overview of the chemistry, mechanisms as well as parameters affecting the scale formation. It reviews the techniques currently in practice to evaluate the scale growth. It also explains flow related characteristics such as prediction of the entrance length, estimation of loss coefficient and understanding of flow convergence phenomenon.

Chapter 3 describes the overview of the equipments, materials, reagents, experimental conditions and procedures used in scaling and particle shadowgraph velocimetry experiments. It also explains the steps taken in processing the

experimental data to obtain the change in slot width as well as derive the 2D- velocity and pressure field.

Chapter 4 provides the experimental results and discusses the efficacy of the industrial products employed as sand control methods i.e. straight, seamed and keystone designs. It highlights the contribution of the flow convergence phenomenon in scaling mechanism and subsequent plugging of the slots.

Chapter 5 discusses the effect of inlet geometry profile on the scaling time and growth rate. It highlights the change in the flow resistance in terms of pressure loss characteristics due to ensuing change in the properties such as aspect ratio and Reynolds number.

Chapter 6 derives the conclusions based on the insights and observations from the experimental results, and provides future recommendations.

2 THEORY AND LITERATURE REVIEW

2.1 The chemistry and mechanism of scale formation

Scale formation, the growth of a dissolved salt into a solid layer, is a multifaceted process influenced by several parameters. The first step in scale formation is the collision and kinetic reaction of cation-anion species [23]. The reaction causes ions to nucleate as well as form micro-solid particles and eventually grow into macro crystals in the later stages [23]. The rate of nucleation as well as crystal growth will primarily be determined by the solution concentration and temperature of the solution. The scale formation occurs in three stages i.e. supersaturation, nucleation and crystal growth [15].

2.1.1 Supersaturation

If the solution is supersaturated, the nucleation will occur and form ideal condition for the crystal growth [19]. Solution supersaturation is the primary requirement for the scale formation and a major driving force for the nucleation. It is achieved when the concentration of cation and anion exceeds their equilibrium concentration which ultimately leads to precipitation and scale deposition [24]. However, in real scenarios the scale formation is mainly caused by the secondary reasons such as reduction in pressure, increase in pH or temperature, and to a certain extent by the changes in the flow rate or surface energy [15].

The solution supersaturation which indicates the possibility of calcium carbonate precipitation is determined by the calculation of saturation ratio (SR). It

is defined as the ratio of concentration of calcium (Ca^{2+}) and carbonate (CO_3^{2-}) ions to the solubility product constant (K_{sp}) of calcium carbonate [19] as given by:

$$SR = \frac{[Ca^{2+}][CO_3^{2-}]}{K_{sp}} \quad (2)$$

If SR is lower than 1, the solution is under-saturated and no precipitation will occur. When the SR is equal to 1 the solution is considered to be saturated, and the rate of precipitation and dissolution are same. Whereas when the SR exceeds 1 the solution is supersaturated and creates ideal scenario to form calcium carbonate scale [7,19]. The solubility product constant K_{sp}, is also a function of pressure, temperature and ionic strength [25]. It determines how much the solute can dissolve in a particular solvent at a given temperature.

2.1.2 Nucleation

For the nucleation process, a nuclei will be created once the solution attains desired supersaturation level. The time taken to form a stable nuclei is known as induction time and depends upon the saturation ratio as well as temperature of the solution [26]. An induction time is commonly determined by conducting the experiments to measure the turbidity or conductivity of the solution [17,19,26]. The infant nuclei will further act as a site for the development of micro-aggregates and subsequent crystal growth.

The process of nucleation mainly occurs in two ways i.e. homogenous nucleation and heterogeneous nucleation. Homogenous nucleation is the type of nucleation in which the presence of foreign particles or surfaces is not required. The precipitation occurring in a bulk solution is often due to homogenous nucleation.

However, it is difficult to occur in real conditions provided the supersaturation level of the solution is very high [27]. The crystallization process occurring due to homogenous nucleation will accelerate if the impurities are present in the actual system [28,29]. Heterogeneous nucleation process takes place on pre-existing surfaces or crystals. In real conditions, crystallization will primarily occur due to heterogeneous nucleation in comparison to homogenous nucleation [30]. The heterogeneous nucleation requires low surface energy and saturation ratio. Hence it has lower induction time than homogenous nucleation as it occurs on foreign surfaces [15]. Therefore, it is affected by the surface wettability i.e. how favorable is the substrate towards another medium. It has been seen that number of nucleation sites quickly rise on the solid surfaces during the initial stages of crystallization, which eventually stop increasing and instead prefer to grow as a complete crystal during the later stages [27].

2.1.3 Crystal growth

Crystal growth is the important step in the scale formation. In this process new atoms/ions/molecules/crystals are continuously added which together grow into a visible crystal in a particular crystalline structure. The common consensus is that the molecules or ions grow into a crystal by a molecular to molecular reaction [15]. Also the crystals might exist in more than one form i.e. polymorphs depending upon the surrounding conditions such as operating temperature, amount of dissolved salts, operating pressure and existing impurities in the solution. Calcium carbonate exists in three different forms- calcite, vaterite and aragonite [31]. Calcite is formed at lower temperatures as compared to other two polymorphs whereas aragonite mainly occurs at higher temperatures. Also higher

the temperature, higher the amount of vaterite will be formed [32,33]. The addition of magnesium ions as an impurity changes the structure of calcium carbonate. The greater amount of aragonite was formed with increase in concentration of magnesium ions [34]. Among the three forms of calcium carbonate, calcite is the most stable polymorph whereas vaterite is the least stable [33].

In scale formation, the growth of crystals is maintained by diffusion process under certain conditions. The rate of crystal growth due to diffusion on a pre-existing surface is directly proportional to the difference in the concentration of the depositing surface and bulk solution [35]. The crystal growth can occur due to the adhesion process in which existing pre-precipitated crystals adhere to other crystals by intermolecular forces [36]. According to surface energy theory [37], crystals prefer a shape that will have least surface energy. If so, the total free energy of the crystal at an equilibrium with neighboring medium would be also minimum at given conditions provided that the total free energy of the crystal per unit volume is uniform. Therefore, the crystal surfaces would grow in proportion to their interfacial energy i.e. crystals with low surface energy will grow faster [38].

2.2 Parameters affecting the scale formation

The scale formation process is affected by multiple factors such as saturation ratio [39], operating pressure [40], temperature [15], pH [41], surface properties [42] and flow rate[35]. There have been various studies to understand their impact on scale formation. In few circumstances, the scale production is anticipated e.g. chemicals are added into municipal water carrying pipes to introduce calcite on internal surfaces as a coating to protect it from corrosion and prolong its service period. However, in most cases the scale production has been a major challenge as

it affects the performance of the equipments across industries. Equipments without scale function smoothly and provide better return on investments.

2.2.1 Solution supersaturation

The solution supersaturation is the major driving force during the crystallization process. It has been investigated that increase in saturation ratio exponentially decreases the induction time i.e. the time required for the nucleation process [39]. Also increase in the concentration of scale forming ions increases the supersaturation level of the solution and results into rapid scale formation [28].

A study by Muryanto et al. [17] reported that the scale mass in semi-annular steel coupons increased from 0.2 grams to 1 gram when the concentration of calcium ions was increased from 3000 ppm to 4000 ppm. Maveredaki et al. [39] investigated the effect of saturation ratio on the induction time across the capillary tube. The study showed that the induction time reduced from 64 minutes to less than 0.5 minutes when the saturation ratio was increased from 1.5 to 54.8.

Based on an experimental study, Bello et al. [19] concluded that calcium carbonate crystals were absent in the solution when the saturation ratio was lower than 80. However, above this ratio the crystals were present in the solution. Therefore, this study showed that scale formation or the crystallization process is mainly dominated by the nucleation and crystal growth below saturation ratio of 80, above which it's controlled by the adhesion of pre-existing crystals.

2.2.2 Operating pressure

The solubility of calcium carbonate in water depends upon the amount of CO_2 gas present in it. As per the Henry's law [43], the higher the partial pressure of CO_2 gas, the more of it dissolves in the water. It has been reported [40] that the solubility of calcium carbonate at 40 °C reduces from 2.5 g/l to 1 g/l after reducing the partial pressure from 12 MPa to zero respectively. Another study [44] reported that calcite solubility reduced from 1800 mg/l to zero when the partial pressure of CO_2 was reduced from 100 atm to zero respectively. Zhang et al. [45] investigated the effect of back pressure up to 100 bar at the upstream of a circular test tube on scale formation. The result showed that scale growth decreased marginally with the increase in back pressure upto 100 bar.

2.2.3 Operating temperature

The solubility of calcium carbonate decreases with the increase in temperature which enhances the process of scale formation [15]. Muryanto et al. [16] studied the effect of temperature on scale formation in pipes. The study confirmed that higher temperature provides more energy to the molecules resulting in faster chemical reaction. They reported increase in the mass of calcium carbonate scale from 3.03 grams to 3.85 grams after the temperature was increased from 25 °C to 40 °C in duration of 4 hours. Bello et al. [19] assessed the effect of temperature on scale formation in a 1 mm diameter capillary tube for the saturation ratio of 5. The study concluded that temperature enhanced the growth kinetics which lead to decrease in scaling time from 72.7 hours at 25 °C to 16.7 hours at 70 °C.

2.2.4 Effect of solution pH

The level of pH indicates the acidity or alkalinity of the solution. It influences the solubility of the calcium carbonate [23]. The amount of calcium carbonate dissolved in water reduces from 325 ppm at pH 7 to 0 ppm at pH 14 [23]. Therefore increase in pH enhances the possibility of the scale formation. Andritsos et al. [29] confirmed that changing the pH of solution resulted in faster scale formation. According to study conducted by Oral et al. [46], pH has a strong effect on calcium carbonate polymorphs. The study reported that the amount of calcite increased from 10% at pH 8 to 100% at pH 12. The change in pH also grew the crystal size to 3 μm.

2.2.5 Surface properties

Surface variables play crucial role in different phases of crystallization i.e. nucleation, precipitation and growth when proper conditions are achieved such as supersaturation, temperature and chemical composition [19,47]. The amount of scale formed on the surface will then depend upon its properties such as roughness and interfacial energy.

Rough surfaces tend to have more scale formed as compared to smooth surfaces as they provide more area for the nucleation sites, and also because they require higher stress to remove the scale from the surfaces [36]. Ruckenstein et al. [48] performed numerical study considering the interfacial energy to investigate the heterogeneous nucleation on a surface with nano-cavities and compare it with a planar surface. This study was conducted for different contact angles and cavity- radii. It concluded that the nucleation rate is higher on the surface with

cavities when compared to a plane surface. The nucleation rate increased with the increase in curvature of cavity because it offered more area for interaction of scaling ions with the surface. Similar observations were made by Gunn et al. [49] that the surface type affects the nucleation and crystal growth process, and higher scale mass was seen on rougher surfaces than smooth surfaces as it substantially improved the nucleation rate.

Surface energy also acts as a bridge between the molecule trying to reside and the solid surface supporting the infant crystal [30]. The relationship between the surface energy and contact angle (θ) is given by,

$$\cos\theta = \frac{\sigma_{sl} - \sigma_{sc}}{\sigma_{cl}} \tag{3}$$

where σ_{sl} and σ_{sc} are the interfacial energies between the surface-liquid and surface-crystal interfaces respectively. The surfaces with low energy increase the induction time i.e. it reduces the nucleation rate. This surface behavior is ideal in scale mitigation studies but this it's only useful during the initial stages of crystallization [47,50]. The surface energy is generally related to the wettability of the substrate and is usually measured in terms of contact angle. A high energy surface will have low contact angle and hence greater possibility of scale formation [47].

Generally metal surfaces have high energy whereas plastics are material with low energy surfaces. Wang et al. [50] studied the influence of substrate on the surface scale formation. Experiments were performed under hydrodynamic conditions for 1 hour on four different substrates namely Teflon (21.8 mN/m), pre-treated stainless steel (32 mN/m), diamond like carbon (34 mN/m), and untreated stainless steel (45 mN/m). The results showed that lower amount of scale was

formed on the Teflon as it had lowest surface energy among the four substrates considered. Also it offered lower number of nucleation sites for the scale agglomeration due to its hydrophobic nature. Most scale was formed on untreated stainless steel surface owing to its highest surface energy.

Similar study was performed by Cheong et al. [47] to understand the effect of substrate type on surface adhesion and crystallization. The tests were on conducted on coated surfaces of polymer and stainless steel along with an uncoated stainless steel surface for 1 hour using the rotating disk electrode method. The study reported increase in scale mass on all surfaces but coated stainless steel surface had least gain in terms of scale mass as compared to coated polymer surface. The uncoated stainless steel showed its vulnerability to high scaling.

2.2.6 Effect of flow rate

Multiple studies [16,17,19,28,33,45] have concluded that flow rate substantially aid scale formation process as long as it is within the laminar regime. Increase in the flow rate enhances the motion of participating molecules in the crystallization process [16].

A study conducted in semi-annular steel coupons by Muryanto et al. [16] showed that scale mass increased from 0.7 grams to 1.4 grams when the flow rate was increased from 30 ml/min to 50 ml/min. Similarly Bello et al. [19] studied the effect of flow rate on scale formation in a 1 mm diameter capillary tube. The study reported that scaling time i.e. the time taken to reach differential pressure of 5 psi decreased from 72.7 hours to just 9.7 hours when the flow rate was increased from 5 ml/min to 30 ml/min. Zhang et al. [45] found that scale formation increases with

flow rate in a circular test tube and remains stable till the flow velocity of 0.5 m/s. However, in this study the scale formation decreased when the flow velocity exceeded 0.7 m/s, due to resulting increase in shear forces. The static bottle test conducted by Sutherland et al. [51] showed that the turbulence enhances mixing of scaling ions and increases the likelihood of nucleation sites creation as well as the scale formation.

Moghadasi et al. [28] investigated the effect of flow rate on permeability decline and pressure drop in a test section consisting of a porous media. The study found that permeability reduced in a range of 35% to 61% after increasing the flow rate from 50 cm^3/min to 100 cm^3/min respectively. It was concluded that with increase in flow rate, more scaling ions passed through the test section. It led to faster growth kinetics and reduction in pressure as well as sharp decline in the overall permeability.

2.3 Assessment of scale formation or growth rate

There are various techniques currently in practice to estimate the growth rate in the scaling experiment. Generally these methods quantify the parameters affected by the scale kinetic reaction such as changes in pH, conductivity or concentration of scaling ions. Methods employed to investigate scaling include monitoring the pressure drop across the test tube due to subsequent nucleation and crystal growth with respect to time.

2.3.1 Quartz crystal microbalance

Maveredaki et al. [39] used quartz crystal microbalance (QCM) technique to evaluate the induction time and growth rate of calcium carbonate scale. In this

technique, a quartz crystal is pre-coated with stainless steel material which is mounted in between two electrodes and is oscillated at a certain frequency with an applied voltage. However, the frequency of the oscillation depends upon the mass. Based on the scale mass deposited the frequency changes with respect to time. The frequency is then used to determine the deposited mass and subsequent growth rate by using Kanazawa's improved equation [39]. In this study, QCM was primarily implemented during the initial stages of crystallization since the scale growth continues and reaches the maximum load limit on the quartz crystal surface. This technique showed that the growth rate is of linear in nature.

2.3.2 Optical techniques

Optical techniques are used primarily in electrodeposition [34] and membrane scaling [52,53] to monitor the nucleation sites and crystal growth on a surface of interest in real time by means of an optical microscope. In this technique, two dimensional images are captured at time certain intervals. Image analysis software or image processing methods detect the number of nucleation sites i.e. crystal density and measures the surface coverage as well as an increase in the surface area of crystals over a period of time [34,52–55]. Based on this information, the rate of crystal growth is determined which is predominated by heterogeneous nucleation. These studies emphasize the crucial role of surface crystallization in scale formation process over pre-precipitated crystals present in the solution.

2.3.3 Measurement of differential pressure

In this method, the change in differential pressure across a test tube as a function of time due to scale formation is documented. The increase in the scale

thickness due to subsequent crystal growth causes the pressure drop to rise with time. As the crystal growth continues further, the scale thickness increases and results into blockage of test tube as long as the flow regime is laminar in nature as the crystals formed will not get washed away. This method is used widely in practice to compare the effect of different flow rates, saturation ratios, and surface properties on the scale formation [8,19,39,45].

The scaling time (t_s) information i.e. the time taken by the differential pressure to reach certain limit (e.g. 10 psi) is used to obtain the relation between the theoretical nucleation time as a function of saturation ratio (SR) based on the classical nucleation theory as [47]:

$$\log t_s = \mathrm{A} + \left(\frac{\mathrm{B}}{\log^2 \mathrm{SR}}\right) \tag{4}$$

where A and B are constants obtained by fitting t_s vs SR experimental data, and B is a function of two factors, interfacial tension and operating temperature which influence the nucleation process.

Wang et al. [56] and Lawal et al. [57] used change in pressure drop across capillary tube to estimate the thickness of asphaltene deposited using the Hagen-Poiseuille equation. In this method, it was assumed that pressure drop rises gradually with uniform deposition of asphaltene inside the capillary tube. The pressure drop given by Hagen-Poiseuille equation is:

$$\Delta P_0 = \frac{8\mu QL}{\pi r_0^4} \tag{5}$$

where Q is the flow rate, μ is the viscosity, L is capillary tube length, ΔP_0 and r_0 are the initial pressure drop and capillary tube radius respectively.

Similarly the pressure drop due to uniform asphaltene deposition having thickness of Δr_t at time t is given by:

$$\Delta P_t = \frac{8\mu QL}{\pi[r_0 - \Delta r_t]^4} \tag{6}$$

The relative change in pressure drop was then used to calculate the asphaltene thickness at time t assuming it was much lower than initial capillary tube radius as:

$$\frac{\Delta P_t - \Delta P_0}{\Delta P_0} = 4\left(\frac{\Delta r_t}{r_0}\right) \tag{7}$$

2.3.4 Inductively coupled plasma mass spectrometry

Bello et al. [19] employed inductively coupled plasma mass spectrometry (ICP-MS) to determine the amount of calcium (Ca^{2+}) ions in a capillary tube during the experiment. Based on the concentration of Ca^{2+} ions, the growth rate of calcium carbonate was calculated as the ratio of amount of Ca^{2+} ions determined through ICP-MS test with the time taken to reach the differential pressure of 5 psi measured across the capillary tube.

In the same study, the growth rate was also estimated using equation (7) based on the Hagen-Poiseuille equation. Based on the comparison it was concluded that growth rate estimated by Hagen-Poiseuille equation is approximate and overestimates the calcium carbonate growth rate when compared to ICP-MS technique.

2.3.5 Measurement of scale mass

Muryanto et al. [16,17] developed a test rig to assess the influence of flow rate, solution concentration, temperature and inhibitor effectiveness on gypsum as well as calcium carbonate scale formation and growth rate. The test rig included a test section consisting of a tubular sleeve with four semi-annular coupons in which the scale was deposited for a duration of 4 hours. At the end of the experiment, semi-annular coupons were dried overnight in an oven followed by the weight measurement. The scale mass was then obtained as the change in weight of coupons before and after the experiment. The scale growth rate was then calculated as the ratio of scale mass to the duration of experiment for different parameters considered.

2.3.6 Summary of scale formation assessment techniques

For the scale assessment, current studies rely upon the use of techniques such as quartz crystal microbalance (QCM), optical methods, inductively coupled plasma mass spectrometry (ICP-MS), actual measurement using weighing scale and pressure drop measurement. So far, QCM, ICP-MS and optical methods are employed to assess the scale growth on the surfaces of interest. However, these techniques are used when there is shallow nature of scale growth on the surfaces, no significant flow obstruction is occurring or the flow channel is not getting plugged due to scale formation. This seems to be a limitation of the optical techniques use. Whereas, the pressure drop measurement technique provides the information even when the flow channel or test tube is getting plugged. However, it cannot provide any visual information.

Therefore if a flow rig is developed which simultaneously offers optical measurement of the scale growth and pressure drop when the flow obstruction is significant, then maximum information can be retrieved from the experiment. This would be a great advantage for the SAGD in-situ applications to investigate the flow characteristics such as pressure loss as the scaling failure mode causes significant flow obstruction and plugs the slot completely.

2.4 Flow through sudden contraction

A flow passing through sudden contraction is a widely studied topic. It is relevant in wide variety of applications ranging from duct design, heat exchangers, piping systems, orifices, valves to flow measuring devices [58,59]. The fluid passing through a conduit system leads to energy losses, and needs to be taken into consideration for the estimation of power requirement to overcome the said losses.

In internal flows, also known as entry flows, the fluid enters the confined geometry from a large reservoir and moves forward under a pressure difference [60]. When it starts to move into the confinement zone, the surrounding wall retards its motion. It forces the fluid velocity at wall to become zero due to no-slip boundary condition. As a result, the velocity increases towards the center in order to satisfy the continuity equation, and a velocity gradient is developed in the confined geometry [61] as shown in Figure 4. As the flow progresses, a boundary layer region dominated by viscous effects starts to develop. The thickness of boundary layer grows from zero at the wall surface to maximum at the center after fluid travels a certain distance known as the entrance length [62]. In a fully developed region the fluid characteristics do not change along the length i.e. it completely attains the parabolic velocity profile, centerline velocity reaches 99% of

its fully developed value as well as shear stress remains constant. Also the fluid acceleration in longitudinal direction as well as the velocity component in lateral direction are absent [60,62].

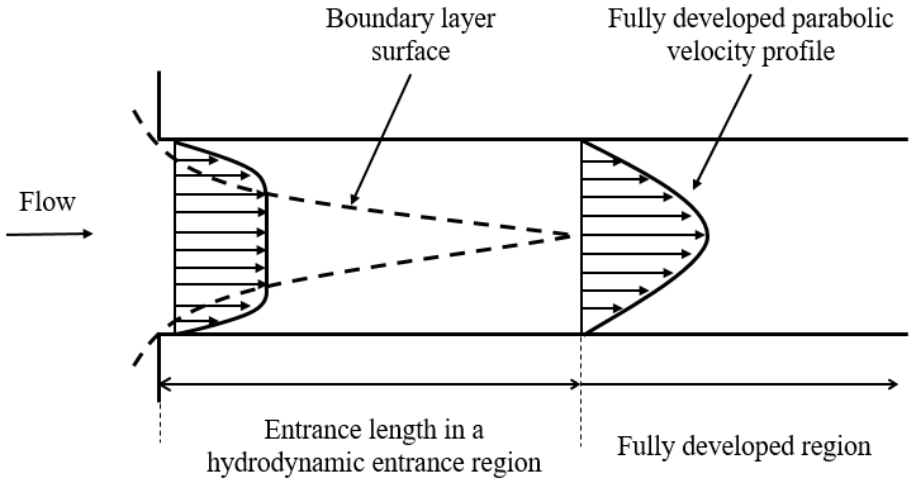

Figure 4: Velocity profile development

The fluid flow experiences sudden change in the geometry as it enters the confinement which causes a pressure drop. The pressure further reduces linearly due to viscous effects in the fully developed region. Shapiro et al. [63] studied the effect of streamline curvature on the pressure as shown in Figure 5. The lines AB and CD represent different concavities drawn perpendicular to the streamlines. The average pressure on curve AB is slightly lower than upstream pressure. However, the pressure on point A is higher than B due to streamline curvature, and hence higher than the upstream pressure as well. The pressure on curve CD is marginally greater than the pressure at downstream. However, the pressure increases from point C to D due to the curvature, and the pressure on point C is lower than the average. So the pressure on point C is lower than A. It was reported that the pressure constantly reduced from point B to D being on the wall. Therefore it can be said that the flow convergence phenomenon causes the pressure drop. Also higher the

streamline curvature, higher will be the pressure drop and fluid velocity at the slot entrance [63–66].

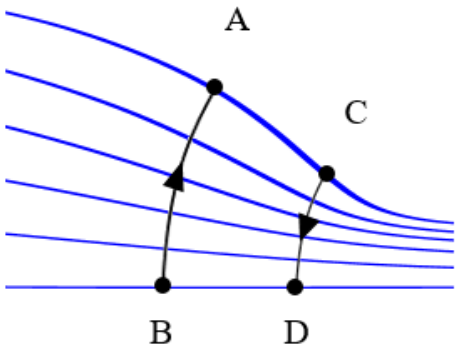

Figure 5: Schematic of streamline curvature

Kaiser et al. [14] studied the near-well bore fluid mechanics where the fluid flow converges the slot using a semi-empirical method. Based on this method the relationship between the slot density and pressure drop was established. The study reported higher pressure drop due to flow convergence phenomenon in comparison to that encountered by an open slot without any convergence. Flow convergence in rectangular slots using particle shadow velocimetry was studied by Yusuf et al. [66]. This study concluded that flow convergence due to geometry contraction causes a significant pressure drop in the near slot entrance region. Also a relationship was established to show that pressure drop increases with increase in the curvature of streamlines as the Reynolds number increases.

Pressure drop for a flow through the rectangular cross-section has been previously studied for different aspect ratios as it influences the curvature of streamlines. Experimental measurements showed that pressure drop increased with increase in the aspect ratio [65,67–69]. A model was established by Yusuf et al. [64] to develop a relationship between the pressure drop and aspect ratio. The model

considered flow convergence parameter in order to describe the converging behavior of the flow.

2.4.1 Prediction of the entrance length

The understanding of hydrodynamic development region i.e. entrance length is essential in fluid related studies as the properties such as pressure gradient, wall shear stress, frictional losses and flow velocity are often quantified in reference to fully developed region. Generally the entrance length (L_e) for a laminar flow through a confined geometry of hydraulic diameter is dependent on the Reynolds number as [70]:

$$L_e = 0.06 Re D_h \tag{8}$$

where the Reynolds number (Re) and hydraulic diameter (D_h) are calculated as:

$$Re = \frac{\rho V D_h}{\mu} \tag{9}$$

$$D_h = \frac{4 \times \text{Cross} - \text{sectional area}}{\text{Wetted perimeter}} \tag{10}$$

where, V is the average velocity, ρ is the density and μ is the viscosity of the fluid.

The equation (8) provides the relationship applicable to inertial flows passing through a macro-duct, and when Reynolds number is greater than 1. However, it has been investigated that inertial forces begin to dominate the flow field only when Reynolds number exceeds a magnitude of 50 [71,72]. It has been identified through various numerical and experimental studies that equation (8) is not universally applicable for the prediction of entrance length and may induce error especially for the systems at micro or meso scale [73]. The entrance length will be

shorter for the geometries with high aspect ratio and rectangular micro-channels or if the flow is pre-developed before it reaches the sudden contraction [74,75]. Also inlet velocity profile affects the entrance length especially at lower Reynolds numbers due to involvement of diffusion whereas for high Reynolds number flows there is weak dependence on inlet velocity profile [76,77].

Based on the experimental investigations performed by Lee et al. [78] in a rectangular channel with aspect ratios of 0.40 and 2.75, and for Reynolds numbers ranging from 1 to 100, it was concluded that aspect ratios significantly affect the entrance length correlations for the flow rates considered in the experiment. However, the entrance length had minor influence of Reynolds numbers considered in this study, probably due to stronger effect of aspect ratios.

Multiple numerical and experimental studies investigated the effect of aspect ratios on the entrance length in a rectangular channel. These studies reported the linear dependence of entrance length on the product of Re and D_h [57,79,80]. Also the observation was that entrance length became shorter with increase in aspect ratio [81–83].

An experimental study was conducted by Ahmad et al. [74] using micro-PIV to investigate the entrance length for micro-channels of hydraulic diameter 100 μm, 200 μm and 500 μm, and Reynolds numbers varying from 0.5 to 200. In this study square micro-channels were considered in order to nullify any effects arising due to aspect ratio. The experimental study confirmed linear behavior of entrance length for $Re > 10$. Also it reported that the entrance length has a certain value for $Re < 10$ which would otherwise be closer to zero considering the linear correlation. Based on the comparison with other studies, this experimental study

reported that entrance length calculations correlate well with those available for conventional ducts when $Re > 10$, whereas for $Re < 10$ it showed good correlation with the formulations obtained by the parallel plate theory. Similar study was performed by Li et al. [84] which concluded that entrance length and Reynolds number have non-linear correlation when Reynolds number is lower than 12.5 whereas it showed linear correlation when Reynolds number exceeded 15.

The linear and non-linear entrance length correlations from various experimental studies are summarized in Table 1.

Table 1: Entrance length correlations from previous experimental studies

Author	D_h	AR	Re	Entrance length correlation
Ahmad et al. [74]	100, 200 and 500 µm	1	0.5 to 200	$\frac{L_e}{D_h} = \frac{0.16}{0.14Re + 1} + 0.0752Re$
Goldstein et al. [85]	1 cm	1	69 to 387	$\frac{L_e}{D_h} = 0.09Re$
Hao et al. [86]	237 µm	Trapezoidal	50 to 1200	$\frac{L_e}{D_h} = 0.08 \ \ to \ \ 0.09Re$
Lee et al. [87]	380 µm	2.65	250 to 2100	$\frac{L_e}{D_h} = 0.033Re$
Li et al. [84]	100, 150 and 200 µm	1	0.5 to 50	$\frac{L_e}{D_h} = \frac{0.28}{0.1Re + 1} + 0.04Re$ (for $Re < 12.5$) $\frac{L_e}{D_h} = 0.0578Re$ (for $Re > 15$)
Muchnik et al. [83]	1.3, 1.6 and 1.8 cm	2, 4 and 10	200 to 600	$\frac{L_e}{D_h} = 0.035 \ \ to \ \ 0.09Re$
Sparrow et al. [80]	1.04 and 2 in	2 and 5	1000 to 5000	$\frac{L_e}{D_h} = 0.08Re$ (for $AR = 5$) $\frac{L_e}{D_h} > 0.08Re$ (for $AR = 2$)

2.4.2 Estimation of loss coefficient

As the flow passes through sudden contraction, the energy dissipates and causes the pressure drop. The reduction in pressure is highest at the geometry entrance due to flow convergence, excessive increase in the kinetic energy and resulting shear stress. The pressure further reduces linearly in fully developed region due to viscous effects [60,62].

The losses incurred due to sudden contraction are often commonly known as minor losses as they are often lower than major losses caused by the viscous forces in the longer pipes [60,62]. However, for the case of short channels it has been investigated that the increase in pressure drop due to change in kinetic energy is significantly higher than those due to viscous losses [88]. The static loss in pressure as the flow passes through sudden contraction is generally determined by measuring the pressure at the upstream and downstream of the contraction. The losses (h_L) depend upon the geometry profile, flow velocity and fluid properties, and are directly related to the velocity head as [89]:

$$h_L = K\frac{V^2}{2g} \tag{11}$$

where, K is the loss coefficient and represents energy dissipation caused by the passage of flow at certain velocity (V) through a conduit system. The loss coefficient is usually in expressed in a form given below [90]:

$$K = A + \frac{B}{Re} \tag{12}$$

where, A and B are empirical constants. The loss coefficient is a strong function of the Reynolds number and geometry contraction ratio (β) [72]. Figure 6 shows the general trend followed by the loss coefficient depending upon the flow regime when the fluid passes through sudden contraction.

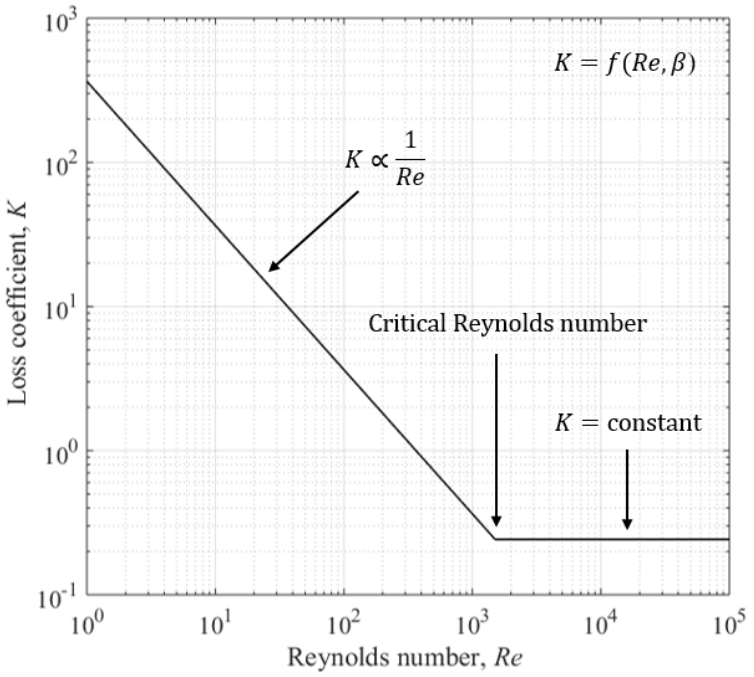

Figure 6: Dependency of loss coefficient on Reynolds number

The loss coefficient is a function of Reynolds number for laminar flows and decreases with increase in the Reynolds number [68,72,89,90]. Also the laminar loss coefficient decreases with increase in the contraction ratio for the same Reynolds number [72,89]. Figure 6 shows inverse relationship with the Reynolds number for a particular contraction ratio. A summary for the experimental values of the loss coefficient constant for laminar flow can be found in the literature [72].

The Bernoulli's equation derived for the steady and frictionless flow can be used to associate the pressure drop with the corresponding change in the kinetic energy due to sudden contraction as:

$$\frac{P_1}{\rho g} + \frac{V_1^2}{2g} + Z_1 = \frac{P_2}{\rho g} + \frac{V_2^2}{2g} + Z_2 + h_L \tag{13}$$

where, subscript 1 and 2 represent upstream and downstream conditions respectively as shown in Figure 7, P is the static pressure, V is the average velocity,

Z is the elevation from the datum, ρ is the density of the fluid and h_L is the head loss.

Using the equation (11) and (13), the associated pressure loss coefficient can be calculated by:

$$K = \frac{\left(\frac{\Delta P}{\rho g} + \Delta Z\right)}{\left(\frac{V^2}{2g}\right)} \tag{14}$$

It can be said from equation (14) that there will be change in the loss coefficient as the pressure drop will increase due to gain in the kinetic energy as the width of the narrow rectangular slot reduces due to calcium carbonate formation as well as growth with time in current experimental study.

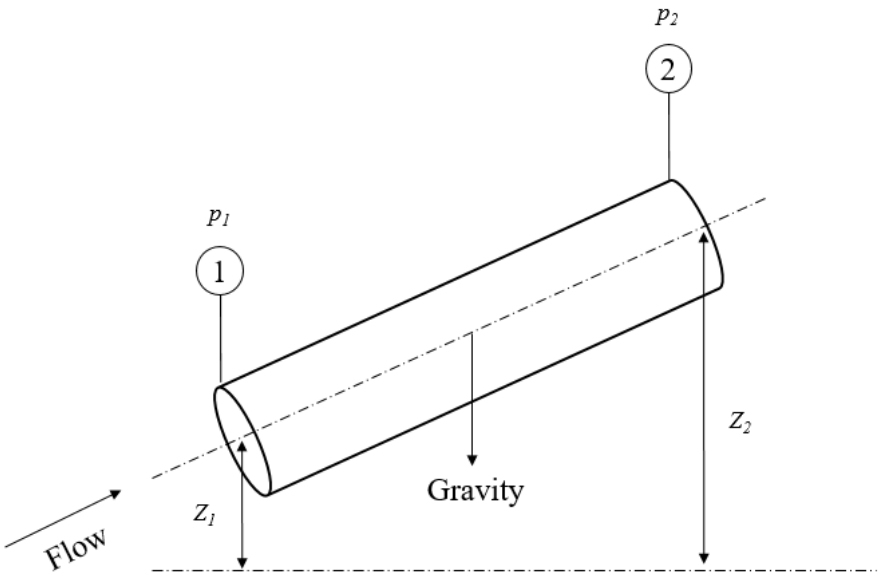

Figure 7: Respective upstream and downstream conditions

2.5 Summary

The formation of calcium carbonate scale is a multi-step process and mainly occurs in three stages of supersaturation, nucleation and crystal growth. The possibility of scale formation increases with increase in solution supersaturation, flow rate, pH, temperature and pressure drop. The surface properties such as interfacial energy and roughness play a crucial role in the scaling process. The more scale is formed on rough surfaces as well as on higher energy surfaces such as metals. The widely used method to evaluate the scale formation is the measurement of differential pressure across the test tube. From the near-well fluid mechanics perspective, the fluid flow converges as it approaches the rectangular slot. It results into increased pressure drop which increases the possibility of the scale formation process. The pressure drop increases with increase in the aspect ratio of the rectangular channels. Also the pressure loss characteristics depend upon the flow regime and geometry contraction ratio.

The detailed review of the literature reveals that the scale formation process has been mainly studied in order to understand the effect of thermodynamic parameters such as system pH, temperature, surface properties and induction time. However, there are very few studies which have tried to understand the effect of flow related aspects such as flow convergence, streamline curvature as well as change in the flow resistance on the calcium carbonate scale formation. Also, image acquisition system has been rarely used in the dynamic flow and in-situ conditions, and to the best knowledge of the author, this is one of its kind of a study in which the image acquisition has been used to monitor the calcium carbonate scale growth and investigate pressure loss characteristics in narrow confined geometry. Another

gap identified from the existing literature is that there is lack of the experimental data for the loss coefficient for laminar flow through sudden contraction with rounded edges.

3 EXPERIMENTAL SET-UP

An experimental set-up was developed to simulate the formation and growth of the calcium carbonate as well as to visualize the flow related phenomenon in the narrow slot. To undertake this, two experimental measurements are needed. Monitoring the growth of the calcium carbonate and measure the subsequent changes in the differential pressure during the scaling experiment, and determination of the pressure field from the velocity data using particle shadowgraph velocimetry (PSV) technique. The experimental set-up mimics the flow through a single rectangular slot of the actual slotted liner design deployed in in-situ SAGD application. However, the experimental conditions used in this study are different to the conditions at which a SAGD production well operates considering the downtime required to simulate the plugging of the slot due to scaling process. Therefore, this chapter provides the overview of the equipments, materials, reagents, experimental conditions and procedures used in the scaling and PSV experiment.

The first section discusses the experimental set-up and provides the details of optical equipments along with the flow cell as well as the particulars of slot profiles used in the experiment. The second and third section explains the procedure involved in the PSV and scaling experiment such as the working principle of PSV, calibration of the pressure transducer, measurement of differential pressure and estimation of solution supersaturation.

3.1 Experimental set-up for scaling and PSV experiment

The experimental set-up shown in Figure 8(a) was used to monitor the growth of calcium carbonate as well as to measure the velocity field. This consists of a high-speed camera (either a SP-5000M-PMCL-CX; JAI Inc. for monitoring the calcium carbonate growth or a FASTCAM Mini WX50; Photron Inc. for collecting the images in the PSV experiment) coupled with a 105 mm lens (f2.8-DG Macro; EX SIGMA Inc.) along with extension tubes, a LED light source (Pulsar 320; Advanced illumination Inc. or ILA.LPS 3, ILA5150 GMbH, Germany), flow cell, peristaltic pump (Masterflex L/S; Cole-Parmer Inc.) and magnetic stirrer. The function generator (AFG3021B; Tektronix Inc.) with square waves output was used to control the frame rate of the camera at an offset of 2.5 V, amplitude of 5 Vpp and frequency of 90 Hz or 300 kHz in case of PSV or scaling experiment respectively. The differential pressure is measured using a pressure transducer (DP15-36; Validyne Inc.) containing a diaphragm (DP15-34; Validyne Inc.), working in conjunction with a voltage demodulator (Model CD-15; Validyne Inc.) and data acquisition system (NI-9219; National Instruments Inc.). The complete setup that was actually used in scaling experiment is shown in Figure 8(b).

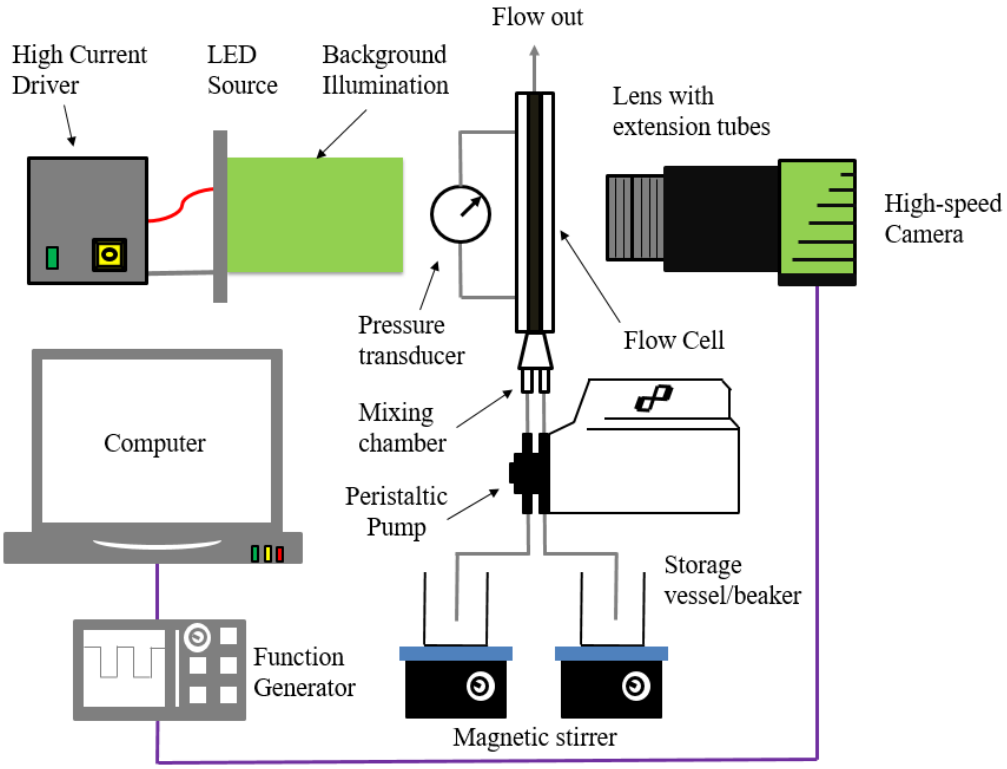

(a)

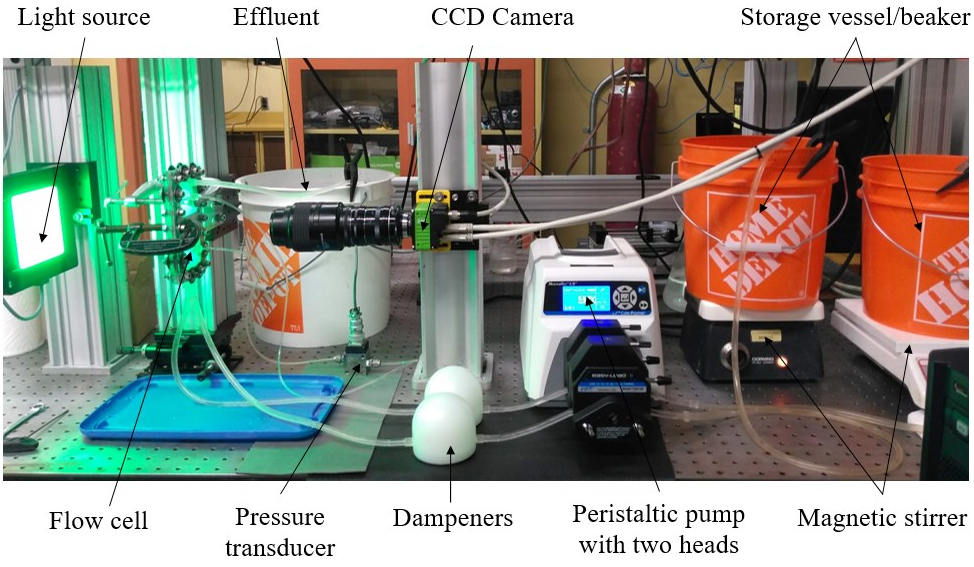

(b)

Figure 8: (a) Schematic of the experimental set-up (b) actual picture of the set-up in scaling experiment

3.1.1 Experimental conditions

Experiments were performed at the flow rate (Q) of 900, 1200 and 1500 ml/hr, and at room temperature of 25 °C. All experiments were repeated three times to understand the repeatability of the experiment. The entrance length and Reynolds number were calculated at given experimental conditions based on equation (8) and (9) by considering the ambient properties of water with viscosity of 0.001 Pa-s and density of 1000 kg/m^3 and are shown in Table 2. The equation (8) provides the generic entrance length correlation established for an inertial flow passing through a macro-duct. These calculations provide an insight into the flow behavior for the scaling and PSV experiments.

The Reynolds number defines the flow regime of the fluid passing through the flow cell. Laminar flow substantially aids in the scale formation process [35] whereas turbulent flow field has been detrimental to it [45]. The increase in flow rate leads to rise in differential pressure across the narrow rectangular slot as well as alters the rate of crystal growth [19]. Entrance length calculations provide the information regarding the establishment of fully developed region as energy losses are highest at the channel entrance due to sudden contraction. Based on the magnitude of Reynolds number in Table 2, it can be concluded that the flow lies in laminar regime for all the three flow rates considered in this experimental study.

Table 2: Reynold number and Entrance length calculation

Flow rate, ml/hr	Reynolds number (*Re*)	Entrance length (L_e), mm
900	68	7.1
1200	91	9.4
1500	113	11.8

3.1.2 Flow cell design

Figure 9 shows a flow cell design with straight slot profile annotated in red box. It is assembled between two acrylic sheets. The flow cell assembly is bolted together to preserve the structural integrity. A groove of rectangular cross-section is made within the two acrylic sheets by slot milling to fit an O-ring and prevent the leakage. The use of acrylic sheets ensures the flow cell is optically accessible in order to visualize the flow field. The acrylic sheets are prepared using the laser cutting process (VersaLaser; Universal Laser Systems Inc.). A thin and transparent layer of Teflon (23-5S-3D; CS Hyde Inc. USA) with thickness of 0.13 mm was installed adjacent to the acrylic sheets to reduce the nucleation rate of calcium carbonate [47]. This ensures the calcium carbonate scale grows on the two sides of the stainless steel walls and not effectively on the acrylic sheets in front of the camera. It allows to capture the images with the best possible clarity. The Teflon sheet was changed after every three experiments. A pressure transducer was located across the slot to measure the static pressure drop as the fluid passes through the sudden contraction from bottom to top direction. The flow cell is mounted vertically so the measurement of pressure includes the effect of gravity forces. The flow cell has a thickness of 6.35 mm and is made of stainless steel (Type 316). This material is preferred due to its corrosion resistance properties.

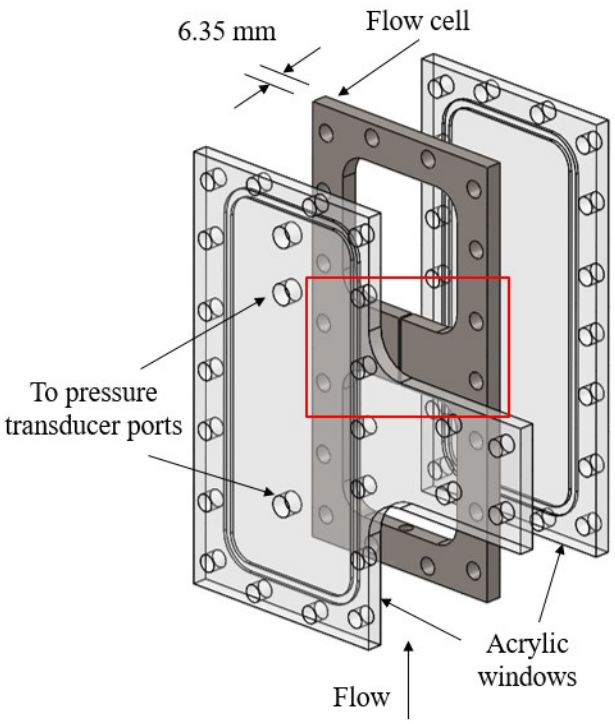

(a)

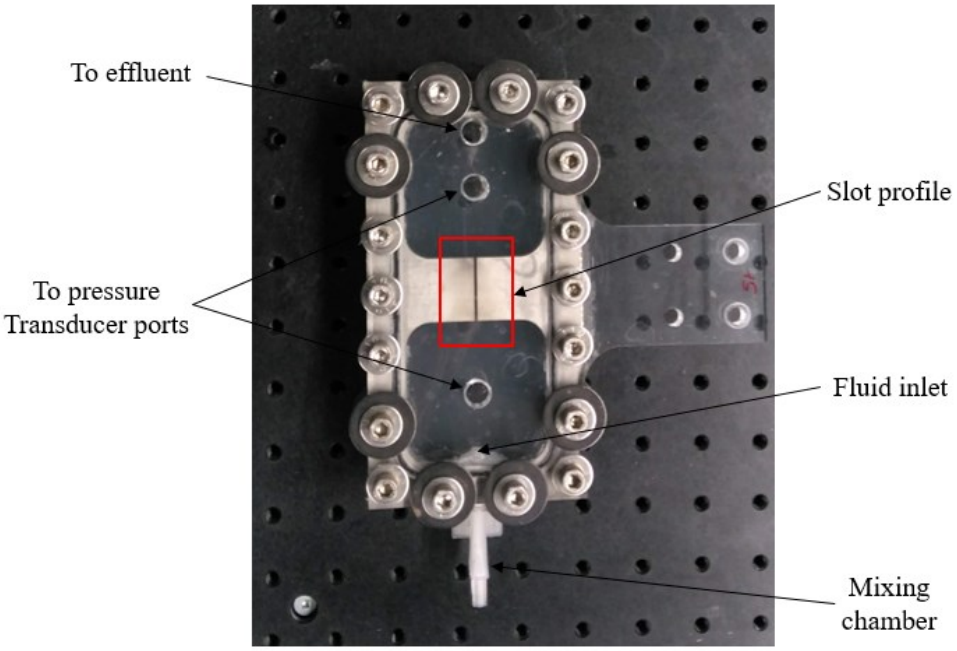

(b)

Figure 9: (a) Schematic and (b) picture of the flow cell assembly

The flow cell is manufactured with water jet cutting method which provided default surface roughness of 80 rms. The benefit of water jet cutting is that it is a faster method but its biggest limitation is that the manufactured part will have certain taper inbuilt for a thickness of 6.35 mm. In order to measure the taper in straight slot design, five different measurements of the slot width were taken on the top and bottom side of the flow cell across its length with a Vernier caliper as shown in Table 3. The average slot width on top and bottom sides were 0.98 mm and 0.86 mm respectively. Therefore the average taper in this flow cell of a 6.35 mm thickness is 0.54 °.

Table 3: Taper measurement in a flow cell with straight slot

	Measured slot width in mm	
	Top side	Bottom side
1	0.99	0.9
2	0.96	0.85
3	1.00	0.81
4	0.99	0.86
5	0.96	0.86
Average width	0.98	0.86
Flow cell thickness	6.35 mm	
Average taper	0.54 °	

There were four different flow cells used in experiments with a specific slot profile i.e. straight, seamed, keystone and rounded designs as shown in Figure 10. In this study, the flow cell is a full plate thickness with a standard rectangular cross section.

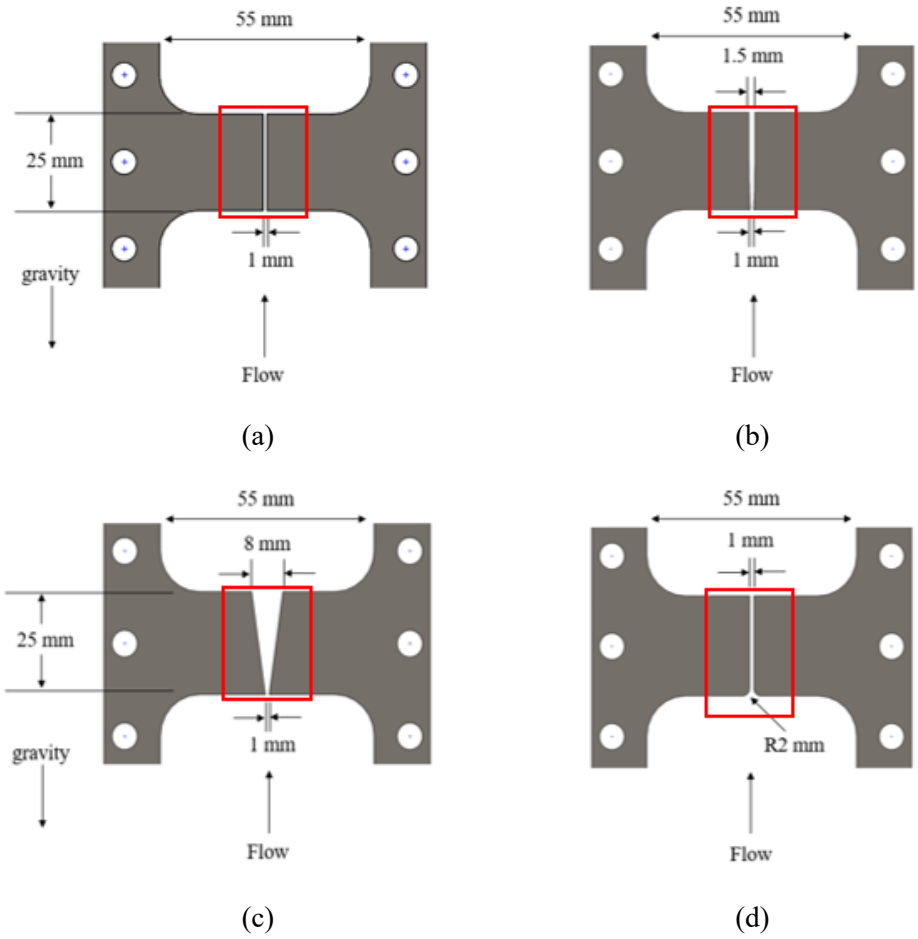

Figure 10: Details of the slot profiles a) straight, b) seamed, c) keystone, and d) rounded designs

The straight slot design is a traditional slotted liner with a width of 1 mm and length of 25 mm as shown in Figure 10(a). The hydraulic diameter of the clean and empty channel is equal to 1.73 mm for a depth of 6.35 mm and width of 1 mm as calculated by equation (10). For the seamed design, the slot opening is rolled inwards which makes the entrance narrower than outlet as shown in Figure 10(b). Its width at the inlet and outlet is 1 mm and 1.5 mm respectively. The keystone

design is comparatively similar to the seamed design. However, in this study different dimensions of the keystone design were chosen, and its wider width at the outlet is not realistic to current industry standards. The design of keystone slot has a narrow entrance of 1 mm and wider outlet equal to 8 mm as shown in Figure 10(c). Inclusion of this design will help to investigate the effect of geometry having a greater open area and wider outlet on the scale formation. The rounded design has radius of 2 mm at the entrance instead of a sharp edge present on the straight design and is shown in Figure 10(d). This radius of 2 mm provides gradual change in the geometry profile. Therefore the flow resistance in this design will be minimal in comparison to all other designs. As described in section 1.1.2, a seamed design is preferred over the straight design due to its perceived anti-plugging performance.

The aspect ratio of the channel can be used as an important non-dimensional parameter to compare different geometries. In this study, a change in aspect ratio is used to evaluate the converging behavior and pressure loss characteristics due to real time scale formation. The aspect ratio (AR) for a rectangular flow cell with depth (d) of 6.35 mm and an instantaneous slot width $w(t)$ is calculated as:

$$AR = \frac{\text{depth}}{\text{slot width}} = \frac{d}{w(t)} \tag{15}$$

3.1.3 Camera

There were two different cameras used for scaling and PSV experiments as their requirements were distinct to each other. The scaling experiment required the growth to be monitored by imaging a comparatively large field of view (FOV) and collecting images at a known interval over a long duration of time. However, the particle shadowgraph velocimetry experiment required multiple images to be taken within a fraction of time at high resolution owing to the high flow rates considered.

For the scaling experiment, a CMOS camera (SP-5000M-PMCL-CX; JAI Inc.) which has resolution of 2560 × 2048 pixel and capable of taking images up to 134 fps was employed. The existing LabView CVI 2010 code was modified in order to collect an image every 5 minutes till the end of the experiment as shown in Appendix A1. The specifications of the camera are given in Table 4. A macro lens (f2.8-DG Macro; EX SIGMA Inc.) was attached to the camera along with 34 mm and 20 mm extension tubes which provided the field of view of 14 mm × 11 mm. In this experiment exposure time of 800 μs was used to bring more light into the camera. This setting was especially used in combination with Teflon sheet to overcome the decrease in the intensity count due to the calcium carbonate nucleation on acrylic windows located in front of camera, which would otherwise hinder the transparency and hence the quality of image acquisition. The camera was focused at the center of flow cell using dial gage indicator.

The specifications of the camera used in PSV experiment used are shown in Table 4. A high speed camera (FASTCAM Mini WX50; Photron Inc.) was used along with the same macro lens to collect 1000 images at 2000 fps. This camera provides full resolution of 2048 × 2048 pixels till the frame rate of 750 fps.

Therefore it reduced available resolution to 1280 × 1088 pixels after frame rate was increased to 2000 fps, which was sufficient to capture the area of interest at the slot entrance equivalent to 10 mm × 8.5 mm. The average diameter of tracer particles was about 4 to 5 pixels and the displacement was lower than 10 pixels for given experimental conditions.

Table 4: Camera specifications in scaling and PSV experiment

Camera	SP-5000M-PMCL-CX	SP-5000M-PMCL-CX
Resolution	2560 × 2048 pixels	1280 × 1088 pixels
Sensor type	CMOS	CMOS
Image acquisition rate	1 frame every 5 minutes	2000 fps
FOV	14 mm × 11 mm	10 mm × 8.5 mm
No. of images captured	till end of the experiment	1000
Pixel format	Mono 8	Mono 16
Exposure mode	Timed	Timed
Exposure time/Shutter speed	800 µs	1/5000 sec to 1/35000 sec

3.1.4 LED light source

A LED light source (Pulsar 320; Advanced Illumination Inc.) was used as the source of background illumination during the scaling experiment. When the scale grows on the side walls it casts shadow on the camera sensor and creates contrast for the every frame captured. It was later was processed to estimate the growth rate of calcium carbonate in the rectangular slot. The light source was operated in continuous mode at its maximum intensity during the scaling experiment. The benefit of this light source is that it provides incoherent light and is reliable for long term use. Also the light sources has a green light with spectral

wavelength of 520 nm and it complies with the optimum quantum efficiency for the camera sensor.

During the PSV experiment, a high power LED source (ILA.LPS 3, ILA5150 GMbH Germany) had to be used considering the high frame rate of 2000 fps employed in the experiment. The LED light source was operated in continuous mode at frequency of 300 kHz to provide the background light and freeze the motion of tracer particles.

3.2 Particle Shadowgraph Velocimetry (PSV) experiment

To effectively investigate the scale growth phenomenon in the flow cell, the contribution of fluid flow and its mechanics needs to be understood. This study used particle shadowgraph velocimetry, an experimental flow visualization technique which works on the similar principles of particle image velocimetry (PIV). The technique of PIV is employed to measure the instantaneous velocity field by tracking the displacement of tracer particles in between frames with short interval of time. The advantages of particle image velocimetry is that it provides the velocity information for the entire flow field, and hence deemed to be a whole field technique. It is also known as a non-intruding method as it does not interfere the flow field [91].

A schematic in Figure 11 shows the working principle behind the PSV operation. The PSV technique broadly consists of flow visualization and image processing stages. The typical PSV set-up consists of a high speed camera with a background light source for illumination. The fluid flow is seeded with small particles in order to identify the flow field. The shadow is recorded on the camera

sensor for the particles which are in focus for given depth of field. Generally the shadowgraph technique utilizes the refraction between the medium and object being studied. The light rays do not collide with the object provide a bright background, whereas the light interacting with the object or particles is made to refract and thus disappear. Hence, the particles appear dark on the camera sensor [92]. The captured images are later processed to track the particle displacement and estimate the velocity field based on the frame rate employed in the experiment.

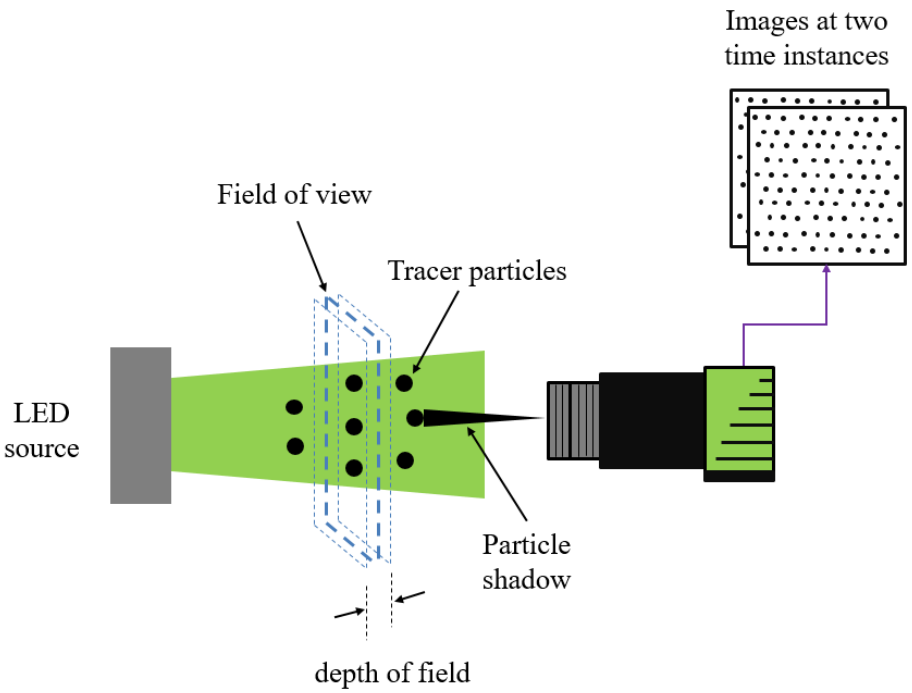

Figure 11: Schematic of Particle shadow velocimetry set-up

In this experimental study, PSV was used to measure the two dimensional velocity field, and from this determine the pressure field. During flow visualization, the tracer particles of 20 μm diameter hollow glass spheres (Dynoseeds TS20, Microbeads) with a density of 1.10 g/cc were added in the water in order to identify the flow field and its motion. The tracer particles casted their shadow onto the high speed camera (FASTCAM Mini WX50; Photron Inc.) from the background light

source (ILA.LPS 3, ILA5150 GMbH Germany). The fluid and tracer particle were continuously stirred using the magnetic stirrer during the experiment. The experiment was undertaken at given flow rates and 1000 images were captured at 2000 fps in time series mode at the desired plane within area of interest at the slot entrance equivalent to 10 mm × 8.5 mm. The frame rate of 2000 fps was sufficient to capture the particle motion as the particle displacement was observed to be less than 10 pixels, so it could be potentially tracked for around next 100 frames considering the available resolution of 1088 pixels in the vertical direction.

3.2.1 Tracer particles

PIV is described as a non-intrusive method which distinguishes the particle displacement for a short time interval without disturbing the flow field. However, it is an indirect method since it measures the velocity of tracer particles instead of the fluid flow [91]. This can hold true only if the tracer particles do not induce any forces in the fluid medium as well as follow the fluid flow with a smaller settling velocity [91]. Therefore, the effective interaction of tracer particles with surrounding fluid avoids the inconsistencies in the velocity measurement. To assess if the particles meet this requirement, a non-dimensional number, Stokes number (*Stk*) is determined as follows [91][93]:

$$Stk = \frac{\rho_p d_p V}{18\mu_f} \tag{16}$$

where, ρ_p and d_p are the density and diameter of tracer particle respectively, V is flow velocity and μ_f is the viscosity of the fluid. This equation shows that Stokes number is a function of fluid properties i.e. flow velocity and viscosity, and is affected by the characteristics of the tracer particles such as density and the

diameter. Therefore it provides good basis for the suitable selection of tracer particles and understand if they follow the fluid flow and eventually allow for the indirect measurement of fluid velocity.

The settling velocity (v_s) of the particle characterizes if the particle will remain suspended in the fluid medium and is calculated as [93]:

$$v_s = \frac{g(\rho_{p-}\rho_f)d_p^2}{18\mu_f} \tag{17}$$

where, ρ_f is the fluid density. This shows that settling velocity depends upon the density of tracer particles along with the density and viscosity of the fluid. Therefore density of particles and fluid should be equivalent in order to particles remain suspended in the fluid [91].

The Stokes number and settling velocity were calculated for the tracer particles considered according to equation (16) and (17) considering the water density of 1 g/cc, viscosity of water equal to 0.001 Pa-s and maximum flow rate of 1500 ml/hr. As per the calculations, the Stokes number is 4.89×10^{-7} which is much lower than 1, hence it is expected that the tracer particles will follow the fluid motion. Also the settling velocity is 1.1×10^{-5} m/s, hence it can be concluded that the gravitational forces will not affect the movement of tracer particles and will remain suspended in the fluid flow [91][93].

3.3 Scaling (scale build-up) experiment

For the scale build up experiment, two different aqueous solutions saturated with calcium chloride dihydrate (C79-500; Fisher Chemical Inc.) and sodium carbonate (S263-500; Fisher Chemical Inc.) were prepared with their concentration equal to 0.01 M. The distilled water with pH 7 was used to prepare the brine solutions and were kept in a vacuum chamber for a certain time before starting the experiment in order to remove any air bubbles from it. The brine solutions were continuously stirred throughout the experiment with magnetic stirrer to assure that the solution is homogenously saturated. The aqueous solutions were separately pumped using the peristaltic pump and are mixed in a chamber shown in Figure 8(a) and Figure 9(b) after which the combined flow enters the flow cell. The aqueous solution of the calcium chloride dihydrate and sodium carbonate passes through the vertical flow cell in a single pass and discharged to effluent after it exits the flow cell. The scale grows on the surfaces by nucleation and diffusion process ultimately plugging the narrow slot. The images captured during the experiment were processed later to estimate the change in the slot width as a function of time. At the end of the experiment, calcium carbonate scale deposited in the flow cell was cleaned with diluted 2.5% hydrochloric acid, followed by flushing the water through the flow cell for next half an hour.

3.3.1 Pressure drop measurement

The corresponding increase in pressure drop due to subsequent growth of calcium carbonate crystals was measured with the pressure transducer (DP15-36; Validyne Inc.) across the slot. The change in pressure alters the diaphragm position, and invariably changes the reluctance of the two sensing coils which ultimately

produces the electrical signal. The voltage demodulator (Model CD-15; Validyne Inc.) processes the signal from the pressure transducer and provides voltage as DC output signal. It was collected at the rate of 100 data points per second using a data acquisition system (NI-9219; National Instruments Inc.) through analog input recorder as an interface (Matlab Data Acquisition Toolbox 3.14; Mathworks Inc.) as shown in Figure 12. The data acquisition system supports voltage measurements up to range of ±60 V but a range of 0-6.5 V is used in this experimental study which was rather limited by the output of the voltage demodulator.

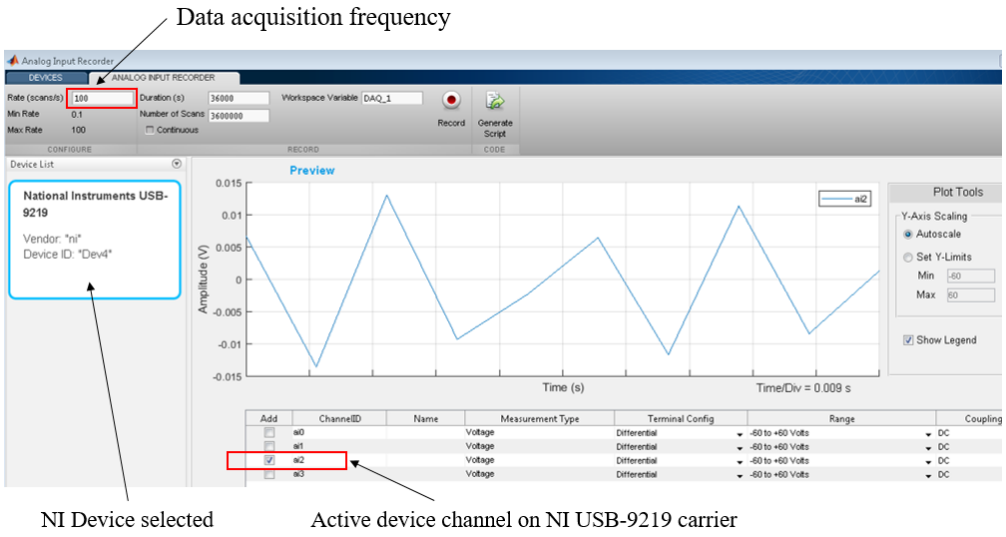

Figure 12: Data acquisition interface

In this study, the differential pressure of 17 kPa is used as a criterion to manually stop the experiment. It corresponds to the voltage of 6.5 V and is visible on the Matlab analog input recorder interface in real time. Based on this criterion of 17 kPa, next available diaphragm (DP15-34; Validyne Inc.) with capacity of 22 kPa was chosen to utilize its full pressure range and get good accuracy. The pressure transducer has accuracy of ±0.25% at full scale so the corresponding noise

would be 0.05 kPa for the capacity of 22 kPa. It can sustain overpressure up to 200% of the full scale.

The pressure transducer was calibrated with pressure calibrator (DPI-603, Druck Inc.) before its use. The voltage demodulator has two knobs to set the pressure transducer to a desired zero and span. During the calibration, the zero knob was set to 0 V corresponding to 0 kPa pressure and span was set to 6.5 V for the pressure of 17.2 kPa whereas the pressure transducer was open to atmosphere. The zero knob decided the intercept on y-axis whereas span determined the slope. The linear dependence of voltage (V) output on the pressure (P) applied during calibration is shown in Figure 13 and represented by:

$$V = 0.377 \times P \tag{18}$$

This relation was further used to obtain the pressure drop caused by the scale formation by multiplying a constant of 2.65 with the voltage output from the data acquisition system.

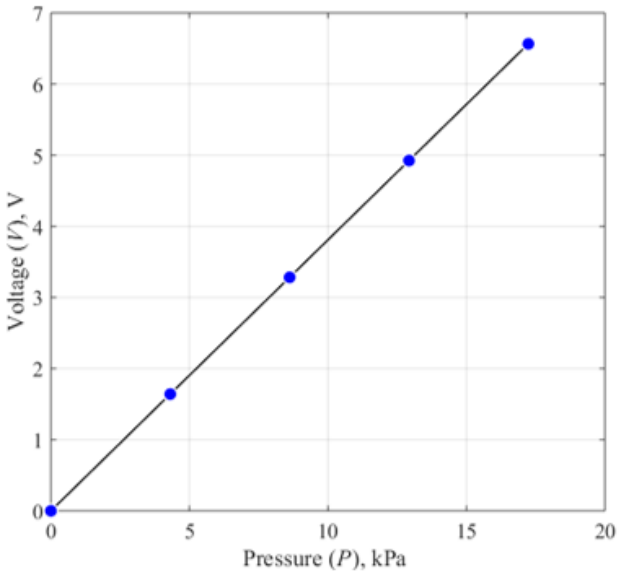

Figure 13: Pressure-voltage relation during pressure transducer calibration

3.3.2 Prediction of solution supersaturation

In order to determine if the aqueous solution would be supersaturated and form suitable condition for the nucleation and growth of calcium carbonate, stoichiometric calculations were performed in a chemical equilibrium modeling freeware (Visual MINTEQ V3; KTH Sweden) [94]. It considers the amount of salt used as an input and provides information such as saturations index, type of polymorph formed and pH at given operating temperature. The modeling approach takes into account a mass balance and change in Gibbs free energy to find ionic strength (*IAP*) and equilibrium constant (K_s) [94] to define a saturation index (*SI*) such that:

$$\text{Satuation Index } (SI) = \log(IAP) - \log(K_s) \tag{19}$$

The saturation index is therefore the difference between the ionic strength and solubility constant of the precipitate. If the solution is under saturated, the value of saturation index will be negative and scale formation will not occur. If the saturation index value is positive, the solution will be supersaturated and increases the likelihood of the scale formation. The simulation results show that the value of saturation index is greater than one for all forms of calcium carbonate i.e. aragonite, calcite and vaterite as shown in Figure 14. Hence the aqueous solutions of calcium chloride and sodium carbonate with concentration of 0.01 M can be used in the scaling experiment as it indicates ideal scenario for the scale formation. The results also show that the pH value increases to 10.8 after mixing the two solutions containing cations and anions. Whereas the pH value of 11.12 was measured physically by mixing the two aqueous solutions at 0.01 M using a pH meter (AR50; Fisher Scientific Inc.) before the experiment.

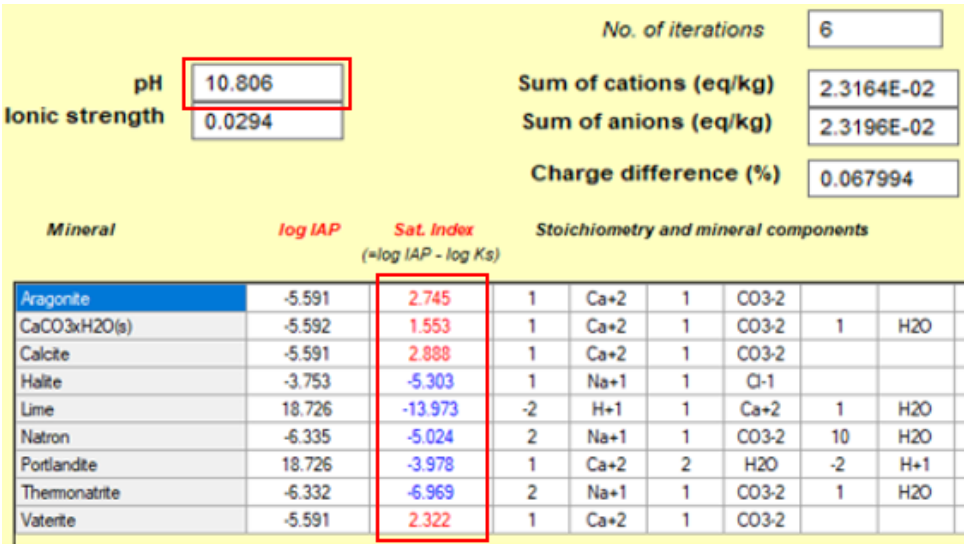

No. of iterations 6

pH 10.806

Ionic strength 0.0294

Sum of cations (eq/kg) 2.3164E-02

Sum of anions (eq/kg) 2.3196E-02

Charge difference (%) 0.067994

Mineral	log IAP	Sat. Index (=log IAP - log Ks)	Stoichiometry and mineral components					
Aragonite	-5.591	2.745	1	Ca+2	1	CO3-2		
CaCO3xH2O(s)	-5.592	1.553	1	Ca+2	1	CO3-2	1	H2O
Calcite	-5.591	2.888	1	Ca+2	1	CO3-2		
Halite	-3.753	-5.303	1	Na+1	1	Cl-1		
Lime	18.726	-13.973	-2	H+1	1	Ca+2	1	H2O
Natron	-6.335	-5.024	2	Na+1	1	CO3-2	10	H2O
Portlandite	18.726	-3.978	1	Ca+2	2	H2O	-2	H+1
Thermonatrite	-6.332	-6.969	2	Na+1	1	CO3-2	1	H2O
Vaterite	-5.591	2.322	1	Ca+2	1	CO3-2		

Figure 14: Stoichiometric calculations in Visual MINTEQ software

3.4 Data processing methodology

This section discusses the steps taken to process the experimental data. It also explains the methodology followed to derive the 2D-velocity and pressure field from the particle shadowgraph velocimetry experiment as well as to obtain the change in slot width due to subsequent growth of calcium carbonate in the scaling experiment. The data processing was undertaken by first calibrating the images.

3.4.1 Image calibration method

Calibration is the procedure to acquire the relationship between camera's dimensions with the physical units i.e. number of pixels with mm or inch. The calibration was done in a commercial software (DaVis 8.4, LaVision GmbH) used to derive the velocity field. The standard measurement device was held in focus and an image was taken by the camera. The corresponding number of pixels from the image were mapped with the physical dimensions as shown in Figure 15. It needs to be ensured that the camera is in alignment with the object in order to avoid any

error. Based on how many pixels were associated with a known distance, the ratio was obtained to convert pixels into the physical dimension. The calibration has to be repeated if the particular camera settings such as focal length or zoom are changed.

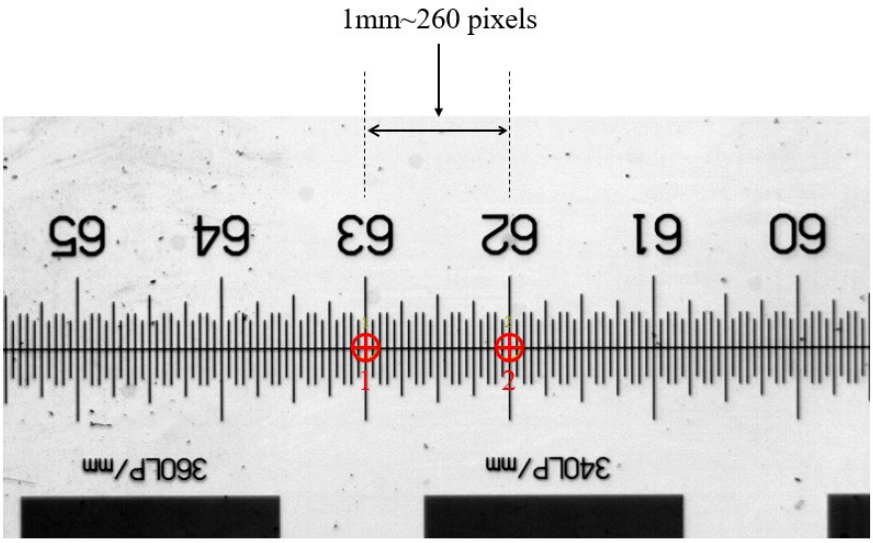

Figure 15: Image calibration

3.4.2 Derivation of 2D-Velocity field from PIV data

There are three basic steps involved in processing the PIV data to obtain the velocity field. First, image preprocessing is implemented to remove illumination inconsistencies in order to achieve the unambiguous displacement correlation peak. Then a sum of correlations method was used after the image preprocessing stage to calculate the velocity vector field. The vector field calculation method is followed by the vector post-processing step to remove the outliers and obtain the averaged velocity vector map.

For the PIV correlation algorithm, the vector peak detection is influenced by the inconsistencies in the image intensity. The peak detection will be accurate if

there is better contrast available between the particle and background intensity [95]. Also, different aspects such as out-of-plane motion of tracer particles, arbitrary particle shape and size as well as inconsistent particle brightness results in erroneous errors in the vector peak detection, and strongly affect the quality of velocity measurement [91,96]. Therefore, an image preprocessing scheme is employed to manipulate the images and enhance the accuracy of the vector calculation in PIV.

In this study, a commercial software (DaVis 8.4, LaVision GmbH) was used to process the images collected during the PSV experiment. The first step employed in preprocessing was the image inversion using a scale length and arbitrary factor. The need to invert the images arises since the particle and background appears dark and brighter respectively in PSV experiment. In this approach, the intensity inversion is based on the image intensity that is determined using a specific equation and considering the minimum and maximum local intensities for a particular scale length in pixels and the arbitrary factor as [97]:

$$\text{Image intensity} = L_{min} + \text{Factor} \times (L_{max} - L_{min}) \tag{20}$$

where, L_{min} is local intensity minimum and L_{max} is local intensity Maximum.

As a next step, another correction was applied to normalize the local particle intensity considering the length in pixels. This option is particularly useful when the variation in intensity is significant. The implementation of this correction technique results in normalizing the intensity across the particles and ensures that the smaller particles also participate in vector peak detection [97]. A geometric and algorithm mask was also employed to decrease the noise in the background as well

as the processing time. Figure 16(a) and (b) compare the images before and after the pre-processing respectively. It shows the inverted image as particles appear bright and background dark as opposite to the original image. Also, every particle has consistent intensity across the image due to the use of particle intensity normalization scheme.

(a)

(b)

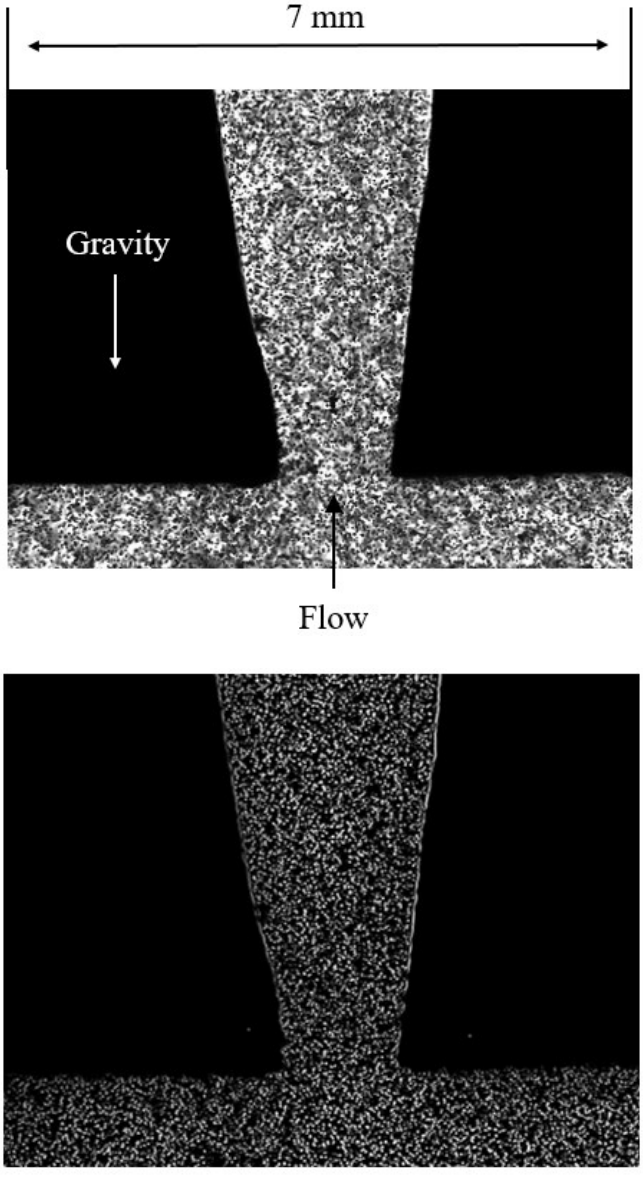

Figure 16: Image preprocessing in PIV, (a) Raw image and (b) Preprocessed image

The basic principle to derive the velocity field is to divide the field of view or area of interest into small interrogation windows and trace the particle in between two

successive frames by freezing the motion of the tracer particles. The particle displacement is used to calculate the velocity field by considering the time lag in between the two frames employed. This process is subsequently repeated for remaining interrogation windows.

In order to obtain the vector field, a multi-pass sum of correlation with interrogation window overlap as well as decreasing window size along with weight option was employed in the commercial software (DaVis 8.4, LaVision GmbH). This selection ensures more vectors per unit area and hence provides higher spatial resolution. However, it increases the computation time accordingly. The three passes were initially conducted with 64 × 64 interrogation window and 50 % overlap. In this initial step, a default square form was chosen for the interrogation windows. For the final stage, four passes of 32 × 32 window size were considered with 87 % overlap. However, for this stage an elliptical form with 2:1 weighting option was chosen for the interrogation window. This option internally chooses an interrogation window of twice the size in vertical direction as compared to horizontal, and the calculations are performed such that the integral of all weighed pixels is equivalent to the interrogation window selected [97].This setting is useful when the flow direction is significant in a particular direction. The idea behind this setting is to ensure more pixels in the dominant flow direction in order to obtain a dominant correlation peak [97].

The PIV sum of correlation algorithm was selected as it's extremely efficient in cases of poor flow seeding, excessive noise or out-of-plane motion in the experiment [97]. The vector field is calculated in three stages as [97]:

$$C_i(x_0, y_0) = I_1(t_1, x_0, y_0) \times I_2(t_2, x_0, y_0) \tag{21}$$

$$C_{avg}(x_0, y_0) = \sum_i C_i(x_0, y_0) \tag{22}$$

$$V_{avg}(x_0, y_0) = \text{Position of highest peak in } C_{avg}(x_0, y_0) \tag{23}$$

First, for every collected image, the sum of correlation calculates the correlation planes (C_i) at position (x_0, y_0) at a particular time instant t by cross-correlation of two image interrogation windows I_1 and I_2 of $n \times n$ pixel each. Then all correlation planes are combined into a single ensemble of correlation planes (C_{avg}). Lastly, a single vector field (V_{avg}) is calculated from all the combined correlation planes as shown in equation (23). This velocity vector then represents the average velocity in the defined correlation window. The vector field calculation method is followed by the vector post-processing step in which erroneous vectors are removed. The 2 × 2 median filter was employed to remove the outliers. The median vector is calculated from the set of neighboring vectors and matched with the center vector. It is then rejected outright if it falls outside of the range of average vectors [97]. The option of interpolation was also selected in order to fill the empty places. The resulting velocity vector field achieved through vector post-processing was stored as *.VC7 file. An in-house code (Appendix A2) was modified and employed to post-process this vector field and obtain the averaged velocity vector map using the commercial software (Matlab 2017a, MathWorks Inc.). The velocity map is obtained by averaging 1000 raw images. Figure 17 shows the resulting velocity vector map for a laminar flow passing through a straight slot profile with sudden contraction. In the plot, 1 out 2 vectors are shown in x-direction, whereas, 1 out of 9 vectors are shown in y-direction. Also the horizontal and vertical dimensions of the channel are normalized with the entrance width, whereas, the

velocity scale is in absolute dimensions i.e. mm/s. The length of the vectors is more in regions with higher velocity, where the vector length will be short where there isn't enough flow movement.

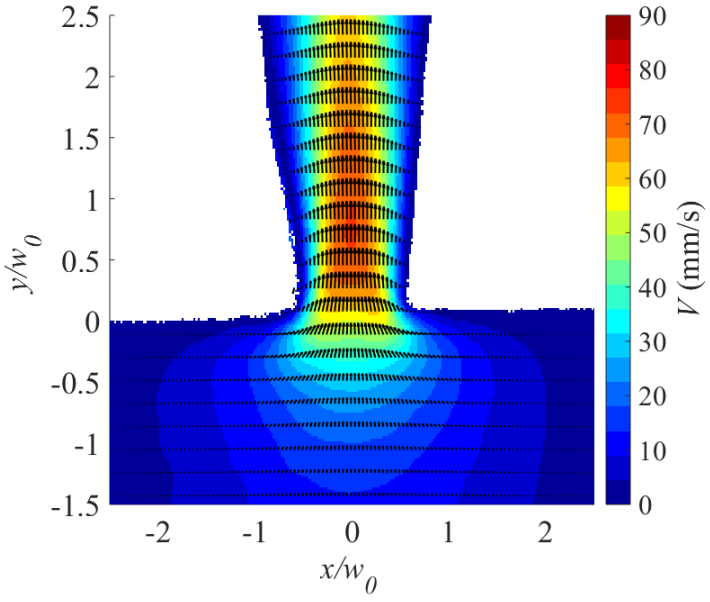

Figure 17: An example resultant 2D-velocity field of the flow into and through a slot.

3.4.3 Computation of 2D-Pressure field from PIV data

In this study, the velocity data obtained from PIV was used to compute the two-dimensional pressure field using the Poisson equation [98]. The Eulerian perspective is considered which uses the fixed frame of reference as opposite to the Lagrangian method in which a particular particle is tracked. The Navier-Stokes equation provides the avenue to associate the velocity field with the pressure field as [98–101]:

$$\nabla p = -\rho \frac{\mathrm{D}\mathbf{u}}{\mathrm{D}t} + \mu \nabla^2 \mathbf{u} \tag{24}$$

where, p is the pressure, ρ is the density, $\mathbf{u}$ is the velocity, μ is the viscosity of the fluid, ∇ is the divergence operator. The Poisson equation is obtained by applying divergence operator on the Navier-Stokes equation as:

$$\nabla^2 p = \nabla.(\nabla p) = \nabla.\left(-\rho\frac{\mathrm{D}\mathbf{u}}{\mathrm{D}t} + \mu\nabla^2\mathbf{u}\right) \tag{25}$$

where, D$\mathbf{u}$/Dt is the total or material derivative which includes the local and convective part of acceleration:

$$\frac{\mathrm{D}\mathbf{u}}{\mathrm{D}t} = \frac{\partial u}{\partial t} + (\mathbf{u}.\nabla)\mathbf{u} \tag{26}$$

By assuming the flow is steady, and incompressible i.e. $\nabla.\mathbf{u} = 0$, equation (25) becomes:

$$\nabla^2 p = -\rho\nabla.(\mathbf{u}.\nabla)\mathbf{u} \tag{27}$$

which can also be expressed as:

$$\frac{\partial^2 p}{\partial x^2} + \frac{\partial^2 p}{\partial y^2} = -\rho\left\{\left(\frac{\partial u}{\partial x}\right)^2 + 2\frac{\partial v}{\partial x}\frac{\partial u}{\partial y} + \left(\frac{\partial v}{\partial y}\right)^2\right\} \tag{28}$$

This Poisson equation can be then discretized by using second order finite difference method with step size of h as [102]:

$$\frac{\partial^2 p}{\partial x^2} = \frac{p(x_{i-1}, y_i) - 2p(x_i, y_i) + p(x_{i+1}, y_i)}{h^2} + O(h^2) \tag{29}$$

$$\frac{\partial^2 p}{\partial y^2} = \frac{p(x_i, y_{i-1}) - 2p(x_i, y_i) + p(x_i, y_{i+1})}{h^2} + O(h^2) \tag{30}$$

$$\frac{\partial u}{\partial x} = \frac{u(x_{i+1}, y_i) - u(x_{i-1}, y_i)}{2h} + O(h^2) \tag{31}$$

$$\frac{\partial u}{\partial y} = \frac{u(x_i, y_{i+1}) - u(x_i, y_{i-1})}{2h} + O(h^2) \tag{32}$$

An in-house code (Appendix A3) was executed in commercial software (Matlab 2017a, MathWorks Inc.) to compute the 2D-presure field from the velocity field obtained by PIV and using the second order finite difference scheme to solve the Poisson equation as explained earlier. Figure 18 shows the pressure field computed for the 2D-velocity field shown in Figure 17 for a laminar flow field passing through the sudden contraction. Similarly the horizontal and vertical dimensions of the channel are normalized with the entrance width, whereas, the pressure magnitude is in absolute dimensions i.e. Pa. The contour plot displays isolines with no edge color and the areas between the isolines are filled with 12 contour colors. The green color shows areas with low pressure. The pressure at the start of domain or on the edges of channel in the plot is zero due to the application of the Dirichlet boundary condition.

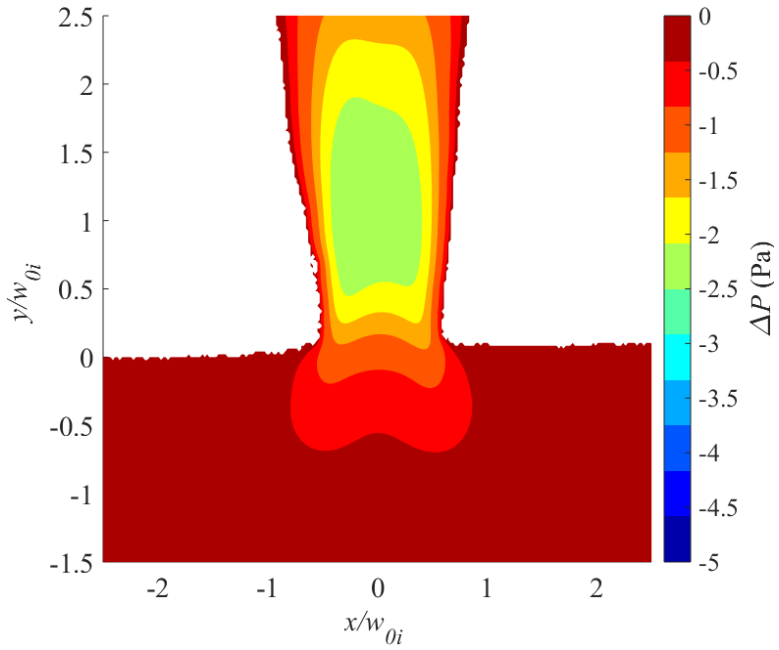

Figure 18: 2D-Pressure field

3.4.4 Image processing for calcium carbonate scaling experiments

The scaling experiments involves image acquisition at a periodic interval to investigate the growth of calcium carbonate on the side walls of metallic flow cell. The subsequent scale growth reduces the slot width until it's completely plugged. So this section basically explains the steps taken to process an image acquired during the experiment in order to estimate the slot width.

As described earlier in Chapter 3, the scaling experiment captures the images in the backdrop of a light source. So the growth of calcium carbonate hinders the background illumination and casts shadow on the camera sensor. Therefore it fundamentally affects the light intensity which would reduce due to subsequent crystal growth. The camera employed has pixel format of mono 8. Therefore, this 8- bit depth camera could provide 2^8 i.e. 256 gray shades per pixel, if the CCD is fully saturated. In this study, when there is no scale present within the slot, the image being processed has maximum intensity count of 255 with a factor of 1as shown in Figure 19(a). It also shows a dark location at the extreme side of the image with an intensity count of 20 and a factor of 0.078. Figure 19(b) shows the intensity count of 27 with a factor of 0.094 within the slot when it's completely plugged. Ideally these intensity counts should be equivalent to zero since they are captured at dark location. However, the reason is the high camera exposure time of 800 μs used in the experiment, which brought more light into the camera and amplified/saturated the intensities across the image.

(a)

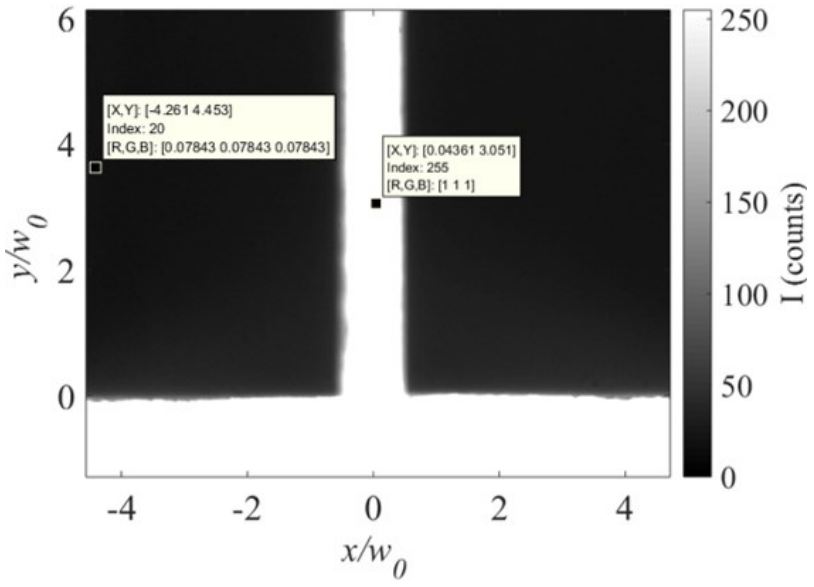

(b)

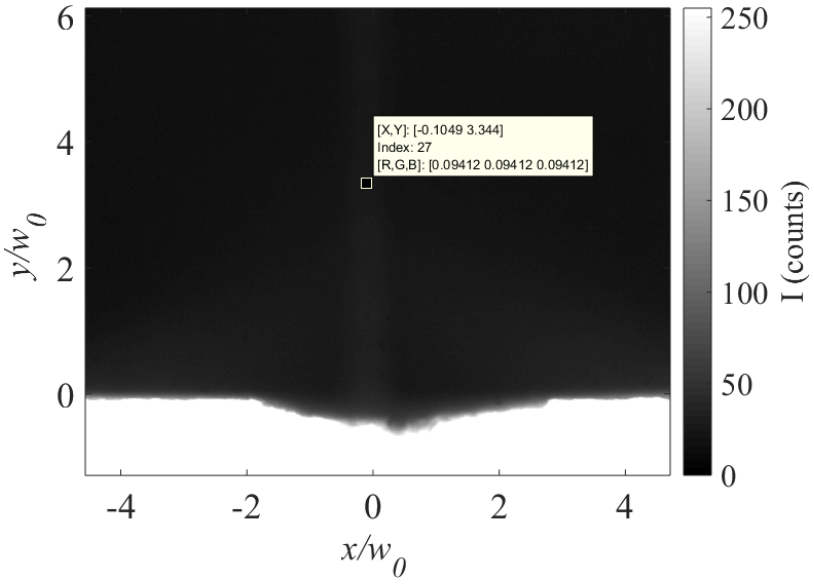

Figure 19: Image intensity count (a) for a clean slot and (b) a plugged slot

The images captured during the experiment were processed in commercial software (Matlab 2017a, MathWorks Inc.) using a peak prominence method. An in-house code (Appendix A4) is built which makes use of the function *findpeaks*. It detects a local maxima or peak of the given input signal. The code further utilizes the concept of peak prominence. The prominence of a peak decides how important it is in comparison to other peaks. It locates an intensity peak if it exceeds given intensity threshold or peak prominence of intensity count equal to 75 considered in

this study. So it filters out remaining peaks which doesn't meet this criteria. The care has been taken to add a small number in an increasing order along the length of the intensity vector in horizontal direction in order to avoid the duplicate peak e.g. Figure 20(a) originally has a plateau with an intensity of 255. However, since a small number is added in an increasing order, the intensity at the left edge of the plateau is 255, whereas, at the right edge it's 255.001. Therefore if there is a plateau, the plot will always detect a peak at the right edge of the plateau as seen in Figure 20 (a). The code then records the full width at half prominence as the local slot width. This process is repeated across the length of the slot starting at the slot entrance, and the slot width at real time instant is obtained by averaging all local slot widths obtained across the slot length. The use of full width at half maximum is a common practice in signal processing [103–105]. It was assumed during processing that the scale grows evenly on side walls of the flow cell at any instance of time.

Figure 20(a) and (b) respectively show the horizontal intensity profile located at the middle of the slot length for the images shown in Figure 19(a) and (b). In Figure 20 (a), the intensity peak has reference of 20 count and its highest value is 255 count. So the prominence of this peak is 235 and is higher than the considered criteria of 75 hence it detects the peak and records the local slot width of 270 pixels at half prominence of 135. Figure 20 (b) shows the peak is undetected for the plugged slot as it doesn't meet the said criteria. The width was later converted to millimeters using the calibration process described in section 3.4.1.

(a)

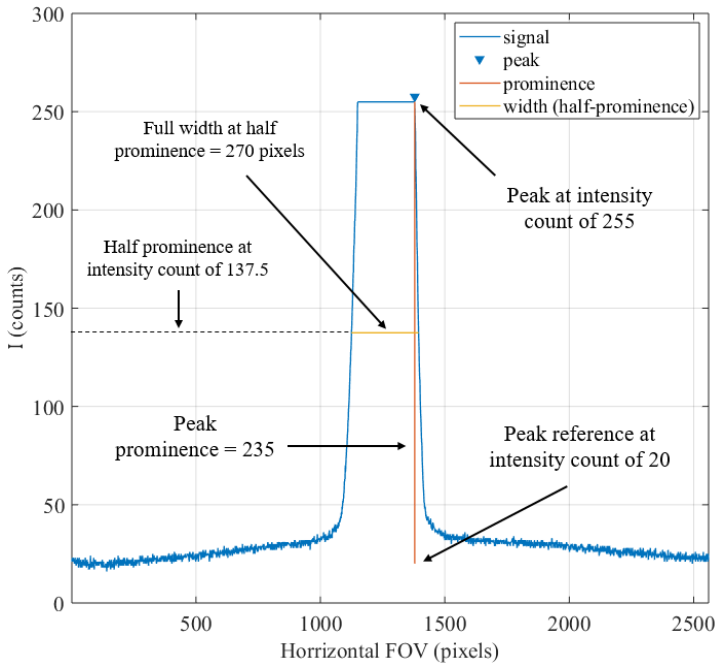

(b)

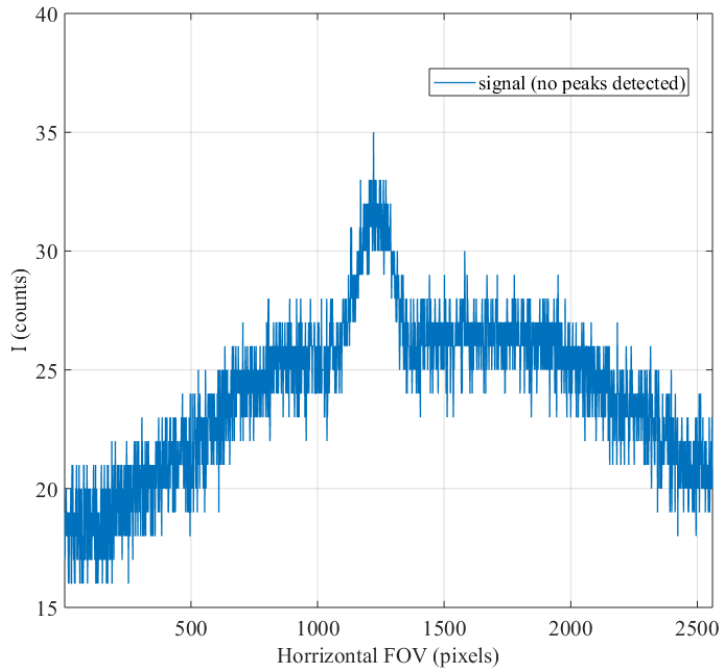

Figure 20: Intensity peak detection (a) for a clean slot and (b) a plugged slot

The width estimation process is repeated for all the images captured till the slot is plugged in the experiment. The code processes consecutive images and stores the current slot width in an array. Now it has an instantaneous value of slot width for every 5 minutes. This information is used to plot how the slot width, *w(t)* changes as a function of time (*t*) as shown in Figure 21. The instantaneous slot width

is normalized with the slot width at time zero (w_0) for a clean channel i.e. at the start of the experiment. The slot width reduces in a linear fashion as the time progresses.

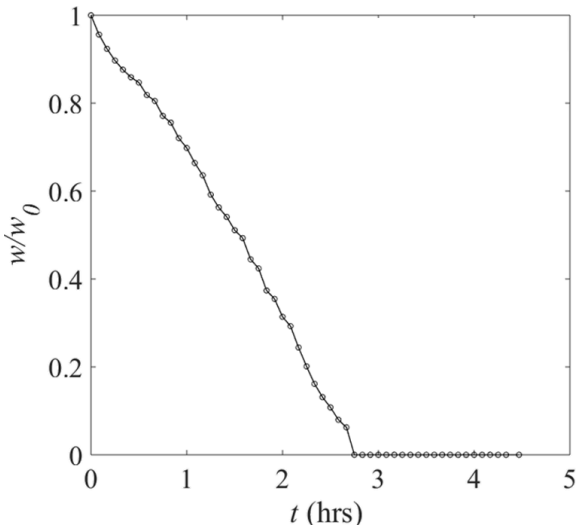

Figure 21: Change in slow width vs time plot

3.4.5 Estimation of scaling time

The differential pressure at the beginning of the scaling experiment when the fluid passes through sudden contraction in given flow cell is minimal. However, in order to understand the effect of resulting flow behavior on instantaneous scale formation and vice-versa, the initial differential pressure value provided by the pressure transducer is offset to zero. Hence the change in the pressure drop measured during the experiment is only due to the subsequent growth of calcium carbonate crystals. The differential pressure rises with respect to time as the slot width reduces. However, it increases rapidly when the opening in slot is very slim. The slot gets plugged subsequently resulting in excessive flow obstruction.

In order to compare the effect of different geometries and flow rates, the time taken to reach the magnitude of 17 kPa is defined as the scaling time as shown

in Figure 22. It will help to understand the experimental conditions which would prompt the faster nucleation and crystal growth of calcium carbonate.

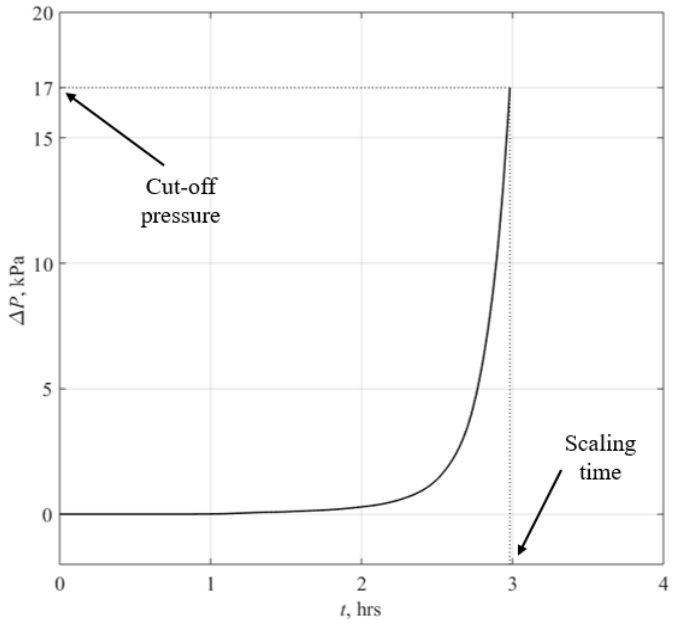

Figure 22: Pressure drop vs time curve

3.4.6 Uncertainty analysis

In experimental work, the error is defined as the variation between calculated and true value [106,107]. However, the error cannot be estimated since the true value is not known. There are various parameters such as accuracy of measuring devices, variation in readings or design/manufacturing tolerances may induce the error [106,107]. Broadly there are two types of uncertainties namely random and bias uncertainty. The confidence interval represents the total error due to uncertainties. The confidence of 90% means that 90% of the times the variations are within the acceptable range. The total uncertainty for a parameter Y as a function of independent n variables ranging from x_1 to x_n can be defined as [106]:

$$u_y = \sqrt{\sum_{i=1}^{n} (\partial x_i \frac{\partial Y}{\partial x_i})^2} \tag{33}$$

where, ∂x_i is the uncertainty of the independent variables and $\frac{\partial Y}{\partial x_i}$ represent the sensitivity of Y on given independent variables. The standard deviation of *x* is given as [106]:

$$s_x = \sqrt{\sum_{i=1}^{n} \frac{(x_i - \bar{x})^2}{n-1}} \tag{34}$$

$$s_{\bar{x}} = \frac{s_x}{\sqrt{N}} \tag{35}$$

where, s_x is the standard deviation, $s_{\bar{x}}$ is the standard error, N is the sample size and $s_{\bar{x}}$ is the mean value of the samples.

In PIV, the random errors are often associated with the tracer particles as well as interrogation windows and resolution [74]. The random collisions with other particles may impart Brownian motion. However, the Brownian motion becomes less apparent for tracer particles with diameter above 10 µm [108]. The error associated due to interrogation windows and resolution is because of inconsistency in the image displacement of tracer particles, and larger particles may induce the error because they take more pixels [74]. The uncertainties in PIV measurement can be reduced by using high frames to freeze the motion, also ensuring the settling velocities of the particles is small and by using more number of images for correlation along with small interrogation windows as well as by using sum of correlation method for processing the vector field in case of poor flow seeding and out-of-plane motion [97]. In this study a frame rate of 2000 fps was used. It was

sufficient to capture the high flow rate of 1500 ml/hr. Also 1000 images were used in displacement peak correlation using sum of correlation method. The calculated Stokes number and settling velocity were very low so the tracer particles will remain suspended in the fluid flow and will also follow the fluid motion.

The experiments will have uncertainty arising from the sensitivity of the measuring devices. However, calibration of the devices is the most reliable way to reduce the errors. In scaling experiment, the camera is focused at the center of the flow cell using dial gauge indicator in order to achieve better contrast between the scale getting formed and background illumination. After the experiment, the camera's natural units i.e. number of pixels are calibrated with the physical units to avoid any distortion and obtain accurate estimation of slot width in the flow cell. The peristaltic pump was calibrated before the experiment to reduce any uncertainty arising from the stiffness of the tubing used for the delivery of aqueous solutions. Based on the calibration, the error for the peristaltic pump was ±2 ml for a fluid delivery of 180 ml. The pressure transducer with capacity of 22 kPa was used for measuring a pressure drop up to 17 kPa. It was chosen to utilize its full pressure range and get good accuracy. Also it can sustain overpressure up to 200% of the full scale. The pressure transducer has accuracy of ±0.25% at full scale so the corresponding noise would be 0.05 kPa for the capacity of 22 kPa.

3.4.7 Data repeatability

In scaling experiment, the change in slot width and pressure drop are measured with respect to time. All experiments were repeated three times to provide insights into the repeatability of the experiments. Figure 23(a) and (b) shows the repeatability of change in slot width and pressure drop for the three experiments

collected for the straight slot profile and flow rate of 1200 ml/hr. The plots show that slot width reduces and pressure drop increases as the time progresses due to calcium carbonate growth, and the change in slot width has a linear behavior. The slope of the reduction in slot width obtained by linear regression can be considered as the growth rate at which the calcium carbonate grows within the slot. Figure 23(b) provides the information about the scaling time. The pressure drop rises as the calcium carbonate grows and the slot width reduces. The time taken to reach the differential pressure of 17 kPa is defined as the scaling time as described in section 3.4.5

The first observation is that the data in Figure 23(a) and (b) is repeatable. In order to confirm this observation, the standard deviation and error were calculated for the growth rate and scaling time using equation (34) and (35). It measures the variations in the given dataset. As the experiment was performed three times the sample size is 3. The standard deviation and error for the growth rate is equal to 0.0193 and 0.01117 respectively, whereas, the standard deviation and error for the scaling time is equal to 0.101 and 0.0583 respectively. Based on the small values for the standard deviation and error, it can be said that the data is repeatable and follows the normal distribution.

A Teflon sheet was installed adjacent to the acrylic sheets to reduce the nucleation. It was changed after every three experiments. Figure 23(a) shows that the slot width for the first experiment reduces to zero comparatively slower to other two experiments. At the end of the experiment, the flow cell is cleaned with diluted hydrochloric acid to dissolve and remove the scale deposited. However, it appears that there is some residue left on Teflon surface even after cleaning with acid in the

first experiment which caused this difference. Therefore it can be said that the first experiment conducted doesn't have any influences. Hence the change in slot width and pressure drop curve of first experiment are considered to plot and calculate other dependent results. This is considering that the standard deviation and error for these two measured parameters is low, and the values are close to the mean values. The other repeatability plots are shown in Appendix A5.

(a)

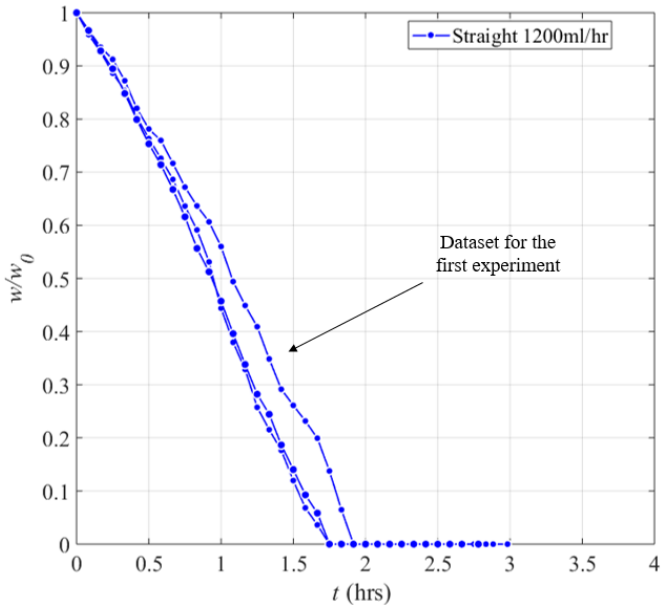

(b)

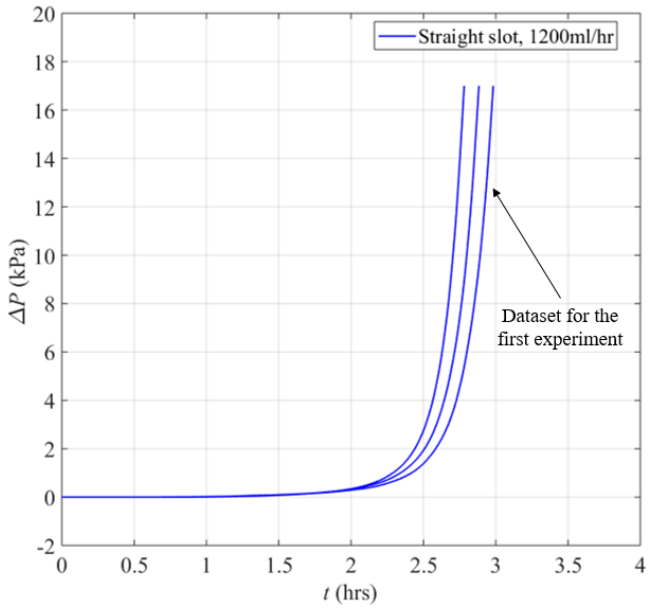

Figure 23: Repeatability of (a) Change in slot width and (b) pressure drop

3.5 Summary

This chapter described the overview of the equipment's, reagents, experimental conditions and procedures employed in the current experimental study. Monitoring the calcium carbonate scale growth and determination of pressure field are anticipated to meet the overall objectives defined earlier. The flow conditions and chemical composition considered suggest that the flow field lies in laminar regime and scale formation phenomenon should prevail. The differential pressure trace history reveals the kinetics and scale growth in real time. The particle shadowgraph velocimetry, a non-intruding method is employed to measure the two-dimensional velocity field due to its simplicity and ease of operation.

It also described the methodology followed to process the experimental data is explained. A multi-pass sum of correlation method was employed to obtain the 2D-veolcity field. The PIV data is further used to compute the pressure field using the Poisson equation which interlinks the velocity and pressure field. The images captured during the scaling experiment were processed using a peak prominence method to obtain the change in slot width in real time.

4 COMPARATIVE STUDY ON THE SCALING PERFORMANCE OF INDUSTRIAL SLOTTED LINER DESIGNS

The slotted liner designs are used in an oil and gas industry to control the sand production which experience critical failure mechanisms affecting the oil production. Therefore these industrial products are designed to discourage the plugging due to migration of fines or sand grains. However, slotted liner designs have rarely been investigated from the scaling failure mode perspective. The goal of this study is to observe the locations where scaling occurs, predict the growth rate of calcium carbonate and evaluate which slotted liner design is superior to mitigate the scale formation. This study will also validate the effect of flow convergence and pressure drop due to sudden geometry contraction on the calcium carbonate build-up and growth. To undertake this, the experiments are conducted at flow rate (Q) of 1200 ml/hr for the three industrial slotted liner devices namely: straight, seamed and keystone.

The first three sections discusses the results for the straight, seamed and keystone designs by comparing the shadow images captured at a certain intervals during the experiments. It helps to visualize how the scale grows in real time, and locate the critical locations which are affected by the fluid flow behavior. The fourth section compares their individual growth rates and scaling time to conclude upon the scaling performance. The last section discusses the two dimensional velocity and pressure fields for two scenarios i.e. for a slot without any scaling and with

scaling at time of 2 hrs to explore the cyclic behavior of scale growth and pressure drop in scaling failure mechanism.

4.1 Results for the straight slotted liner design

A straight slotted liner design is a traditional design with uniform width of 1 mm. It has sharp edged geometry profile at the entrance as shown in Figure 24(a). As a fluid flow supersaturated with scaling ions passes through the slot, nucleation occurs on the side walls made of stainless steel material owing to its rough surface and favorable surface energy gradient. With continuous supply of fresh scaling ions, the calcium carbonate crystals continue to agglomerate and grow within the slot. Figure 24(a)-(f) shows the binary shadow images for the calcium carbonate growth every 1 hour till the slot gets plugged at 4.6 hrs. The binary images are obtained by considering the intensity count threshold of 96 which is 37.65% corresponding to the intensity count of 255. Therefore, the areas below intensity count of 96 will appear as dark, and above which it will appear as white. The horizontal and vertical dimensions of the slot are normalized with the original width at the inlet (w_{0i}) of a clean slot instead of the averaged width (w_0). Whereas, the original width (w_0) and current width, $w(t)$ are obtained by averaging the instantaneous width along the length of the slot as explained in section 3.4.4. The slot width becomes narrower as the time progresses due to scale formation. The scale growth is uniform along the length of slot. However, as the scale grows in lateral direction within the slot, it also grows into the flow at the slot entrance as seen in Figure 24(c)-(d). This will affect the converging behavior of the flow and also alter the flow resistance. Figure 24(e)-(f) shows complete dark images indicating the plugging of the slot.

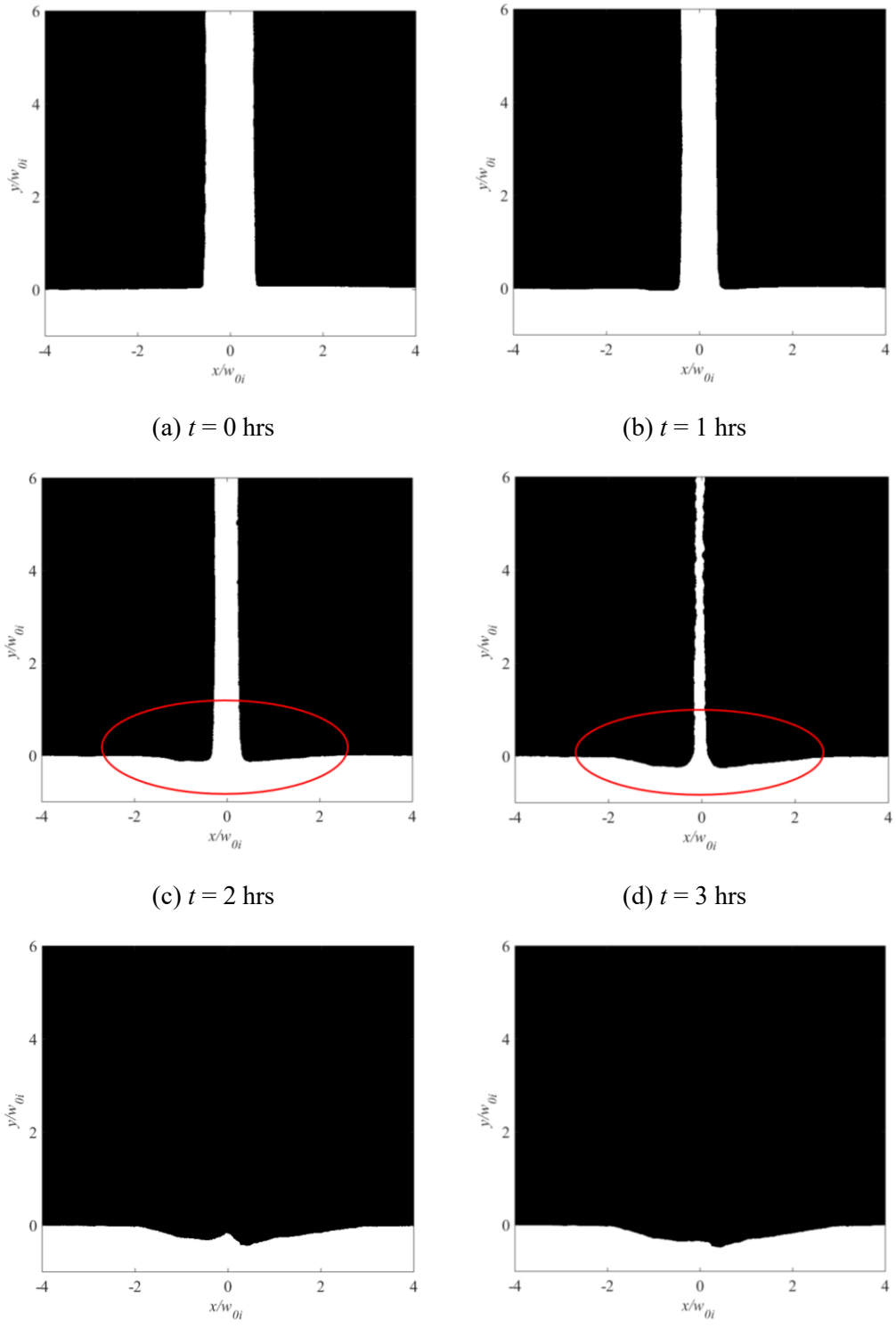

(a) t = 0 hrs

(b) t = 1 hrs

(c) t = 2 hrs

(d) t = 3 hrs

(e) t = 4 hrs

(f) t = 4.6 hrs

Figure 24: Calcium carbonate growth in the straight slot, (a)-(f) at intervals in the experiment

As the scale grows within the slot, its width reduces in real time and approaches the zero at ~3.5 hrs as shown in Figure 25(a). The slope of the reduction in slot width can be considered as the rate at which the calcium carbonate grows within the slot. The growth is linear in nature and can be obtained by linear regression. The estimated growth rate based on the dataset from Figure 25(a) is 0.1987 mm/hr. The pressure drop rises over this time due to a reduction in slot width and asymptotically reaches the maximum when the slot is completely plugged as shown in Figure 25(b). Although the change in slot width is significant after the start of the experiment, the corresponding change in differential pressure due to scale growth is minimal. It only starts to rise predominantly after ~2 hrs of time and reaches the maximum of 17 kPa at 4.5 hrs of time. The slot width approaches to zero at ~3.5 hrs, whereas, the scaling time is 4.5 hrs. So there is a loss of information of 1 hour which indicates the scale structure is porous, and also due to scale growth on acrylic windows to some extent.

(a)

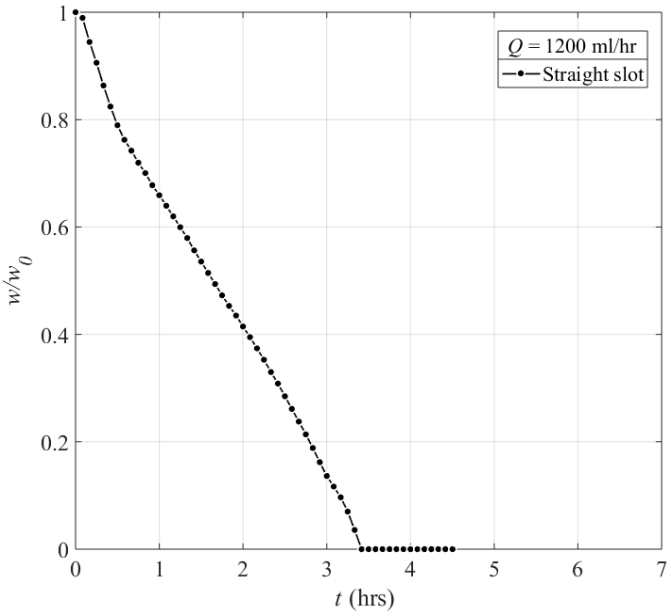

(b)

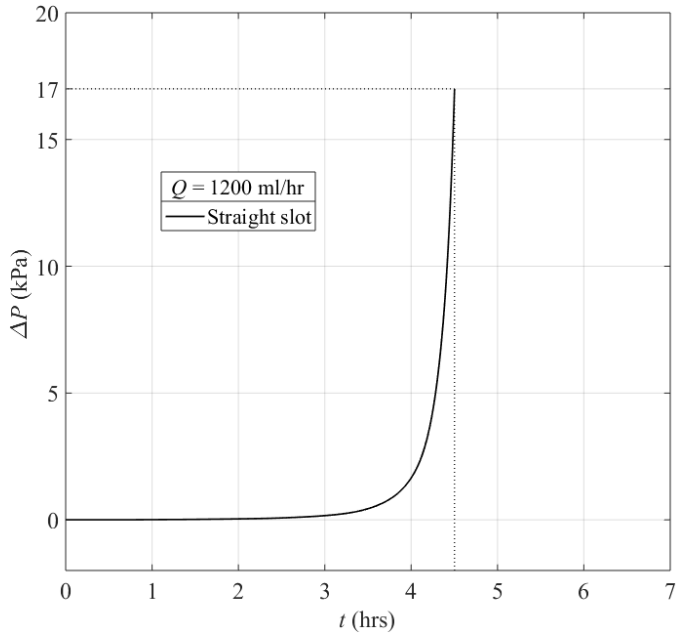

Figure 25: Straight slot (a) Change in slot width, w_0 and w are the original and current slot width respectively and (b) Time history pressure trace

4.2 Results for the seamed slotted liner design

A seamed slotted liner design has width of 1 mm at the inlet with sharp edged profile and 1.5 mm at the outlet (not visible) as shown in Figure 26(a). Seaming the slot makes the slot inlet narrower than the outlet. Figure 26(a)-(f) shows the binary shadow images of scale growth from the start of the experiment

until the slot plugging with an interval of 1 hour. The binary images are obtained with the similar procedure of straight slot design. Since the inlet is narrower, the horizontal and vertical dimensions of the slot are normalized with the original width at the inlet (w_{0i}) of a clean slot. The slot constricts due to the calcium carbonate nucleation and growth. Similar to the straight slot, the scale growth is observed simultaneously in lateral direction within the seamed slot as well as into the flow at the slot entrance as seen in Figure 26(d)-(e). Also it is observed that the scale growth is not uniform in the slot and it's more concentrated at the entrance. Figure 26(f) shows an opening at the top of the field of view when the slot is completely plugged. This area with opening is not taken into account to estimate the slot width, which would otherwise provide non-zero slot width. This result confirms that the plugging of the seamed slot due to scaling failure mode clearly occurs at the slot entrance. Also it suggest that the scale kinetics is influenced by the flow behavior at the entrance region. Few studies have reported that the plugging of the slot starts at the entrance due to transport of clay, fines and sand grains [1,9].

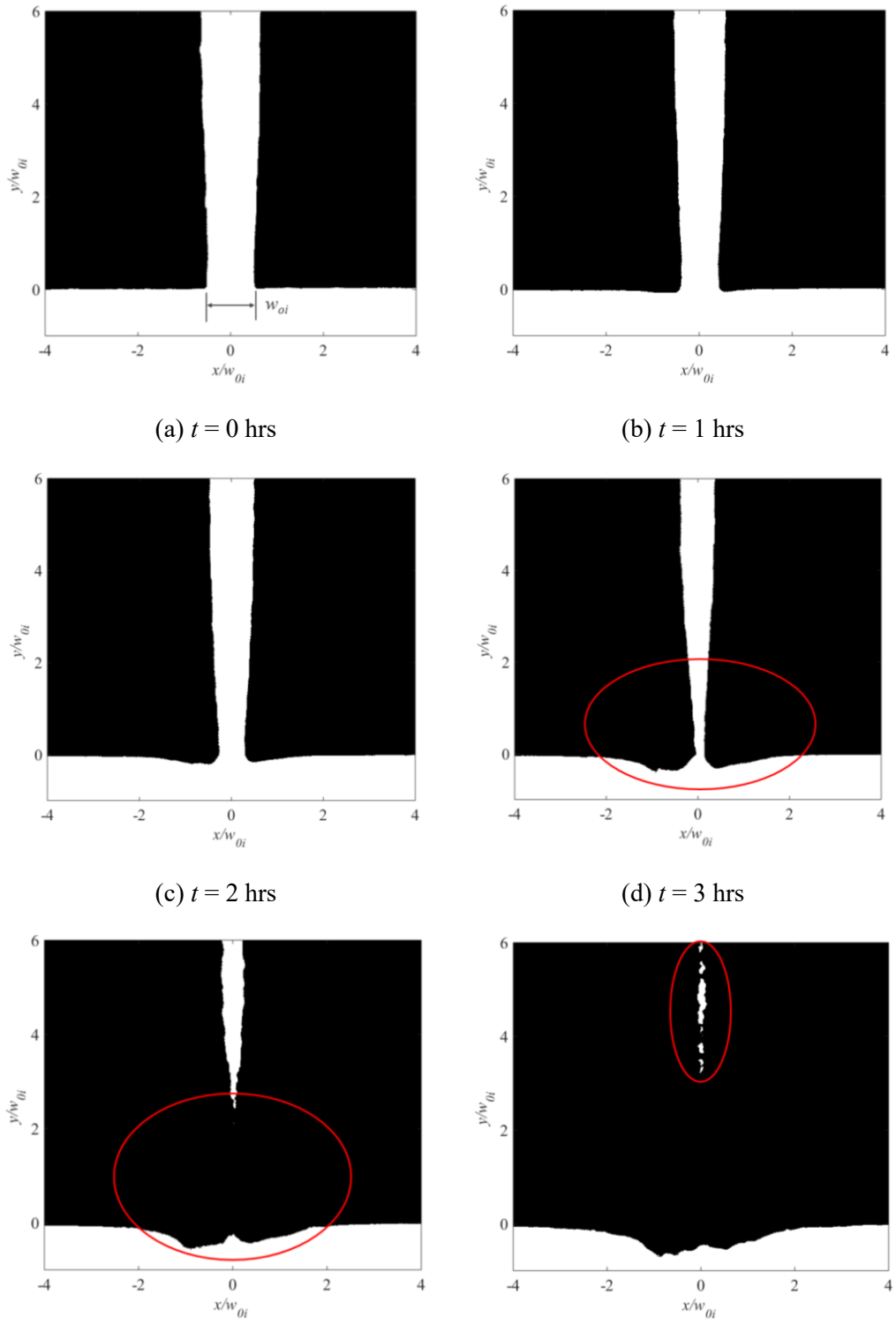

(a) t = 0 hrs

(b) t = 1 hrs

(c) t = 2 hrs

(d) t = 3 hrs

(e) t = 4 hrs

(f) t = 5 hrs

Figure 26: Calcium carbonate growth in the seamed slot, (a)-(f) at intervals in the experiment

Due to scale formation, the slot width reduces in real time and approaches to zero at ~4 hrs as shown in Figure 27(a). The scale growth is linear in nature

similar to the straight slot design. The estimated growth rate based on the reduction in width plot shown in Figure 27(a) is 0.1835 mm/hr. The pressure drop increases with time due to slot constriction and asymptotically reaches the maximum after the slot is plugged as shown in Figure 27(b). The differential pressure starts to rise significantly after ~3 hrs of time and reaches the maximum at scaling time of 4.91 hrs after it has plugged.

(a)

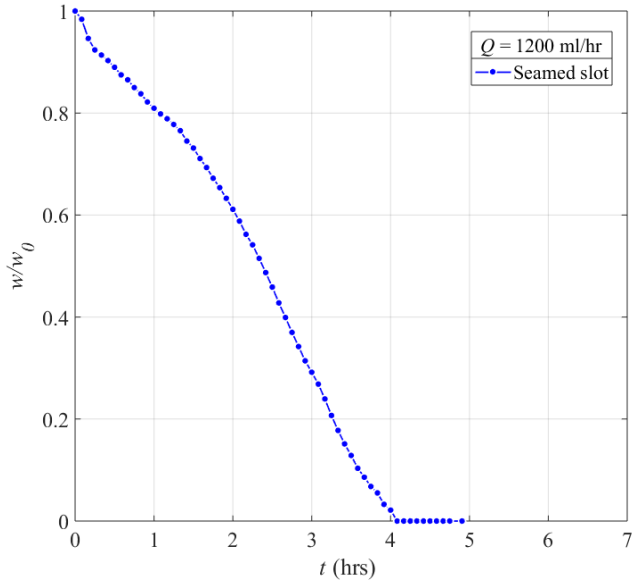

(b)

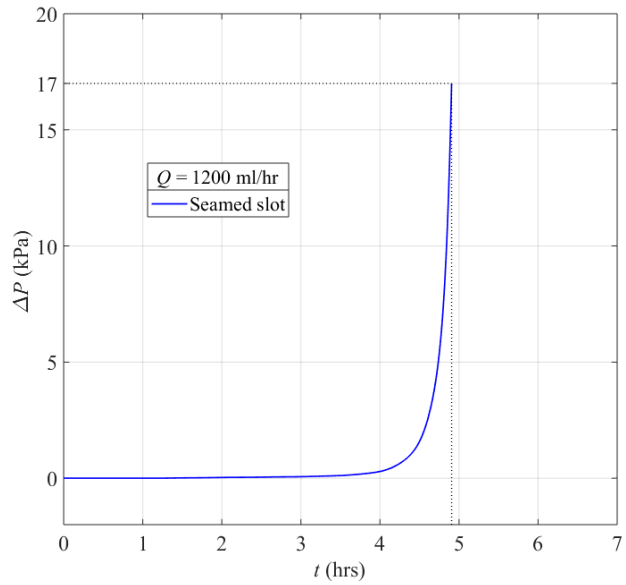

Figure 27: Seamed slot (a) Change in slot width, w_0 and w are the original and current slot width respectively and (b) Time history pressure trace

4.3 Results for the keystone slotted liner design

Similar to the seamed slotted liner design, the keystone slotted liner design also has narrow inlet having width of 1 mm as shown in Figure 28(a). However, its width at the outlet (not visible) is 8 mm as opposite to the seamed design. Figure 28 (a)-(g) shows the binary shadow images which provide scaling characteristics of the keystone slot. The binary images are obtained with the similar procedure of straight and seamed slot designs. Also for this configuration, the scale growth is prominent at the slot entrance similar to the seamed slot design. For the keystone slot design as well, the horizontal and vertical dimensions of the slot are normalized with the original width at the inlet (w_{0i}) due to the narrower inlet.

Over a period of time, the keystone slot is seen to fill with the calcium carbonate scale leading to the scaling failure. From Figure 28(e)-(g) and based on the earlier experience of straight and seamed slot, it is clear that the scale protrudes into the flow when the entrance region has sharp edged profile. Another major observation is that the keystone slot is plugged in a very short length shown in Figure 28(g), and is taken into account to calculate the slot width. Based on Figure 26(e) and Figure 28(g) for the seamed and keystone slots respectively, the keystone slot having wider outlet gets plugged in a short distance along the slot length as compared to the seamed slot. Therefore it suggests that wider the slot outlet, the slot gets plugged at the entrance in a short span along the slot length.

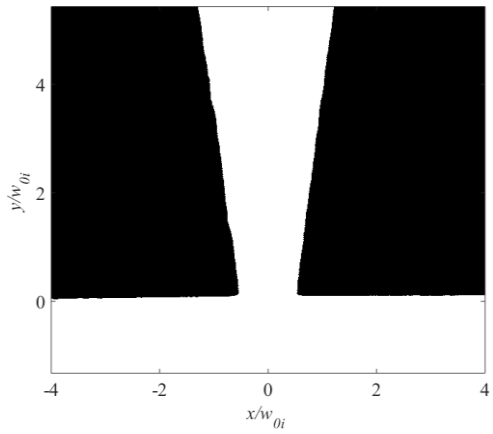

(a) t = 0 hrs

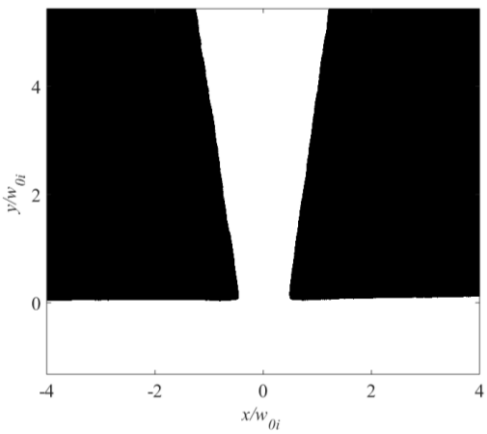

(b) t = 1 hrs

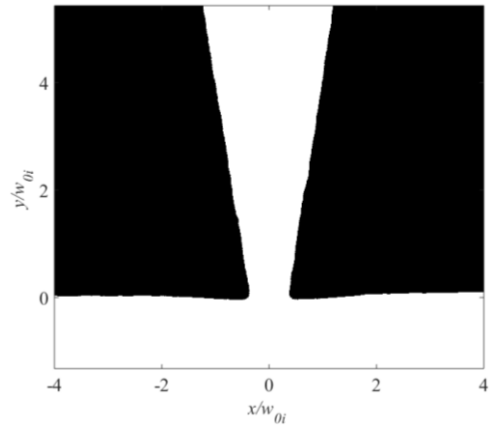

(c) t = 2 hrs

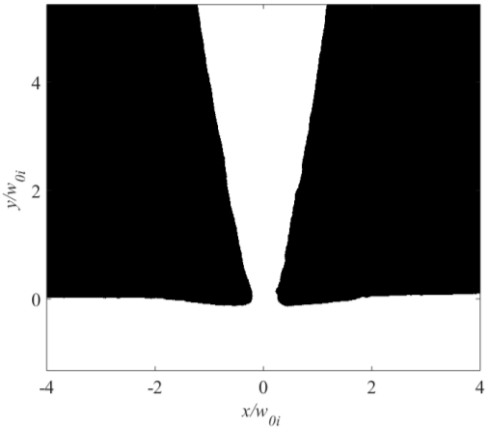

(d) t = 3 hrs

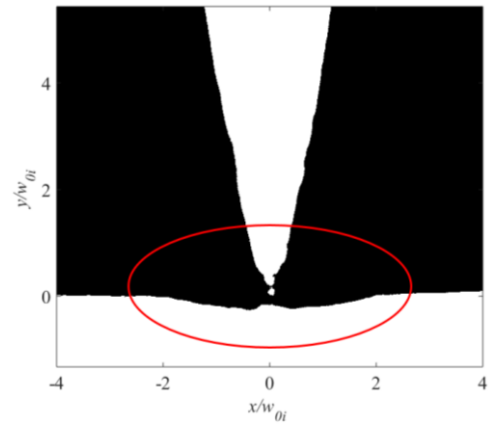

(e) t = 4 hrs

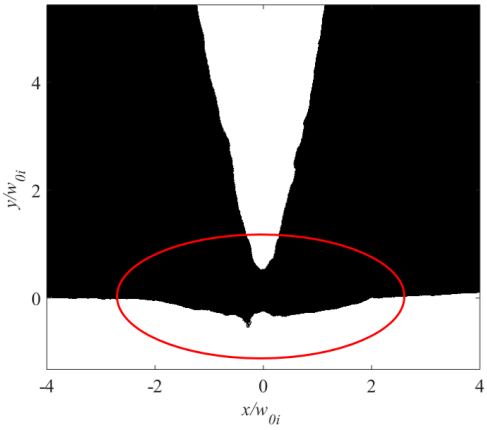

(f) t = 5 hrs

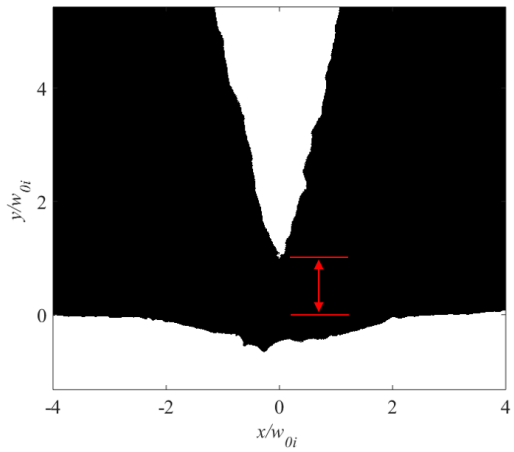

(g) t = 6.1 hrs

Figure 28: Calcium carbonate growth in the keystone slot, (a)-(g) at intervals in the experiment

The slot width reduction takes place due to calcium carbonate scale in the keystone slot. It approaches to zero at ~5 hrs as shown in Figure 29(a) and takes the longest time as compared to straight and seamed design. The reduction in slot width was linear in nature for the straight and seamed designs. However, Figure 29(a) only shows linear trend till ~3 hrs for the keystone design, after which it deviates from linearity. Therefore, a linear approximation is used to estimate the growth rate for the keystone design as shown in the plot as fitted model. The growth rate based on this linear regression is 0.1646 mm/hr. The differential pressure responds to reduction in slot width and increases with time as shown in Figure 29(b). However, it rises rapidly after ~4 hrs of time. The scaling time in case of keystone slot is 5.91 hrs corresponding to cut-off pressure of 17 kPa.

(a)

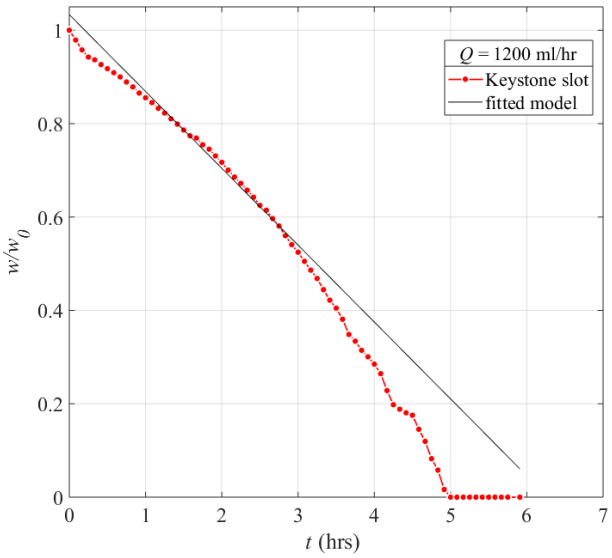

(b)

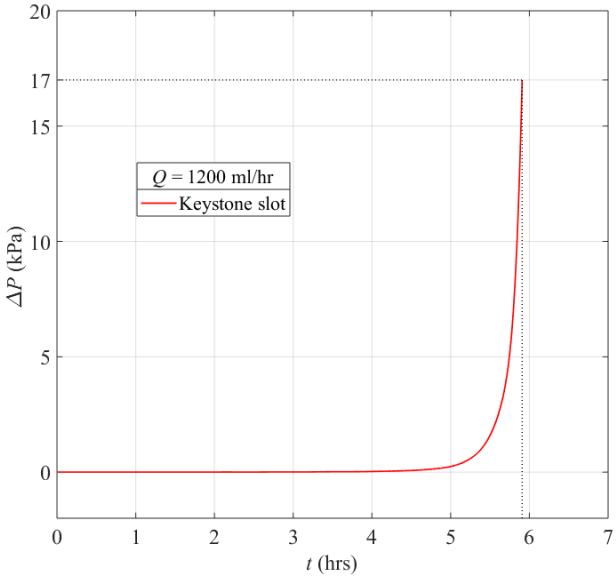

Figure 29: Keystone slot (a) Change in slot width, w_0 and w are the original and current slot width respectively and (b) Time history pressure trace

4.4 Comparison of slotted liner designs

The change in slot width and pressure drop measurements for the straight, seamed and keystone show a clear trend that the slot width reduces as the calcium carbonate grows within the slot. As a result the pressure drop across the slot increases. Therefore the growth rate and scaling time have inverse relationship. A comparison of these designs would provide better understanding to why the scaling

performance differs for all these designs. These designs have a common feature i.e. all slot profiles are supplemented with the sharp edged entrance or sudden contraction. However, the major difference among these designs is the available flow area. The seamed and keystone design have wider outlets as compared to straight slot design.

Figure 30(a) and (b) show the respective plots for the reduction in slot width and differential pressure with respect to time for the straight, seamed and keystone designs and for a flow rate of 1200 ml/hr. These two plots show all three datasets are distinct from each other and placed one after another. The closing of the slot width is shown in Figure 30(a) for all designs. The straight slot plugs faster when undergoes the scale formation phenomenon. On the contrary, keystone slot takes longer time to reach the zero and close the gap. The results for the reduction in slot width for the seamed slot fall in between the straight and keystone slot designs. Figure 30(b) shows the scaling time which is the time is taken to reach the differential pressure of 17 kPa. Since the calcium carbonate growth is expedited in case of straight slot, pressure drop curve reached the 17 kPa magnitude in short time of 4.5 hrs. The scaling time of 5.91 hrs is highest for the keystone design as the pressure drop rises slowly to reach the cut-off pressure. Similar to the reduction in slot width plot, the pressure drop variation in real time for the seamed slot is located in middle and has scaling time of 4.91 hrs.

(a)

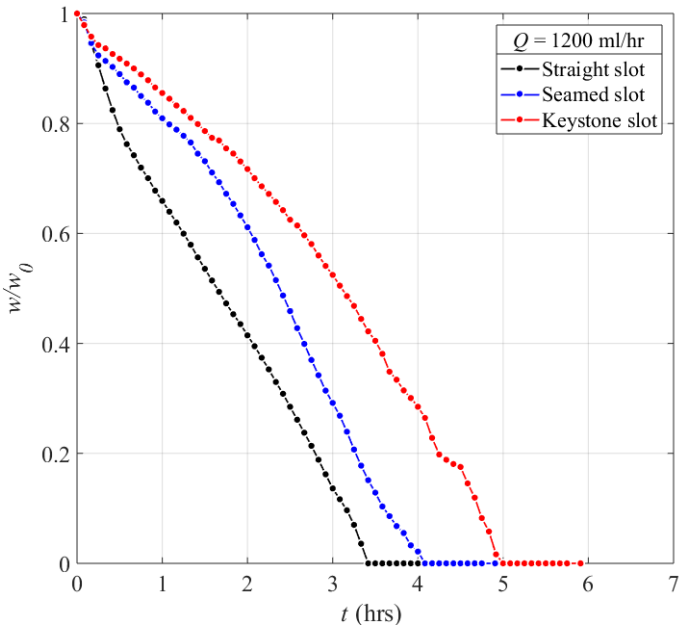

(b)

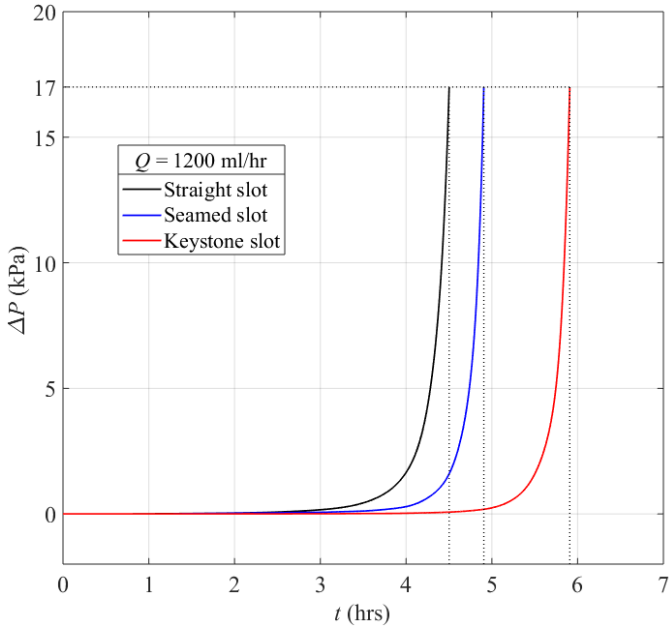

Figure 30: Comparison of (a) Change in slot width vs t, w_0 and w are the original and current slot width respectively and (b) Time history pressure trace

Figure 31(a) and (b) respectively show the effect of aspect ratio (AR) on the pressure drop and loss coefficient for the straight, seamed and keystone designs and flow rate of 1200 ml/hr. The aspect ratio is calculated by equation (15) which is the ratio of the depth with the current slot width, $w(t)$.The aspect ratio increases with decrease in the slot width. Figure 31(a) shows the general trend for the pressure

drop which increases with the increase in aspect ratio for all designs. The pressure drop is almost linear when the aspect ratio is lower than 50. The increase in pressure drop is rapid for the straight design as compared to the other two designs. The major reason is the faster growth of the calcium carbonate growth which results in lowest scaling time. On the contrary, the pressure drop for the seamed and keystone design is equivalent till aspect ratio of 50. However, after this value the pressure drop for keystone design drops in comparison to seamed design. This is possible considering the keystone design plugs slowest and has lowest growth rate among all these designs. It can be concluded that the straight slot design has higher pressure drop from scale formation as it has lower open flow area as compared to seamed and keystone designs.

Figure 31(b) shows the dependence of pressure loss coefficient on the aspect ratio with a logarithmic scale. The loss coefficient is calculated as per equation (14). In general the pressure loss coefficient decreases with increase in the aspect ratio (*AR*). As the slot width reduces, the aspect ratio increases which results in additional energy loss and greater flow resistance. Therefore the pressure loss coefficient has inverse relationship with the aspect ratio. The loss coefficient decreases as aspect ratio increases. It has decreased from ~1000 for *AR*~6.35 to ~1 for *AR*~250 indicating greater change in the flow resistance. All three slotted liners designs exhibit similar behavior and overlap with each other. It is possible that the straight, seamed and keystone designs have sharp edged entrances which does not induce any variation in the loss coefficient. Also higher open flow area in seamed and keystone design doesn't appear to affect the loss coefficient.

(a)

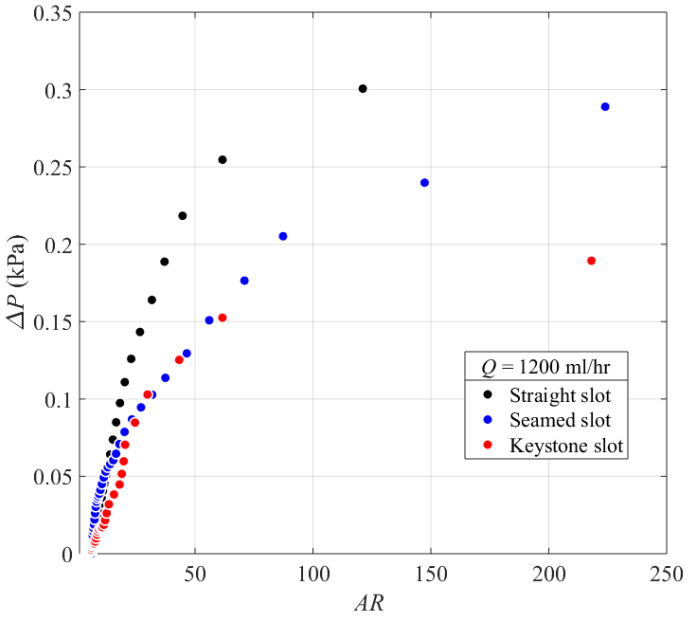

(b)

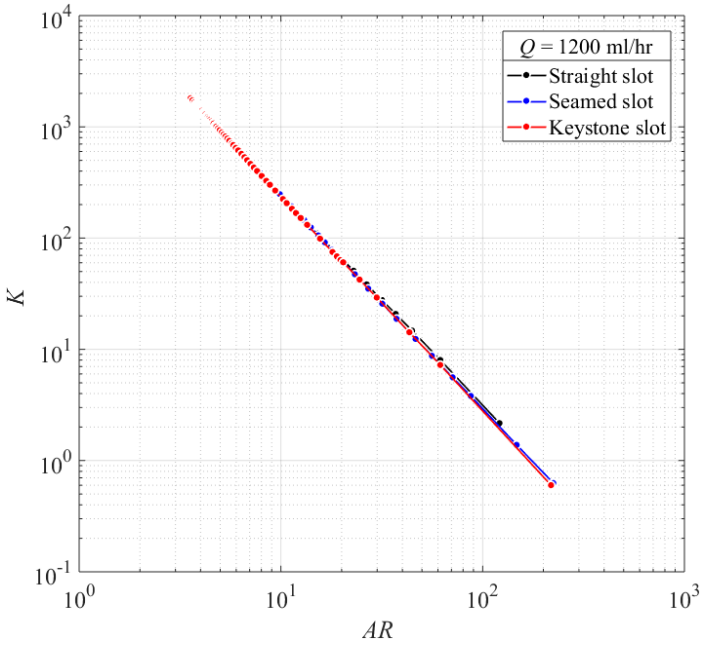

Figure 31: Effect of aspect ratio on (a) Pressure drop, and (b) pressure loss coefficient

Figure 32 summarizes the scaling performance of the straight, seamed and keystone designs. It shows that the straight slot has higher scale growth and hence lower scaling time, whereas the keystone design has lower scale growth and higher scaling time. The performance of seamed design lies in between the other two designs. Therefore from scaling perspective, the keystone design is a better design

to mitigate the scaling issues caused in SAGD production well since it has more open flow area available in comparison to the straight and seamed design.

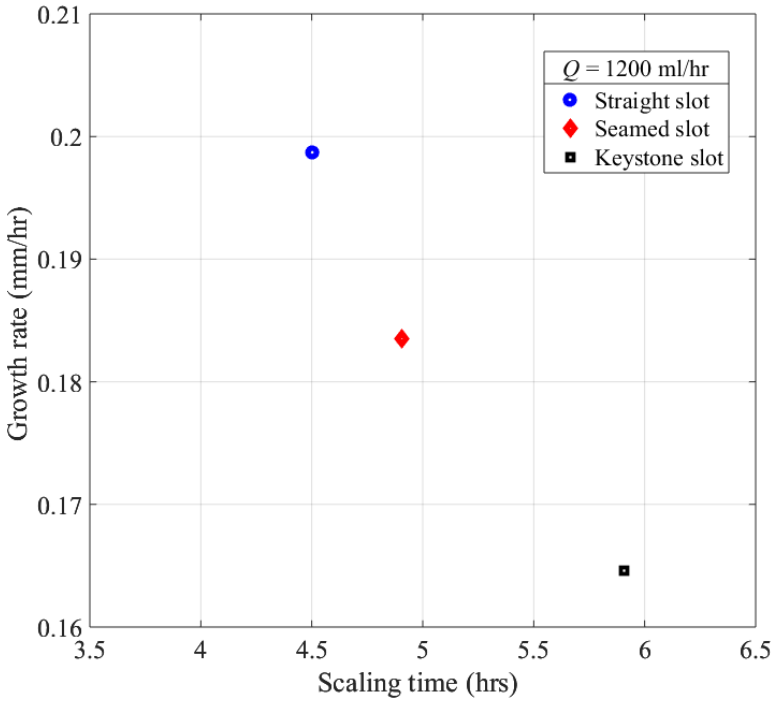

Figure 32: Growth rate vs Scaling time

4.5 Effect of scale growth on flow convergence and pressure drop

It has been studied so far that a pressure drop occurs due to the scale growth and resulting change in the slot. As the growth continues, the slot width reduces which increases the aspect ratio. In earlier sections, the effect of aspect ratio on pressure loss characteristics and flow resistance was investigated. It revealed that the pressure drop occurs as the aspect ratio increases, also the pressure loss coefficient decreases asymptotically indicating that the flow experiences significant resistance due to calcium carbonate growth. There are various studies which have investigated that the flow converges due to sudden contraction, and resulting streamline curvature is associated with the loss in pressure [63–66]. Therefore PIV is employed to obtain the two dimensional velocity and pressure field for the clean

slot i.e. no scaling and for a slot with scaling at the time of 2 hrs. This information will explain how a scale formation process affects the flow convergence phenomenon as well as associated pressure drop, and to hypothesize the critical role of pressured drop on scaling failure mechanism.

Figure 33 shows 2D-velocity and pressure fields obtained from the particle shadow velocimetry (PSV) experiments for a fluid passing through a narrow rectangular slot. As the flow approaches the slot, it cannot adjust itself and convergences due to the sudden constriction as shown in Figure 33(a). The streamlines possess a certain curvature in the vicinity of slot entrance. The velocity increases in the vertical direction and given streamlines straighten as the flow traverses through the slot. The velocity reaches the maximum value at $\sim y/w_{oi}=4$ it reaches ~4 times the non-dimensional parameter in *y*-direction. The corresponding pressure drop due to the sudden contraction is shown in Figure 33(b). The magnitude of pressure drop is increasing as it passes through the slot. It shows that the narrow slot is a low pressure region. The pressure drop reaches maximum at the same location as of high velocity in *y*-direction. However, its location is off-set from the middle of the slot.

Figure 33(c)-(d) show the 2D-velocity and pressure field for the calcium carbonate growth at time 2 hrs. This PSV experiment is conducted after stopping the scaling experiment at 2 hrs. Figure 33(c) shows that the scale growth further causes the streamline to converge significantly. Also, the available slot width has shrunk in comparison to the clean slot at the start of the experiment. The flow convergence and reduction in width leads to the increased velocity in the straight slot. The scale growth and subsequent increase in the aspect ratio enhances the flow

resistance. It reflects into the increased pressure drop located at the middle of the slot as shown in Figure 33(d) as compared to pressure drop at 0 hrs.

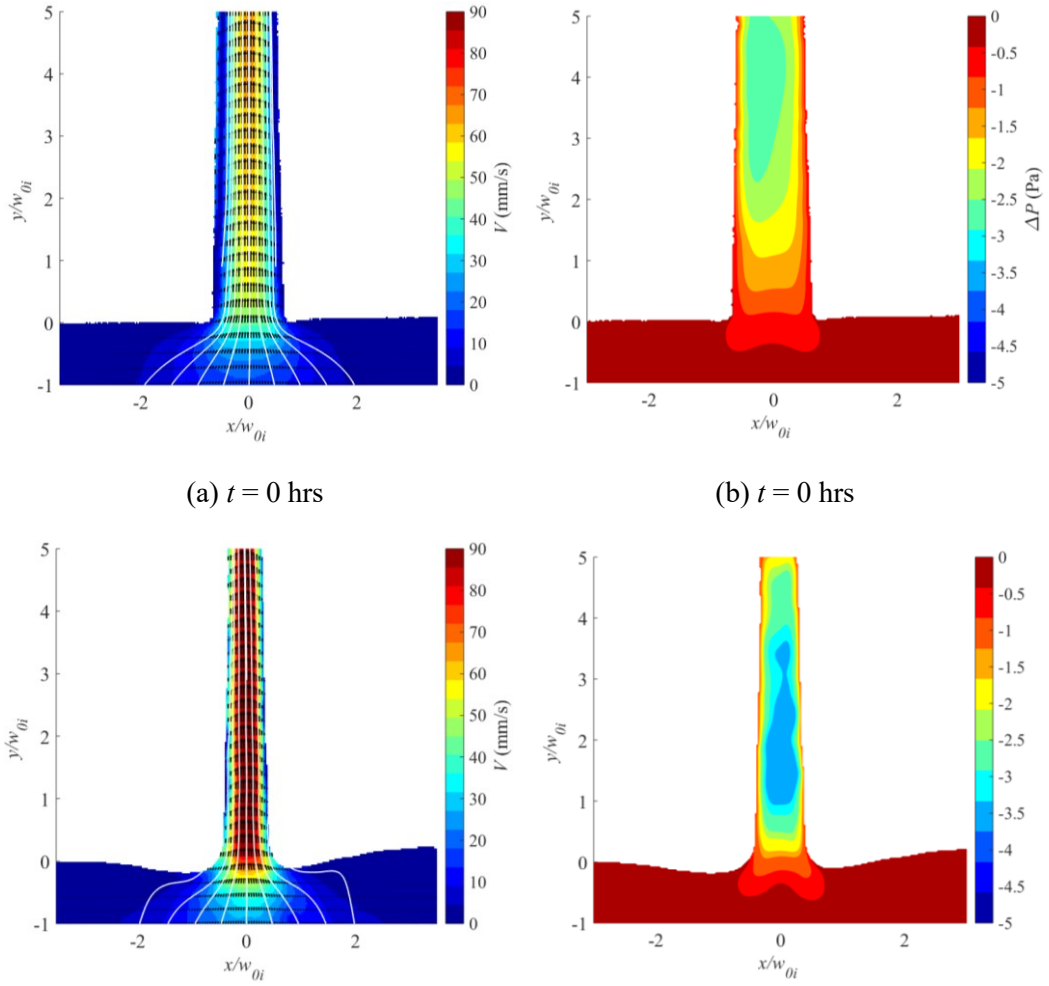

(a) t = 0 hrs (b) t = 0 hrs

(c) t = 2 hrs (d) t = 2 hrs

Figure 33: Results for straight slot at respective intervals in the experiment, (a) and (c) 2D-velocity field, (b) and (d) 2D-pressure field

Figure 34 shows 2D-velocity and pressure fields for a fluid passing through a seamed slot. The flow nearing the entrance region has amended itself to enter the slot which results into its convergence as shown in Figure 34(a). The seamed slot has narrow entrance as compared to its outlet. The 2D-velocity field shows higher velocity in the entrance region where the slot width is narrow. The velocity decreases further as the area increases in order to satisfy the continuity equation.

The pressure responds to this change in velocity and decreases at the slot entrance region where the velocity is high as shown in Figure 34(b). This is the location where highest pressure drop occurs. Also this is the region where maximum scale growth is concentrated as seen in Figure 26. The pressure increases along the downstream direction as the flow travels further.

Figure 34(c)-(d) show the 2D-velocity and pressure fields when the scale has developed at 2 hrs. The scale growth has altered the flow profile and it has converged considerably. In this case, the radius of curvature is larger as compared to the clean slot when the scale was absent as shown in Figure 34(c). The flow convergence and reduction in width affects the velocity field which increases significantly as compared to the clean slot. The pressure drop due to increased flow resistance and flow convergence is shown in Figure 34(d).

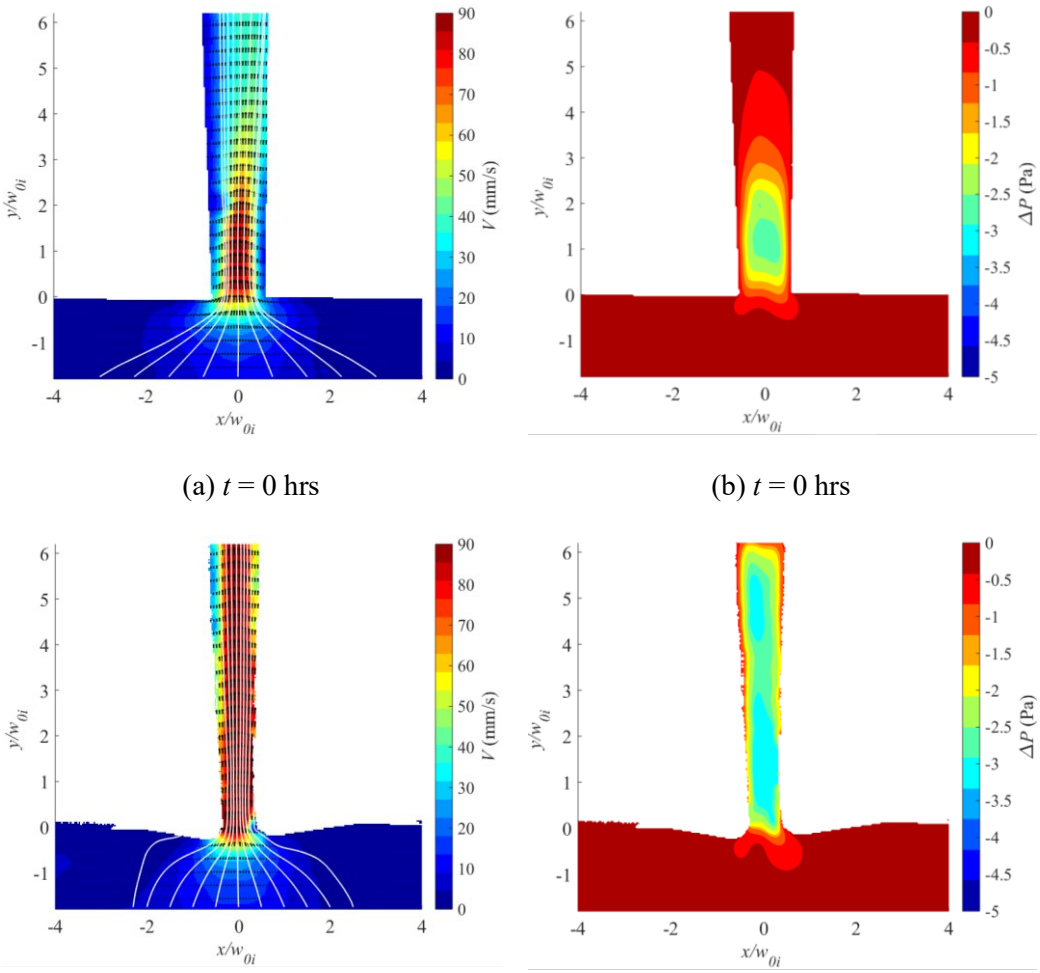

(a) t = 0 hrs (b) t = 0 hrs

(c) t = 2 hrs (d) t = 2 hrs

Figure 34: Results for seamed slot at respective intervals in the experiment, (a) and (c) 2D-velocity field, (b) and (d) 2D-pressure field

The observations made for the case of a seamed slotted liner design holds true for the keystone design as well. Both these design have narrow inlet of 1 mm. However, the keystone design has wider inlet of 8 mm in comparison to 1.5 mm in case of seamed design. Figure 35(a) and (c) show that the flow velocity has increased due to scale formation and corresponding reduction of slot width. The curvature of streamline is also higher as compared to the clean slot. The velocity is highest at the slot entrance where the width is narrow in case of a clean slot as well the slot with scaling. Afterwards the velocity decreases with the flow as the area decreases. Figure 35(b) and (d) show corresponding pressure field for the clean slot

and slot at 2 hrs. The maximum pressure drop occurs at the slot entrance. Also this is the location where predominant scale growth and plugging has occurred as seen in Figure 28.

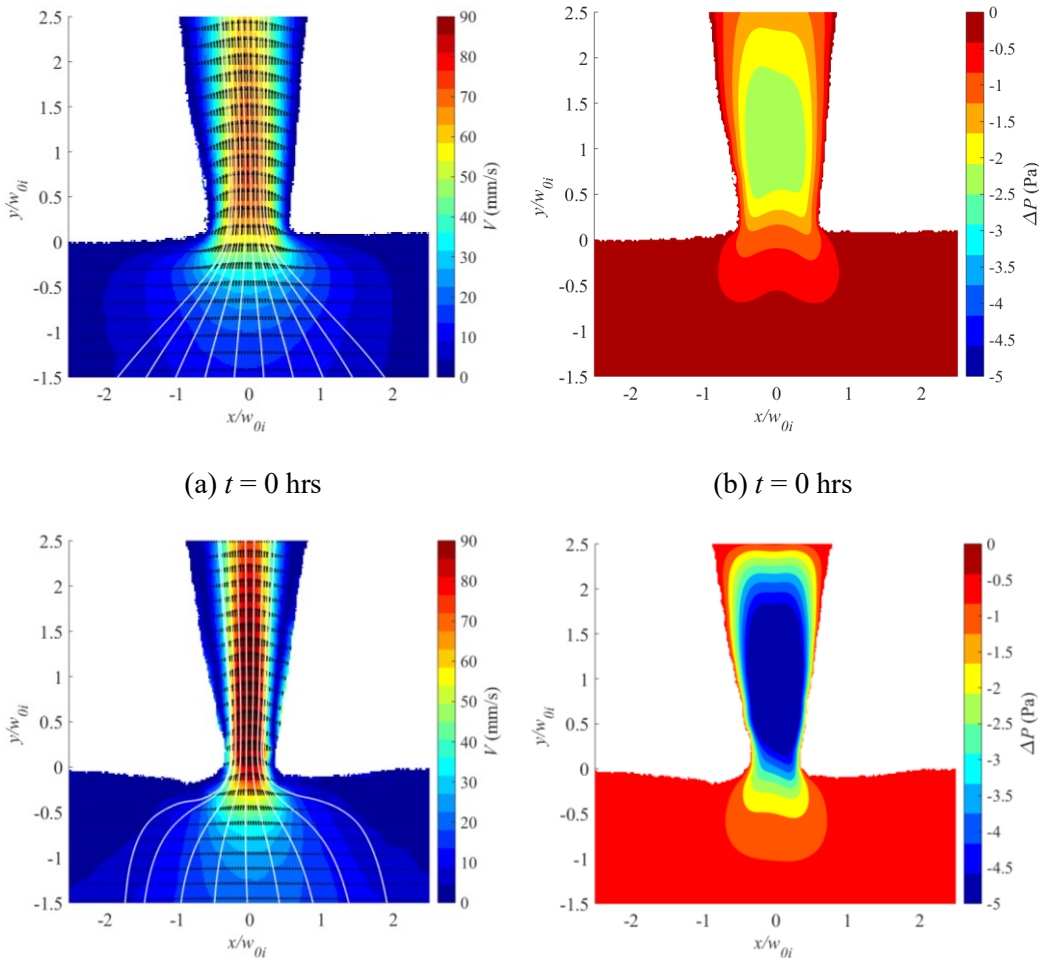

(a) t = 0 hrs (b) t = 0 hrs

(c) t = 2 hrs (d) t = 2 hrs

Figure 35: Results for keystone slot at respective intervals in the experiment, (a) and (c) 2D-velocity field, (b) and (d) 2D-pressure field

4.6 Conclusions

This study has provided insights to understand the scaling performances of the three common slotted liner designs. The slot width becomes narrower due to scale formation which increases the aspect ratio of the slot. It was observed that the scale growth is concentrated at the slot entrance. With the subsequent increase in the aspect ratio, the pressure drop and flow resistance increases. Based on the comparison, the slot width in keystone design closes gradually and also takes longer time to plug the slot as compared to the straight and seamed designs due to more open flow area. Therefore, the keystone design is a superior design to mitigate the scale formation in SAGD production wells. On the contrary, the pressure drop across the straight slot is comparatively higher to other two designs which makes it prone to the scaling failure. Also this study concluded that the plugging of the slot due to scaling phenomenon occurs at narrow locations having high velocity and low pressures. The calcium carbonate scale simultaneously grows within the slot as well as it protrudes into the flow near the slot entrance. This phenomenon significantly affects the pressure loss characteristics and flow resistance. It also leads to stronger flow convergence resulting in higher streamline curvature and accompanying reduction in pressure. Therefore, this study hypothesizes that the cycle of calcium carbonate growth and pressure drop continues until the plugging of the slot.

5 THE EFFECT OF INLET GEOMETRY PROFILE ON CALCIUM CARBONATE GROWTH RATE

The previous chapter presented the scaling performance of the three industrial designs. The straight slot was the most susceptible design to scaling, whereas the keystone design was better to mitigate the scale formation. The straight design experienced greater pressure losses as the scale growth continued. On the contrary, keystone design had lower pressure drop among all the designs. For sharp-edged designs the spike-like structure at the entrance due to the scale growth affected the flow resistance and convergence. The goal therefore of this study is to investigate the effect of inlet geometry profile on calcium carbonate scale formation by comparing the scaling performances of straight and rounded design. It will be assessed by controlling the entrance geometry with a rounded inlet and how it affects the flow resistance. The scaling experiments were conducted at different flow rates, Q =900 ml/hr, 1200 ml/hr and 1500 ml/hr. The straight slot that was assessed in section 4.1 and the straight slot design being assessed in the current chapter are two different designs. The straight slot geometry in the current chapter has a default surface roughness of 80 rms and default taper from the water jet cutting, and its width is consistent along the length of the channel. Whereas, the side wall surfaces of the straight slot in section 4.1 were polished with 80 grit sandpaper to remove the taper and its width is slightly broader at the inlet as compared to the rest of the channel. The width comparison of these geometries is shown in Appendix A6.

5.1 Analysis of the entrance length for straight slot

This section examines the 2D-velocity field for a Newtonian fluid passing through a straight slot using the particle shadow velocimetry (PSV) experiment. As the flow passes through the sudden contraction, the flow characteristics change until the flow is fully developed. The flow compromises with the losses in order to enter the narrow confined geometry. It is the hydrodynamic region which oversees the losses incurred by the fluid due its own inertia. Therefore, the properties such as viscous losses, pressure gradient are measured once the flow is developed. It is also clear that the inlet geometry profile alters the flow convergence behavior. Also, the literature review highlighted that the entrance length is not universal and depends upon the type of the geometry i.e. micro or mini-channel, range of the Reynold number and the aspect ratio of the channels. Therefore, it is essential to study the velocity field of the fluid passing through the straight slot and understand the hydrodynamic development length for the specific geometry and experimental conditions. Figure 36(a)-(c) show the averaged velocity vector map for a fluid traversing though the slot for the flow rates of 900 ml/hr, 1200 ml/hr and 1500 ml/hr. The width, hydraulic diameter and aspect ratio of the channel are 1 mm, 1.73 mm and 6.35 respectively. The respective Reynolds numbers from Table 2 for the three flow rates calculated by equation (9) are 68, 91 and 113. In each case, the inlet profile of the channel is sharp-edged. The first observation is that the flow velocity increases as soon as it enters the slot for all the flow rates. The velocity profile development is taking place with the maximum velocity at the center and lowering to zero velocity at the walls as represented by the length of the velocity vectors. The color contours of the magnitude of velocity (speed) are changing along

the channel length indicating the flow development. Based on the comparison of three contour plots, it can be said that the velocity in the slot is also increasing as the flow rate increases.

(a)

(b)

(c)

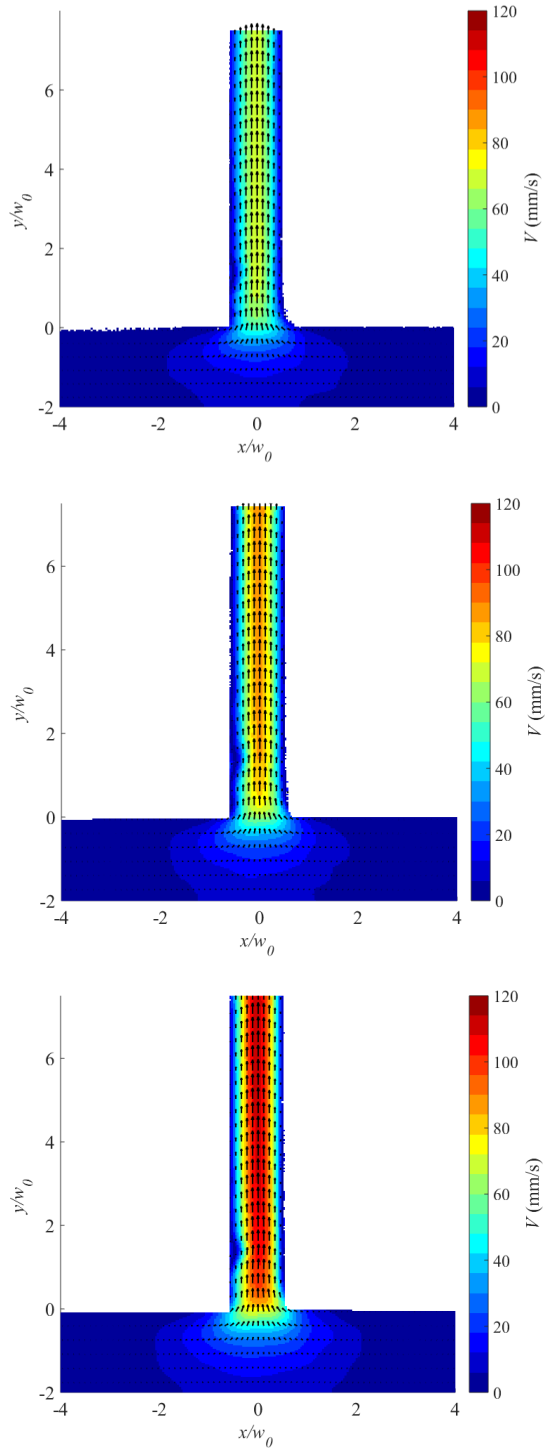

Figure 36: The 2D-velocity field for the straight slot for flow rate of (a) 900 ml/hr (b) 1200 ml/hr and (c) 1500 ml/hr

Figure 37(a)-(c) show the profiles of streamwise velocity for the straight slot geometry and respective flow rates of 900 ml/hr, 1200 ml/hr and 1500 ml/hr at different locations from the slot entrance. The horizontal (x) and vertical (y) dimensions are normalized with the in initial slot width (w_0). The velocity profiles are calculated at seven downstream locations from y/w_0=1 to 7, and are normalized with the local maximum velocity at that location. The velocity profiles are compared with theoretical laminar, parabolic velocity profile (V_{theory}) which is represented by:

$$V_{theory} = V_{Max}\left[1 - \left(\frac{2x}{w_0}\right)^2\right] \tag{36}$$

where, x is the horizontal dimension and V_{max}.is the maximum velocity.

The plots in Figure 37 show the developing behavior of the flow. A fully developed flow will have a parabolic profile with is maximum velocity at the center and zero velocity at the walls. As per equation (8), for lower Reynolds numbers, a shorter entrance length will be present. Figure 37(a) for 900 ml/hr shows that the velocity profile at y/w_0=4 is overlapping the theoretical parabolic profile, and beyond this there is little change in the profile at the downstream locations, so this is the location where flow might get developed. Figure 37(b) for 1200 ml/hr show that velocity profiles at y/w_0=6 and 7 are following the theoretical line. Figure 37(c) shows the velocity profiles for the flow rate of 1500 ml/hr. However, the first observation doesn't confirm any parabolic velocity profile for this flow rate and need additional information from centerline velocity development plot to confirm if the flow is fully developed.

(a)

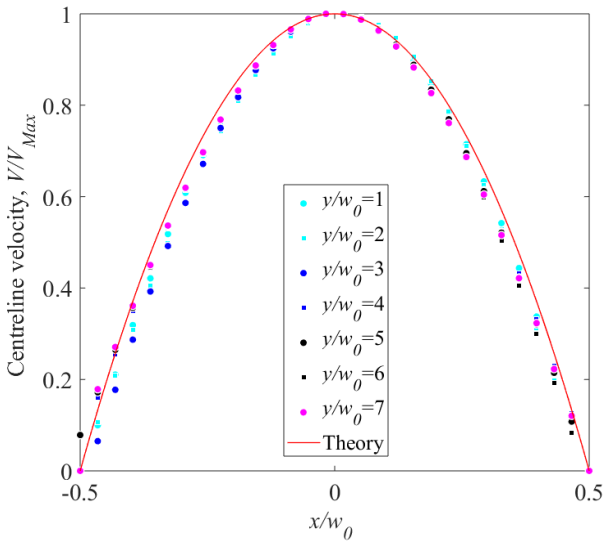

(b)

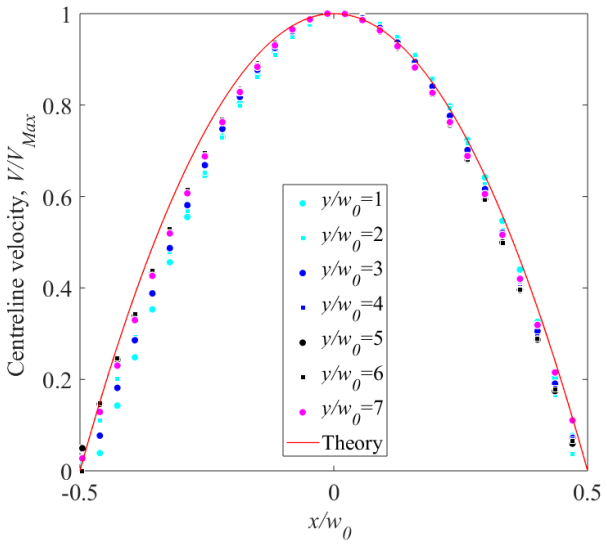

(c)

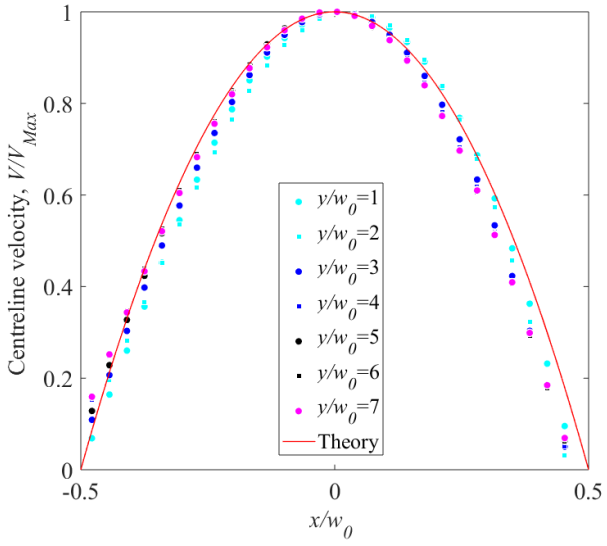

Figure 37: Velocity profiles in the straight slot for flow rate of (a) 900 ml/hr (b) 1200 ml/hr and (c) 1500 ml/hr

The streamwise centerline velocity development for the straight slot at different flow rates is shown in Figure 38. The vertical dimension (y) is normalized with the width (w_0), whereas the centerline velocity (V) is normalized with the theoretical average velocity ($V_{th,\,avg}=Q/A$) calculated considering the flow rate (Q) and slot width (w_0). The figure shows that once the fluid enters the slot it undergoes the development, and the centerline velocity reaches the 1.5 times the theoretical average velocity. Also, it increases rapidly within a short distance of y/w_0=-1 to 1. The basic criteria to determine if the flow is developed is to check if the centerline velocity has reached 99% of its fully developed value. However, in this study the field of view (FOV) is limited. Therefore, it is assumed that the flow is developed once the centerline velocity becomes constant.

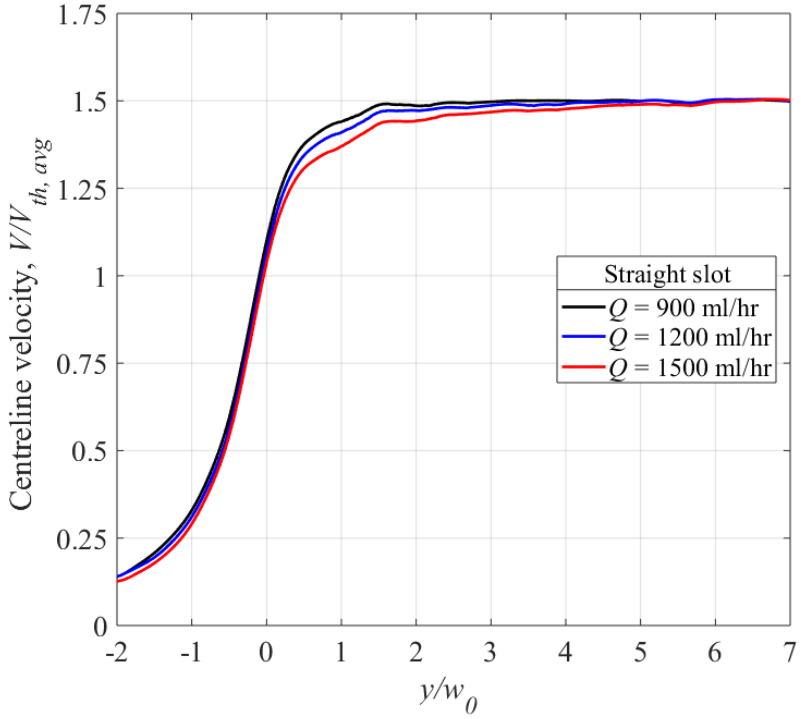

Figure 38: Centerline velocity development for the straight slot

Figure 38 shows that the flow stabilizes after traveling a certain distance for two flow conditions. For the case of Q = 900 ml/hr, the centerline velocity remains constant once it reaches the distance between y/w_0 = 3 and 4. However, considering the velocity profile at y/w_0 = 4 from Figure 37(c), it is appropriate to assume it is fully developed at this location. Similarly, the flow development for the flow rate of Q = 1200 ml/hr occurs when the fluid reaches the distance of y/w_0 = 6. However, the entrance length for the highest flow rate of Q = 1500 ml/hr cannot be determined as the centerline velocity is not constant before y/w_0 = 7 and hence lies outside of the FOV used in this this study.

The information obtained so far for centerline velocity development can be used to obtain a relation for the specific geometry and experimental conditions. The estimated entrance length for the flow rate of 900 ml/hr and 1200 ml/hr is 4 mm and 6 mm respectively. The respective Reynold number for these flow rates are 68 and 91, whereas the hydraulic diameter (D_h) and width is 1.73 mm and 1 mm respectively. Based on the literature review and entrance length correlations from Table 1 it is evident than when the Reynolds number is on the higher side or when the inertial forces come into the picture i.e. when $Re > 50$, the entrance length correlations are of a linear form. So with this consideration, a linear correlation is obtained by fitting the entrance length and Reynolds number for the flow rate of 900 ml/hr and 1200 ml/hr, which is further used to predict the entrance length for the 1500 ml/hr flow rate by linear scaling which comes out to be 7.12 mm. These values are now very different to the one shown in Table 2 obtained by the generic equation (8). The fitted correlation model is shown in Figure 39 and is given as:

$$\frac{L_e}{D_h} = 0.0364Re \tag{37}$$

Table 1 and Figure 39 show correlation models from the experimental studies. Muchnik et al. [80] obtained a linear correlation for $AR = 7$ as $L_e/D_h = 0.07Re$. However, this correlation was obtained for the hydraulic diameter of 1.3 to 1.8 cm, whereas the current study is done for $AR = 6.35$ and $D_h = 1.73$ mm. The wall effects come into the picture for smaller diameters and shorten the entrance length [74]. Therefore, the proposed entrance length approximation is reasonable.

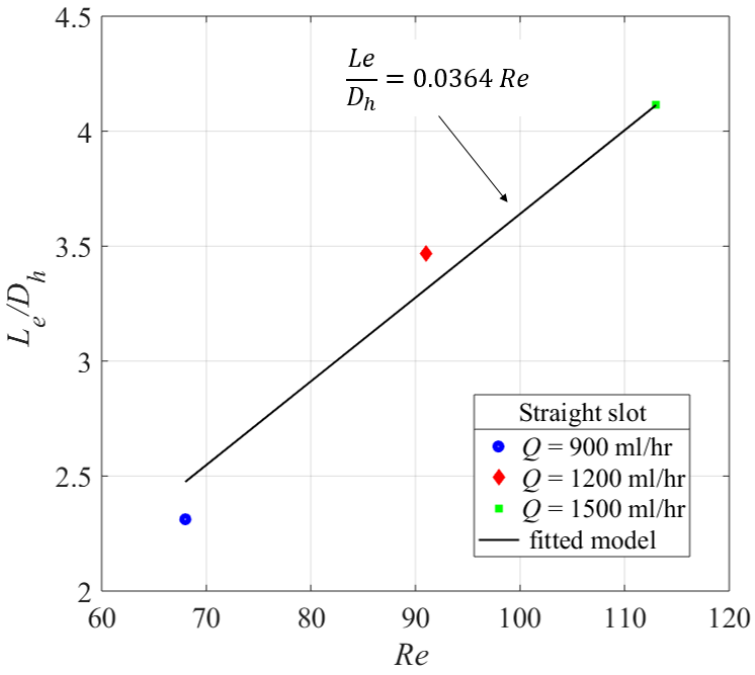

Figure 39: Entrance length correlation

5.2 Analysis of the entrance length for rounded slot

Similar analysis of the straight slot can be applied to the rounded slot using PSV. The key difference between these two designs is that straight design has sharp edges whereas the rounded design has the radius of 2 mm applied at the entrance, and provides relief from the constriction. The width, hydraulic diameter and aspect ratio are similar to the straight slot except the rounding of the edges.

Figure 40(a)-(c) show the 2D-velocity field for the passage of flow through the rounded slot at flow rates of Q = 900 ml/hr, 1200 ml/hr and 1500 ml/hr. This results in the velocity increase due to change in the cross-sectional area. The major observation is that the increase in velocity at all flow rates starts much further into the slot and not at the entrance as compared to straight slot design. This delayed development of the flow in streamwise direction can be attributed to the rounding of the edges. Another observation based on detailed comparison of Figure 40(a)-(c) by Figure 36(a)-(c) is that the flow velocity inside the slot (e.g. at $y/w_0 = 6$) for the rounded design is always higher than the straight design, and this remark holds true for all the flow rates considered in the experiment.

(a)

(b)

(c)

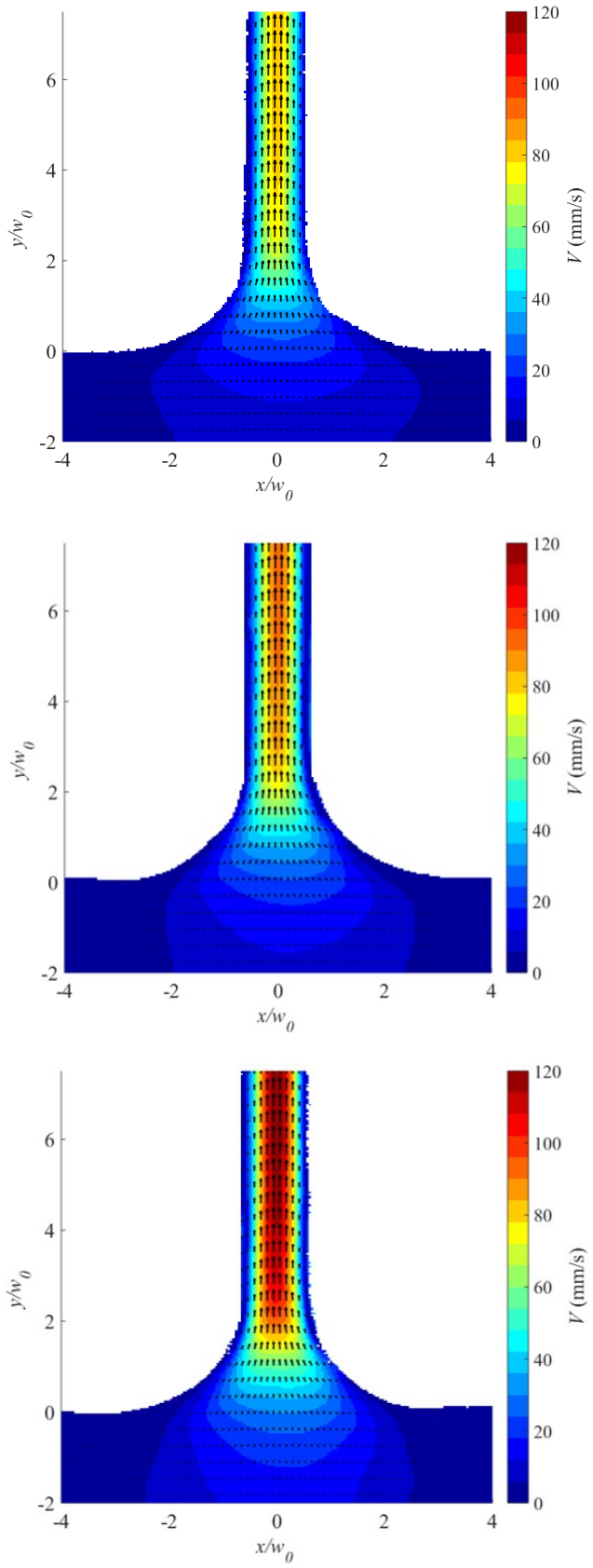

Figure 40: 2D-velocity field in the rounded slot for flow rate of (a) 900 ml/hr (b) 1200 ml/hr and (c) 1500 ml/hr

Figure 41(a)-(c) show the velocity profiles for the rounded slot geometry and at respective flow rates of 900 ml/hr, 1200 ml/hr and 1500 ml/hr. The horizontal (x) and vertical (y) dimensions are normalized with the slot width (w_0). The velocity profiles are compared with theoretical parabolic velocity profile and are calculated at seven downstream locations by normalizing it with maximum velocity. Since the instantaneous width at $y/w_0 = 1$ is greater than overall width (w_0), the velocity profile spans out in the lateral direction. The velocity is lower here in order to satisfy the continuity equation. At $y/w_0 = 2$, velocity profile of the flow doesn't resemble with the theoretical velocity profile. Figure 41(a) shows that the velocity profiles for $y/w_0 \geq 3$ are in good shape with the theory which does not appear to be for other flow rates because there is slight mismatch as seen in Figure 41(b) and (c).

(a)

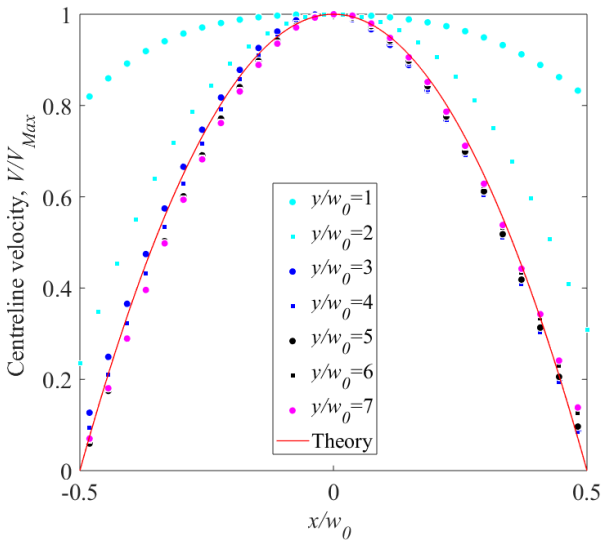

(b)

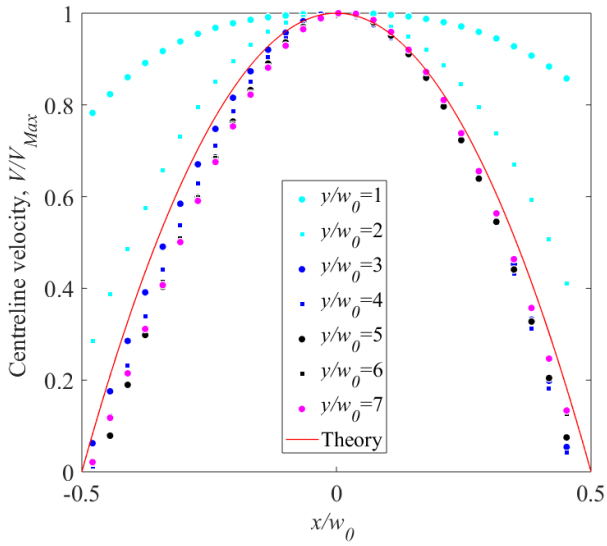

(c)

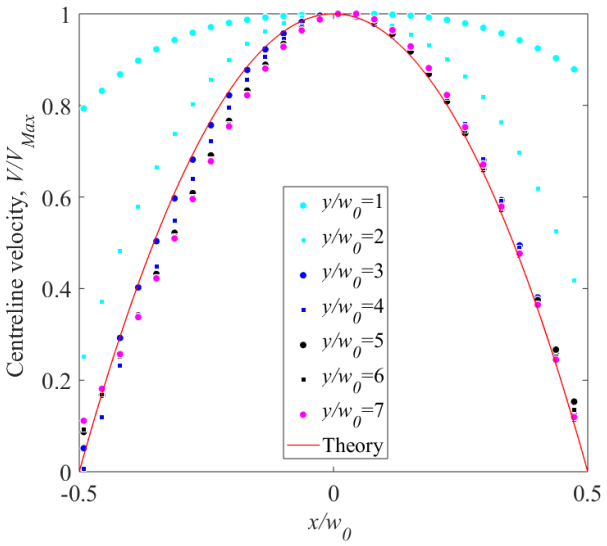

Figure 41: Velocity profiles in the rounded slot for flow rate of (a) 900 ml/hr (b) 1200 ml/hr and (c) 1500 ml/hr

Figure 42 shows the centerline velocity variation in the rounded slot for given flow rates. The vertical dimension (y) and centerline velocity (V) are normalized with the width (w_0) and theoretical average velocity ($V_{th,\ avg}$) respectively. The centerline velocity is low at the entrance due to more area and larger width. As the plot shows, the flow slowly develops as the velocity increases in streamwise direction. The normalized centerline velocity is still increasing till end of the field of view, hence it cannot be confirmed if the flow has developed. Therefore, the flow development occurs much further into the slot suggesting that the rounding of the edges has reduced the flow resistance. These findings are similar to the study performed by Lee et al [73] using micro-PIV to understand the flow resistances in the micro-channels with different radii's from 0.2 to 1.5 times the slot width. The study reported that with increase in the radius the flow resistance decreased with subsequent increase in the velocity at the downstream, and also the flow developed gradually.

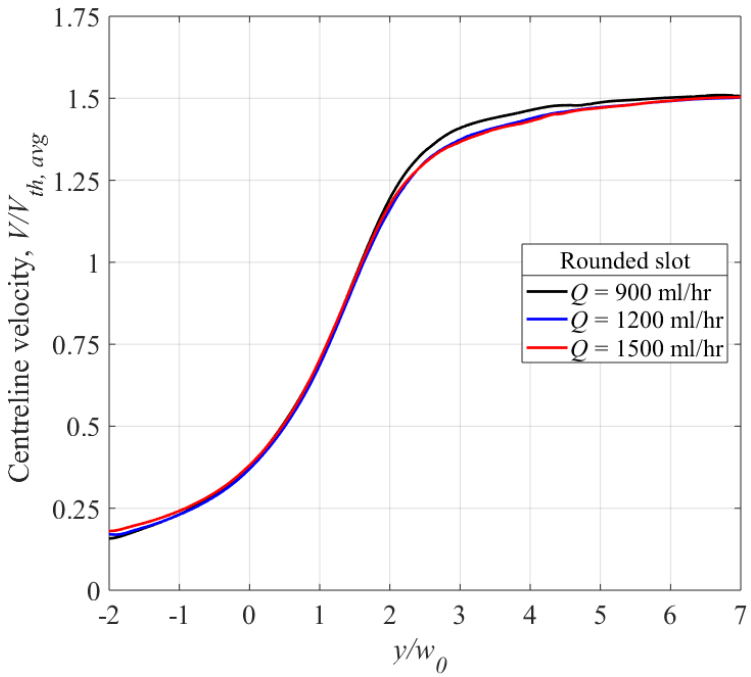

Figure 42: Centerline velocity development for the rounded slot

5.3 Effect of inlet slot profile and flow rate on calcium carbonate growth

Figure 43(a)-(f) shows the binary shadow images of the calcium carbonate growth for the straight and rounded designs, and for the flow rate of 1500 ml/hr. They are shown for every 0.5 hour till the slot gets plugged. The binary images are obtained by considering the intensity count threshold of 96 which is 37.65% corresponding to the intensity count of 255. Therefore, the areas below intensity count of 96 will appear as dark, and above which it will appear as white. The straight and rounded slots get blocked at ~2.5 hrs and ~3.2 hrs respectively. Both these designs have uniform width of 1 mm. The horizontal and vertical dimensions of the slot are normalized with the original width (w_0). In case of rounded design, the slot width (w_0) is obtained by averaging the local widths along the slot length except the area with rounded profile as annotated in Figure 43 (a) for the rounded slot. As the time progresses, the slot width reduces due to scale formation. The calcium carbonate scale grows within the slots in the lateral direction.

A detailed comparison of Figure 43 (a)-(g) shows that in case of straight design the calcium carbonate scale protrudes significantly into the flow near slot entrance, and simultaneously the slot is closing at the slot entrance. These two observations are uncommon for the rounded design. The scale growth in case of rounded design is uniform within the slot and plugs at a later time than straight slot. The binary images for the flow rates of 900 ml/hr and 1200 ml/hr are shown in Appendix A7 and A8 respectively.

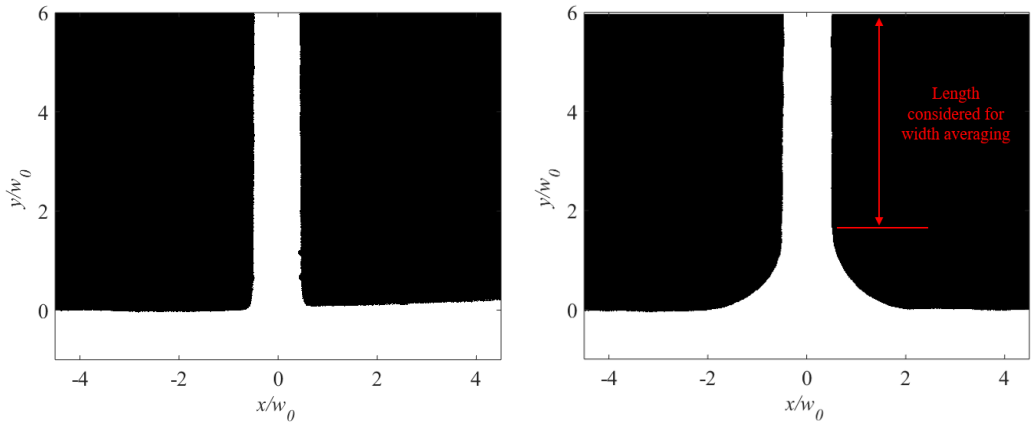

(a) t = 0 hrs

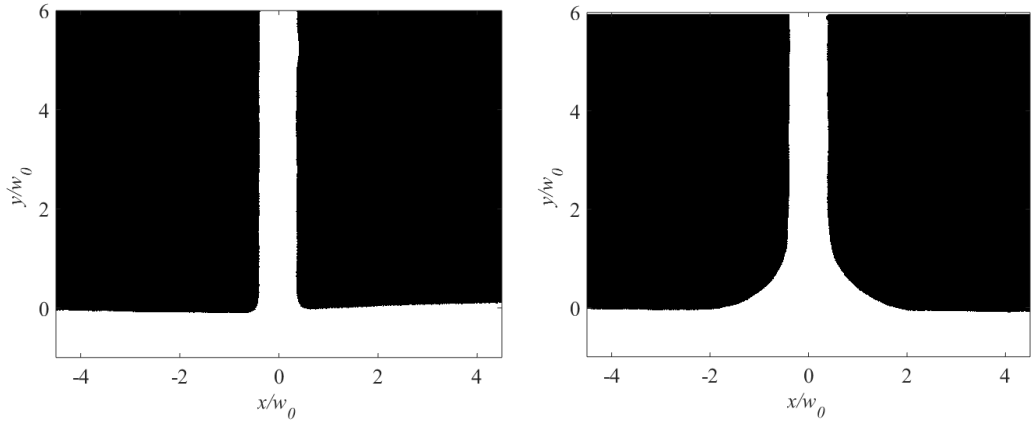

(b) t = 0.5 hrs

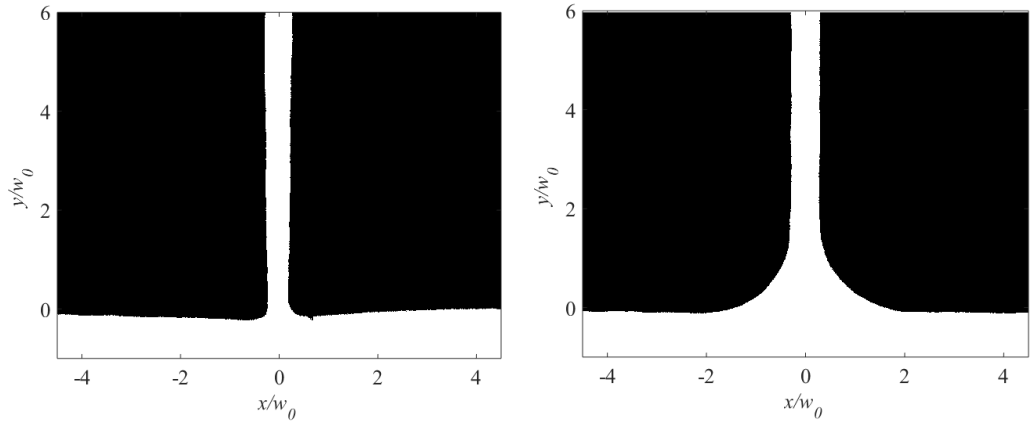

(c) t = 1 hrs

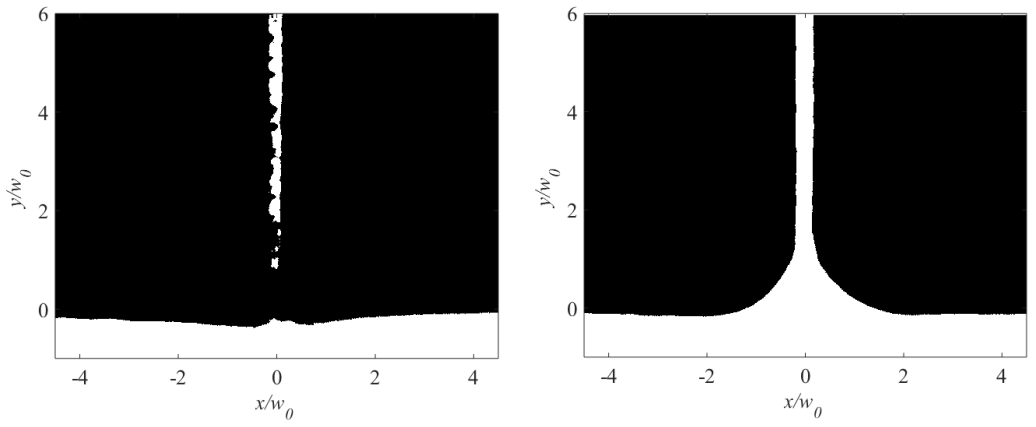

(d) t = 1.5 hrs

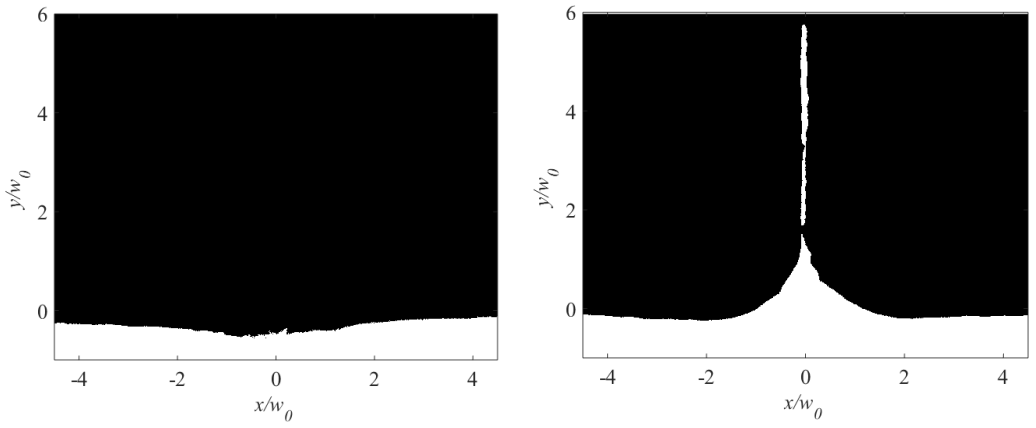

(e) t = 2 hrs

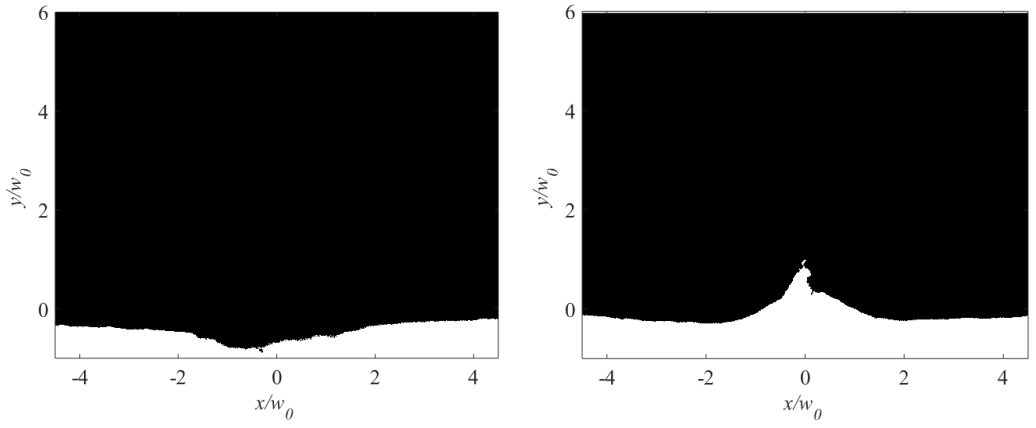

(f) t = 2.5 hrs

Figure 43: Calcium carbonate growth in the straight and rounded slot for Q = 1500ml/hr, (a)-(f) at intervals in the experiment

Figure 44 shows the change in slot width and pressure drop measurements for the straight and rounded designs. As seen before, the slot width reduces in real

time due to the scale growth which results in the increased pressure drop across the slot. A trend can be seen in Figure 44(a) that the slot closes first as the width approaches zero for the straight slot as compared to rounded slot for the flow rates of 1200 ml/hr and 1500 ml/hr. However, this observation does not apply to the flow rate of 900 ml/hr where the gap in both the designs closes at equivalent times. It can be observed that the reduction in slot width for these two designs is distinct till ~2 hrs after which they merge and reduces to zero together at ~3 hrs. The reason might be that these experiments were performed for the lowest flow rate of 900 ml/hr which continued till ~3 hrs. Therefore, this time is highest among all the flow cases. Also nucleation started occurring on the Teflon applied on the acrylic windows at a later time in the experiment.

Figure 44(b) represents the variation of differential pressure in real time for the designs which are being compared. In this comparison the trend is clearly visible for three flow rates considered i.e. the time taken by the pressure drop to reach the cut-off pressure of 17 kPa is always lower in case of straight slot than the rounded slot. It is due to fact that the rapid scale formation takes place which plugs the slot faster in comparison to the other design. Also, the scaling time for the case of rounded design is longest in all circumstances considered. Figure 44 also provides the information for the three flow rates considered in the experiment. It shows that with decrease in flow rate, the change in slot width takes a longer time to reach zero for the straight and rounded designs. Also the reduction in width is linear in nature and the growth of calcium carbonate can be obtained by linear regression. Also the scaling time i.e. the time taken by the differential pressure to reach the cut-off pressure of 17 kpa also increases with decrease in the flow rate.

Figure 45 shows the binary images for the straight and rounded slot at the time of 1.5 hrs for the three flow rates. It shows that the slot width shrunk as the flow rate increased for both the designs. Also all three flow rates show that the scale has grown at the entrance for the straight design whereas the gap in rounded design is more uniform.

(a)

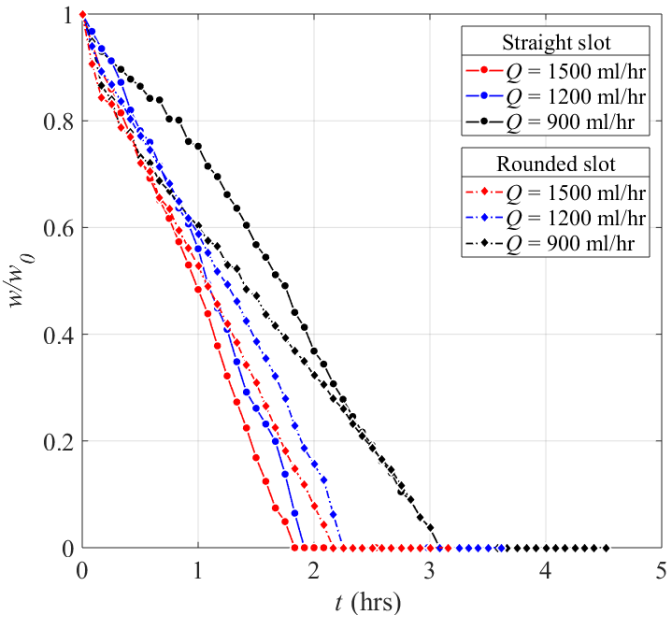

(b)

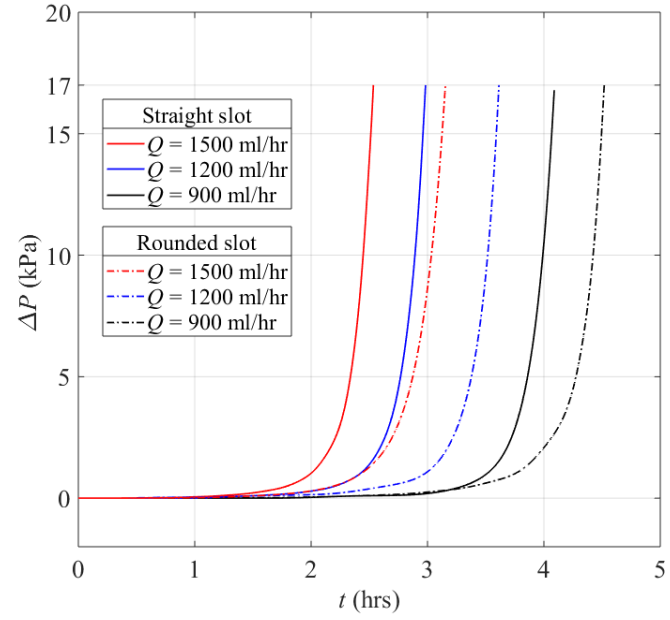

Figure 44: Straight and rounded slot (a) change in slot width, w_0 and w are the original and current slot width respectively and (b) time history pressure traces

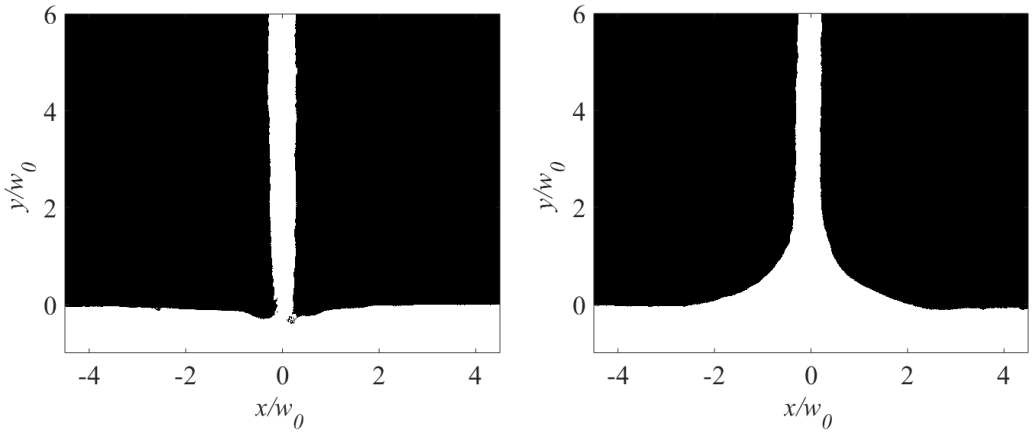

(a) Q = 900 ml/hr

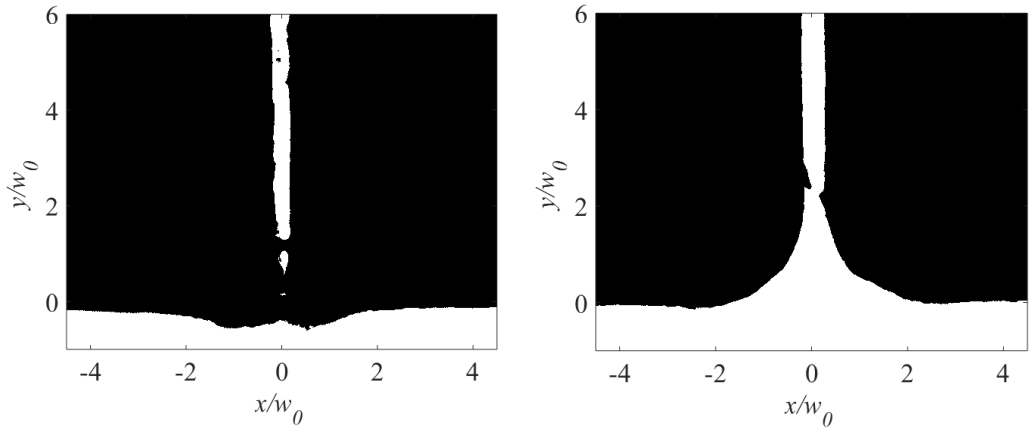

(b) Q = 1200 ml/hr

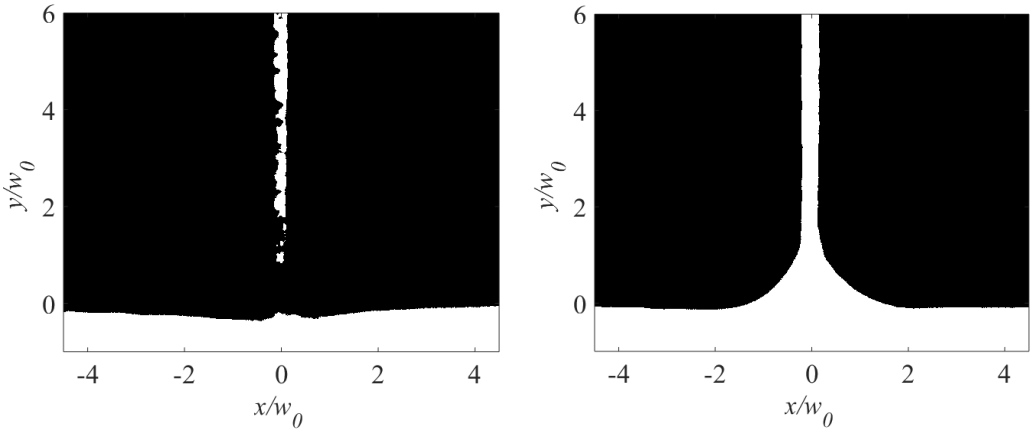

(c) Q = 1500 ml/hr

Figure 45: Calcium carbonate growth in the straight and rounded slot, (a)-(c) at t = 1.5 hrs, and respective flow rates

Figure 46 summarizes the effect of the input slot profile and flow rate on the calcium carbonate scale formation. It shows the growth rate for the case of the straight slot is higher as compared to rounded design for the flow rate of 1500 ml/hr and 1200 ml/hr, whereas it is equivalent for the flow rate of 900 ml/hr. Also the growth rate decreases as the flow rate decreases in case of both the designs. The scaling time for the rounded design is higher as compared to the straight design for all the flow rates. Also the scaling time increases as the flow rate decreases.

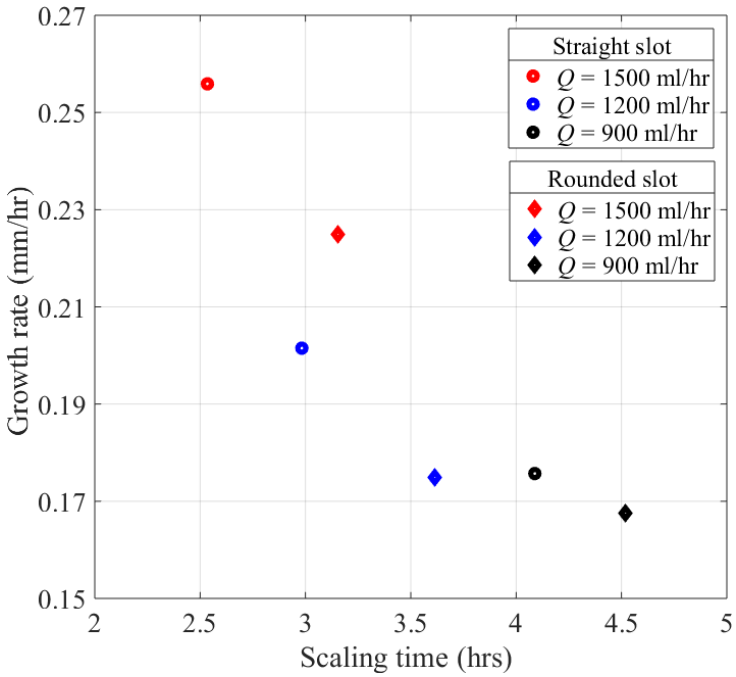

Figure 46: Growth rate vs scaling time for straight and round designs

5.4 Estimation of pressure drop and loss coefficient due to calcium carbonate scale formation

Figure 47 shows the dependence of pressure drop on aspect ratio (*AR*). As the scale growth continues in the slot, the width reduces. With the subsequent reduction in the width, the aspect ratio and velocity in the slot increases, and as a result the pressure drop across the slot increases. This observation is valid for both

the designs. The pressure drop is equivalent till $AR \leq 25$ for the two designs at all flow rates. However above this aspect ratio, the pressure drop is higher for a higher flow rate at any aspect ratio.

(a)

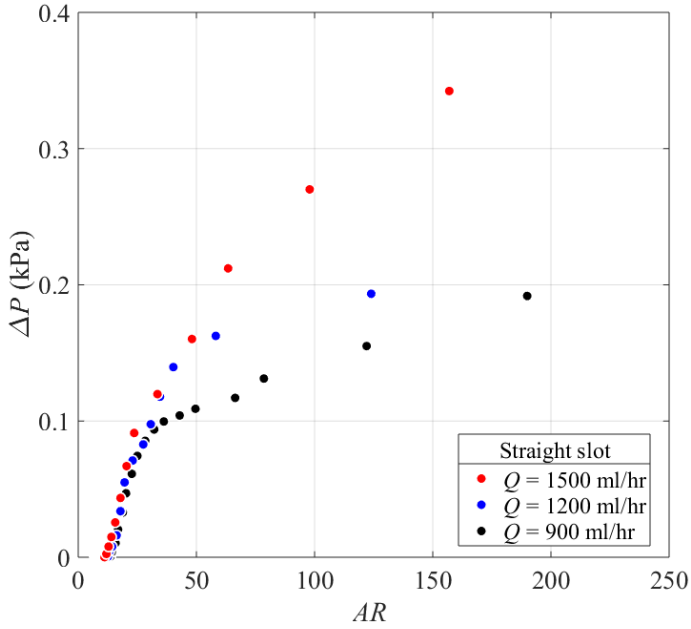

(b)

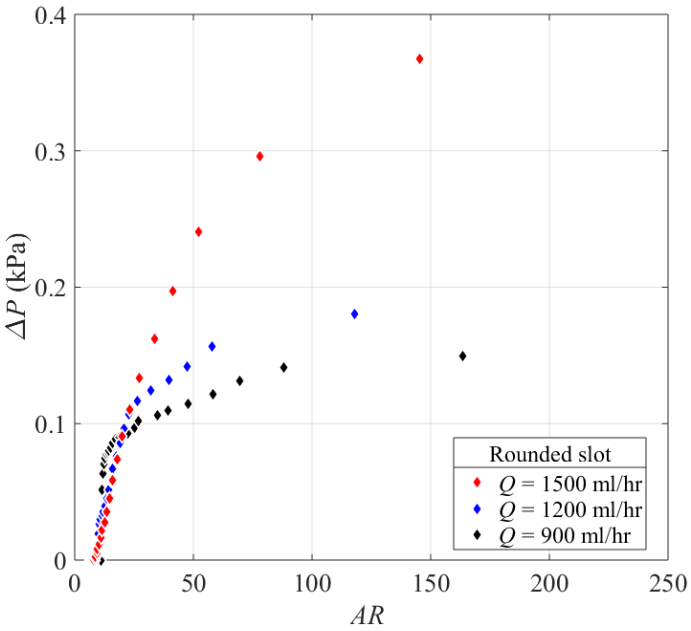

Figure 47: Pressure drop vs *AR* for (a) straight design and (b) rounded design

The relationship between the aspect ratio and pressure loss coefficient is shown in Figure 48 on a logarithmic scale. The loss coefficient is calculated by equation (14). It is the ratio of the pressure loss and the squared velocity. In general, the loss coefficient decreases with the increase in aspect ratio as shown in the plot. Although the pressure drop is increasing with increase in aspect ratio, the loss coefficient is decreasing due to dominant effect of increasing velocity due to the scale growth. When the flow rate is increased, the K vs AR curves are completely distinct with each other. This again shows the predominance of kinetic energy gain due to higher flow rate or lower slot width on the loss coefficient. Also the loss coefficient trends overlap and remain same for the straight and rounded designs indicating no effect of the input geometry profile.

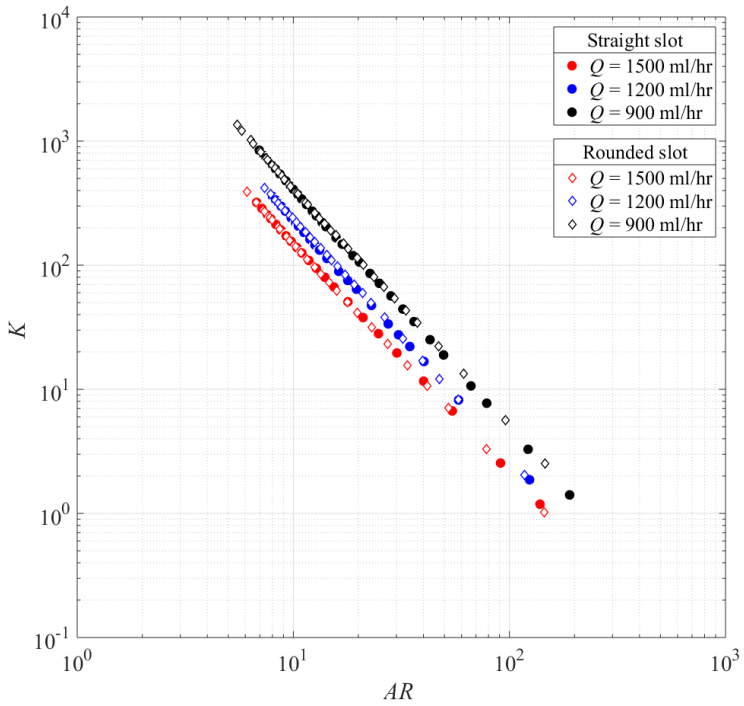

Figure 48: Pressure loss coefficient vs AR for straight and rounded slot

The dependence of the loss coefficient (K) on the Reynolds number (Re) is shown in Figure 49. In general, the loss coefficient decreases with increase in the

Reynolds number for a laminar flow. The plot shows that the Reynolds number increases with a decrease in slot width and corresponding increase in the velocity. It also increases for a constant aspect ratio geometry when the flow rate is increased. The loss coefficient decreases as the Reynolds number as well as the aspect ratio increases. This is mainly credited to the increase in velocity and flow resistance as the *AR* increases. Also, there is no significant difference in the loss coefficient due to dissimilar inlet geometry profile when the Reynold number changes. These findings are similar to the study performed by Yusuf et al [65,69] for a viscous flow through rectangular orifices with high aspect ratios. The study reported that with increase in the aspect ratio, the flow converged with subsequent change in the streamline curvature. The pressure drop also increased due to increase in the aspect ratio. The loss coefficient decreased for high Reynolds number values due to the effect of squared velocity.

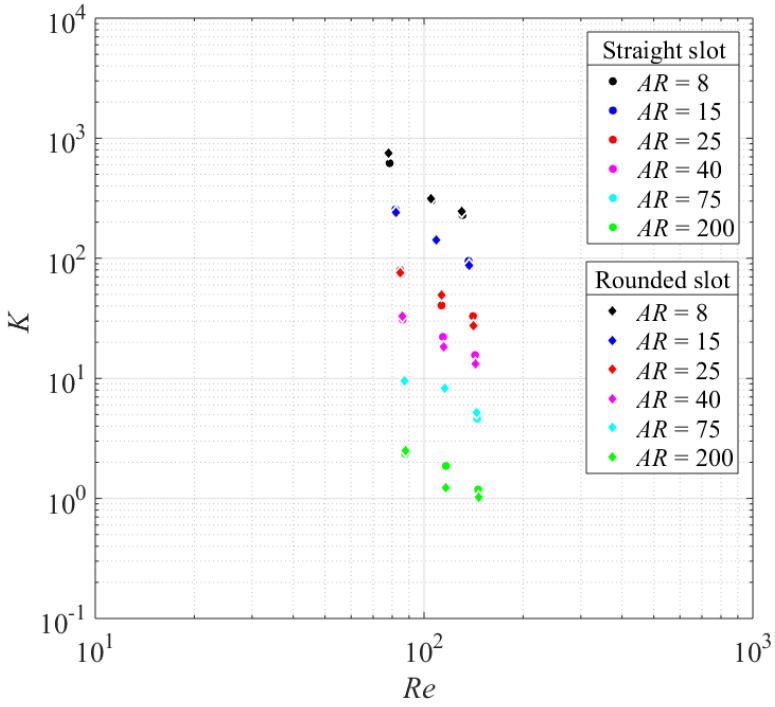

Figure 49: *K* vs *Re* for straight and rounded slot

5.5 Conclusion

This chapter investigated the effect of inlet geometry profile on calcium carbonate scale formation. The scaling experiments were conducted at different flow rates to assess the scaling performances of straight and rounded designs. The velocity field for a flow passing through the confined geometry was studied. The hydrodynamic development length was assessed for the specific geometries and experimental conditions. The velocity in the slot increases with the increase in flow rate. Due to gradual change in the area at the slot entrance, the flow developed slowly for the rounded slot design indicating a reduction in the flow resistance. Based on the velocity profiles and centerline velocity development, an entrance length approximation was proposed for the straight slot design. However, the approximation could not be offered for the rounded slot design as the flow was still developing within the available field of view.

A detailed comparison was made for the straight and rounded slot designs from the scaling perspective. It was observed that the calcium carbonate scale protrudes into the flow as a spike-like structure at the entrance of straight design. This phenomenon however was not observed in case of rounded design where the growth was uniform inside the slot. The experiments showed that the scale formation process accelerated with the increase in flow rate. Also, the growth rate was comparatively higher for the straight slot than rounded slot design. The time taken to reach the cut-off pressure is higher in the case of the rounded design. This confirms that the gradual change at the entrance by rounding the sharp edges affects the scaling tendency.

The pressure loss characteristics for the straight and rounded design were investigated. With subsequent increase in the aspect ratio due to scale formation, the flow converges and accelerates. This mechanism leads to a gain in the kinetic energy and increased pressure losses which affects the pressure loss coefficient. With subsequent increase in the Reynolds number associated with the increased aspect ratio and flow rate, the pressure loss coefficient decreases due to dominant effect of velocity in comparison to pressure losses. This trend remains the same for the dissimilar rounded inlet profile even when the flow has developed slowly with lower accompanying resistance in comparison to the straight slot design.

6 CONCLUSIONS AND FUTURE WORK

The current study investigated the effect of near-well fluid mechanics on the scaling failure mode associated with the SAGD production well. The literature was reviewed to report the deleterious effects of calcium carbonate scale growth on the industrial equipments. The parameters affecting the scale formation as well as the techniques currently in practice for the assessment of scale formation and growth rate were thoroughly reviewed. The literature revealed that the scale formation process has been mainly studied to understand the effect of thermodynamic parameters and there are very few studies which have tried to understand the effect of flow related aspects Also image acquisition system had rarely been used in dynamic flow and in-situ conditions to monitor the calcium carbonate scale growth and investigate the pressure loss characteristics in narrow confined geometry. Therefore, a flow rig was developed to simultaneously measure the scaling parameters using optical and differential pressure measurement techniques for the SAGD in-situ application.

The scaling performances of industrial slotted liner designs i.e. straight, seamed and keystone were investigated to asses a better design in mitigating the scaling issues. The particle shadowgraph velocimetry (PSV) and scaling experiments were conducted at the flow rate of 1200 ml/hr. The experiments provided live visuals to show how the scale grows in real time and locate the critical locations which are affected by the fluid flow behavior. This study also validated the effect of flow convergence and pressure drop due to sudden geometry

contraction on the calcium carbonate build-up and growth. It was observed that the slot width reduces due to calcium carbonate scale formation and subsequent crystal growth. It was confirmed that the scale growth is concentrated at the slot entrance which was a low pressure region. Based on the comparison, the keystone design is a superior design to mitigate the scale formation in SAGD production wells. On the contrary, the straight slot is prone to the scaling failure. The study concluded that the plugging of the slot due to scaling phenomenon occurred at high velocity and low pressure regions. It was observed that a pressure drop occurs as the fluid flow encounters the sudden contraction and the scale formation process is initiated in the slot. With the subsequent scale growth and increase in the aspect ratio, the pressure drop and flow resistance improved. The study concluded that the flow convergence phenomenon is accompanied by the increase in streamline curvature, fluid velocity and associated pressure drop. As the scale growth continues, the flow further converges with increased velocity and subsequent pressure reduction, which in turn influences the scale kinetics. Therefore, this study hypothesizes that the cycle of calcium carbonate growth and pressure drop continues until the plugging of the slot.

The second study investigated the effect of inlet geometry profile on calcium carbonate scale formation. The basis behind this study was that for sharp-edged designs, the spike-like scale structure at the slot entrance affected the flow convergence. The PSV and scaling experiments were conducted for the straight and rounded designs at flow rates 900 ml/hr, 1200 ml/hr and 1500 ml/hr. The velocity field for a flow passing through the confined geometry was studied which showed that the velocity in the slot increases with the increase in flow rate. It was concluded that flow developed slowly for the rounded slot design indicating the reduction in

the flow resistance due to gradual change in the area at the slot entrance. Based on the velocity profiles and centerline velocity development, an entrance length approximation was proposed for the straight slot design.

A detailed comparison was made for the straight and rounded slot designs from the scaling perspective. The growth rate was comparatively higher for the straight slot than rounded slot design. The time taken to reach the cut-off pressure is higher in the case of the rounded design. Therefore this study confirmed that the gradual change at the entrance by rounding the sharp edges affects the scaling tendency. Also the scale formation process accelerated with the increase in flow rate. The pressure loss characteristics for the straight and rounded design were investigated. The scale formation and growth mechanism affected the pressure loss coefficient due to subsequent gain in the kinetic energy and increased flow resistance. With subsequent increase in the Reynolds number, the pressure loss coefficient decreased for a given laminar flow. The trend remained the same for the straight and rounded inlet profiles even when the flow developed slowly with lower accompanying resistance in case of rounded inlet profiles. Also, this study confirms that the shear stress doesn't have detrimental effect on the scale build-up as the scale growth increased in real time for three different flow scenarios.

Future work

This study has provided significant insight into understanding the scaling mechanisms for different configurations of slotted liner design. It also emphasized the significance of the near-well fluid mechanics on the cyclic effect of local pressure field and calcium carbonate growth. Therefore, the conclusions of this study are believed to have made significant contributions in understanding the

crucial role of hydrodynamic parameters and constriction on the slotted liner designs from scaling perspective. This study mainly developed a test rig to validate scaling phenomenon for different flow related aspects and hydrodynamic parameters. However, this methodology can be extended to gain the comprehensive knowledge of the flow physics on underlying scaling mechanisms using the following:

- It was earlier reported that the solution supersaturation and surface properties are critical factors that affect the crystallization process. The current study was conducted for only one saturation ratio using a metal flow cell with a certain roughness. Therefore, the experiments can be conducted at different saturation ratios, materials and surface roughness in order to retrieve plausible additional information from the experiments.

- It was concluded that the local pressure is affected by the flow convergence and spike-like structure associated with the scale growth at time of 2 hrs. Also, the velocity measurements for the rounded design concluded that the flow developed slowly and hence corresponding flow resistance has decreased. However, the scaling experiment showed that the loss coefficient was equivalent for the straight and rounded design. It might be due to limited range of Reynold numbers considered or pressure transducer connected at upstream and downstream locations (not at the slot entrance and exit) was not able to detect the local pressure changes. Also the pressure loss characteristics have been rarely investigated for the rounded design in a laminar flow regime. Therefore, there is an opportunity to investigate the pressure drop and loss coefficients for a wide range of Reynolds numbers

for the rounded design (without scaling) using multiple pressure transducers or numerical techniques.

- The current study considered camera exposure time of 800 μs for the scaling experiment. However, the intensity count decreased with subsequent scale formation. So the experiments can be conducted in future with dynamic exposure time setting in order to retrieve plausible additional information from the experiments.

REFERENCES

[1] U.G. Romanova, T. Ma, An investigation of the plugging mechanisms in a slotted liner from the steam assisted gravity operations, SPE - Eur. Form. Damage Conf. Proceedings, EFDC. 1 (2013) 285–292. https://doi.org/10.2118/165111-ms.

[2] O.S.D. Centre, Facts about Alberta ' s oil sands and its industry, Gov. Alberta, Oil Sands Discov. Cent. (2016) 51.

[3] J. Mclennan, C. V Deutsch, SAGD Reservoir Characterization Using Geostatistics: Application to the Athabasca Oil Sands, Alberta, Canada, Cent. Comput. Geostatistics. (2004) 1–21.

[4] S. Banerjee, T. Abdelfattah, H. Nguyen, Benefits of passive inflow control devices in a SAGD completion, Soc. Pet. Eng. - SPE Heavy Oil Conf. Canada 2013. 2 (2013) 1195–1203. https://doi.org/10.2118/165478-ms.

[5] B. Fermaniuk, Sand Control in Steam Assisted Gravity Drainage (SAGD) Wellbores and Process of Slotted Liner Design and Manufacture, University of Calgary, 2013.

[6] T. Cheung, M. Scheck, S.C. Limited, Novel Scale Remediation for Steam Assisted Gravity Drainage (SAGD) Operations, (2013) 1–10.

[7] V. Lightbown, New SAGD Technologies Show Promise in Reducing Environmental Impact of Oil Sand Production, J. Environ. Solut. Oil, Gas, Min. (2015). https://doi.org/10.3992/1573-2377-374x-1.1.47.

[8] U.G. Romanova, G. Gillespie, J. Sladic, T. Ma, T.A. Solvoll, J.S. Andrews, A Comparative Study of Wire Wrapped Screens vs . Slotted Liners for Steam Assisted Gravity Drainage Operations, World Heavy Oil Congr. (2014) 1–23.

[9] D.B. Bennion, S. Gupta, S. Gittins, D. Hollies, Protocols for slotted liner design for optimum SAGD operation, J. Can. Pet. Technol. 48 (2009) 21–26. https://doi.org/10.2118/130441-PA.

[10] RGL Reservoir Management Inc. AB, Canada, (2015). http://www.rglrm.com.

[11] J. Xie, S.W. Jones, C.M. Matthews, B.T. Wagg, P. Parker, R. Ducharme, Slotted liner design for SAGD wells, World Oil. (2007).

[12] M. Sivagnanam, J. Wang, I.D. Gates, On the fluid mechanics of slotted liners in horizontal wells, Chem. Eng. Sci. 164 (2017) 23–33. https://doi.org/10.1016/j.ces.2017.01.070.

[13] D. Matanovic, C. Marin, M. Bojan, Sand Control in Well Construction and Operation, Springer Science and Business Media, 2012.

[14] T.M.V. Kaiser, S. Wilson, L.A. Venning, Inflow analysis and optimization of slotted liners, SPE Drill. Complet. (2002). https://doi.org/10.2118/80145-PA.

[15] J.C. Cowan, D.J. Weintritt, Water-formed scale deposits, Gulf Publishers Company, 1976.

[16] S. Muryanto, A.P. Bayuseno, H. Ma'mun, M. Usamah, Jotho, Calcium Carbonate Scale Formation in Pipes: Effect of Flow Rates, Temperature, and

Malic Acid as Additives on the Mass and Morphology of the Scale, Procedia Chem. 9 (2014) 69–76. https://doi.org/10.1016/j.proche.2014.05.009.

[17] S. Muryanto, A.P. Bayuseno, W. Sediono, W. Mangestiyono, Sutrisno, Development of a versatile laboratory project for scale formation and control, Educ. Chem. Eng. 7 (2012) e78–e84. https://doi.org/10.1016/j.ece.2012.04.002.

[18] B.P. Erno, J. Chriest, K.A. Miller, Carbonate scale formation in thermally stimulated heavy-oil wells near Lloydminster, Saskatchewan, (1991) 229–240. https://doi.org/10.2523/21548-ms.

[19] O. Bello, Calcium Carbonate Scale Deposition Kinetics on Stainless Steel Surfaces Omoregbe Bello Doctor of Philosophy The University of Leeds, PhD Thesis, Univ. Leeds. (2017).

[20] C.J. Hinrichsen, Preventing scale deposition in oil production facilities: An industry review, NACE - Int. Corros. Conf. Ser. 1998-March (1998).

[21] Y. Duccini, A. Dufour, W.M. Hann, T.W. Sanders, B. Weinstein, High performance oilfield scale inhibitors, NACE - Int. Corros. Conf. Ser. 1997-March (1997) 1–27.

[22] G.M. Graham, L.S. Boak, C.M. Hobden, Examination of the effect of generically different scale inhibitor species (PPCA and DETPMP) on the adherence and growth of barium sulphate scale on metal surfaces, Soc. Pet. Eng. - Int. Symp. Oilf. Scale 2001. (2001). https://doi.org/10.2523/68298-ms.

[23] P. Duggirala, Formation of calcium carbonate scale and control strategies in

continuous digesters, CD Del II Coloq. Int. Sobre Celul. …. (2005).

[24] T. Chen, In-Situ Monitoring The Inhibiting Effect Of DETPMP On Caco3 Scale Formation By Synchrotronx-Ray Diffraction, Corros. 2007 NACE Int. (2007) 1–14.

[25] J.E. Oddo, M.B. Tomson, A Discussion of calcium carbonate scaling problems and solutions with respect to produced brines, Soc. Pet. Eng. AIME, SPE. PI (1989) 551–564. https://doi.org/10.2523/19763-ms.

[26] O. Söhnel, J.W. Mullin, A method for the determination of precipitation induction periods, J. Cryst. Growth. (1978). https://doi.org/10.1016/0022-0248(78)90002-7.

[27] T. Chen, A. Neville, M. Yuan, Calcium carbonate scale formation - Assessing the initial stages of precipitation and deposition, J. Pet. Sci. Eng. 46 (2005) 185–194. https://doi.org/10.1016/j.petrol.2004.12.004.

[28] J. Moghadasi, M. Jamialahmadi, H. Müller-Steinhagen, A. Sharif, Scale Formation in Oil Reservoir and Production Equipment during Water Injection (Kinetics of CaSO4 and CaCO3 Crystal Growth and Effect on Formation Damage), (2007). https://doi.org/10.2523/82233-ms.

[29] N. Andritsos, A.J. Karabelas, Calcium carbonate scaling in a plate heat exchanger in the presence of particles, Int. J. Heat Mass Transf. 46 (2003) 4613–4627. https://doi.org/10.1016/S0017-9310(03)00308-9.

[30] E. Ruckenstein, G.O. Berim, G. Narsimhan, A novel approach to the theory of homogeneous and heterogeneous nucleation, Adv. Colloid Interface Sci. 215 (2015) 13–27. https://doi.org/10.1016/j.cis.2014.10.011.

[31] K. Sawada, G. Kanno, M. Iino, K. Satoh, The Phenomena of Calcium Carbonate Scale Adhesion on Various Material Surfaces, Zairyo-to-Kankyo. 60 (2011) 296–303. https://doi.org/10.3323/jcorr.60.296.

[32] N. Spanos, P.G. Koutsoukos, The transformation of vaterite to calcite: Effect of the conditions of the solutions in contact with the mineral phase, J. Cryst. Growth. 191 (1998) 783–790. https://doi.org/10.1016/S0022-0248(98)00385-6.

[33] K. Ishikawa, S. Matsuya, Y. Miyamoto, K. Kawate, 9.05 - Bioceramics, in: Compr. Struct. Integr., Elsevier Ltd, 2007: pp. 169–214. https://doi.org/10.1016/B0-08-043749-4/09146-1.

[34] O. Devos, S. Jakab, C. Gabrielli, S. Joiret, B. Tribollet, S. Picart, Nucleation-growth process of scale electrodeposition - influence of the magnesium ions, J. Cryst. Growth. 311 (2009) 4334–4342. https://doi.org/10.1016/j.jcrysgro.2009.07.021.

[35] D. Hasson, D. Bramson, B. Limoni-Relis, R. Semiat, Influence of the flow system on the inhibitory action of CaCO3 scale prevention additives, Desalination. 108 (1997) 67–79. https://doi.org/10.1016/S0011-9164(97)00010-6.

[36] R. Hidema, T. Toyoda, H. Suzuki, Y. Komoda, Y. Shibata, Adhesive behavior of a calcium carbonate particle to solid walls having different hydrophilic characteristics, Int. J. Heat Mass Transf. 92 (2016) 603–609. https://doi.org/10.1016/j.ijheatmasstransfer.2015.08.068.

[37] J.W. Mullin, Crystallisation, 2nd editio, 1972.

[38] R.S. Feigelson, Crystal Growth through the Ages: A Historical Perspective, in: Handb. Cryst. Growth Second Ed., 2015. https://doi.org/10.1016/B978-0-444-56369-9.00001-0.

[39] E. Mavredaki, A. Neville, Prediction and evaluation of calcium carbonate deposition at surfaces, Soc. Pet. Eng. - SPE Int. Conf. Exhib. Oilf. Scale 2014. (2014) 616–629. https://doi.org/10.2118/169796-ms.

[40] K.Z. Abdelgawad, M.A. Mahmoud, Effect of CO2 flooding during EOR process on the rock petrophysical and electrical properties, Soc. Pet. Eng. - North Africa Tech. Conf. Exhib. 2013, NATC 2013. 2 (2013) 1132–1143. https://doi.org/10.2118/164730-ms.

[41] J. Moghadasi, M. Jamialahmadi, H. Müller-Steinhagen, A. Sharif, Formation Damage Due to Scale Formation in Porous Media Resulting From Water Injection, Proc. - SPE Int. Symp. Form. Damage Control. (2004) 581–591. https://doi.org/10.2523/86524-ms.

[42] H. Roques, A. Girou, Kinetics of the formation conditions of carbonate tartars, Water Res. 8 (1974) 907–920. https://doi.org/10.1016/0043-1354(74)90105-5.

[43] S. Ouoba, F. Cherblanc, J. Koulidiati, J.C. Bénet, A New Experimental Method to Determine the Henry's Law Constant of a Volatile Organic Compound Adsorbed in Soil, J. Chem. 2015 (2015) 20–23. https://doi.org/10.1155/2015/479327.

[44] O.J. Vetter, V. Kandarpa, PREDICTION OF CaCO3 SCALE UNDER DOWNHOLE CONDITIONS., Mater. Res. Bull. (1980) 155–165.

[45] Y. Zhang, R. Farquhar, Laboratory determination of calcium carbonate scaling rates for oilfield wellbore environments, Soc. Pet. Eng. - Int. Symp. Oilf. Scale 2001. (2001) 1–7. https://doi.org/10.2523/68329-ms.

[46] Ç.M. Oral, B. Ercan, Influence of pH on morphology, size and polymorph of room temperature synthesized calcium carbonate particles, Powder Technol. 339 (2018) 781–788. https://doi.org/10.1016/j.powtec.2018.08.066.

[47] W.C. Cheong, P.H. Gaskell, A. Neville, Substrate effect on surface adhesion/crystallisation of calcium carbonate, J. Cryst. Growth. 363 (2013) 7–21. https://doi.org/10.1016/j.jcrysgro.2012.09.025.

[48] E. Ruckenstein, G.O. Berim, Kinetics of heterogeneous nucleation on a rough surface: Nucleation of a liquid phase in nanocavities, J. Colloid Interface Sci. 351 (2010) 277–282. https://doi.org/10.1016/j.jcis.2010.06.045.

[49] D.J. Gunn, Effect of surface roughness on the nucleation and growth of calcium sulphate on metal surfaces, J. Cryst. Growth. 50 (1980) 533–537. https://doi.org/10.1016/0022-0248(80)90104-9.

[50] Z. Wang, A. Neville, A.W. Meredith, How and why does scale stick - Can the surface be engineered to decrease scale formation and adhesion?, SPE Seventh Int. Symp. Oilf. Scale 2005 Push. Boundaries Scale Control. Proc. (2005) 85–92. https://doi.org/10.2523/94993-ms.

[51] L. Sutherland, C. Johnston, T. Herrman, The influence of turbulence (or hydrodynamic effects) on strontium sulphate scale formation and inhibitor performance, Soc. Pet. Eng. - SPE Int. Conf. Exhib. Oilf. Scale 2014. (2014)

167–176. https://doi.org/10.2118/169760-ms.

[52] J. Thompson, N. Lin, E. Lyster, R. Arbel, T. Knoell, J. Gilron, Y. Cohen, RO membrane mineral scaling in the presence of a biofilm, J. Memb. Sci. 415–416 (2012) 181–191. https://doi.org/10.1016/j.memsci.2012.04.051.

[53] E. Lyster, M. man Kim, J. Au, Y. Cohen, A method for evaluating antiscalant retardation of crystal nucleation and growth on RO membranes, J. Memb. Sci. 364 (2010) 122–131. https://doi.org/10.1016/j.memsci.2010.08.020.

[54] M. Euvrard, C. Filiatre, E. Crausaz, A cell to study in situ electrocrystallization of calcium carbonate, J. Cryst. Growth. 216 (2000) 466–474. https://doi.org/10.1016/S0022-0248(00)00366-3.

[55] O. Sanni, O. Bukuaghangin, M. Huggan, N. Kapur, T. Charpentier, A. Neville, Development of a novel once-Through flow visualization technique for kinetic study of bulk and surface scaling, Rev. Sci. Instrum. 88 (2017). https://doi.org/10.1063/1.4991729.

[56] J. Wang, J.S. Buckley, J.L. Creek, Asphaltene deposition on metallic surfaces, J. Dispers. Sci. Technol. 25 (2004) 287–298. https://doi.org/10.1081/DIS-120037697.

[57] K.A. Lawal, J.P. Crawshaw, E.S. Boek, V. Vesovic, Experimental investigation of asphaltene deposition in capillary flow, Energy and Fuels. 26 (2012) 2145–2153. https://doi.org/10.1021/ef201874m.

[58] R. Pal, C.Y.J. Hwang, Loss coefficients for flow of surfactant-stabilized emulsions through pipe components, Chem. Eng. Res. Des. 77 (1999) 685–691. https://doi.org/10.1205/026387699526818.

[59] R.M. Turian, T.W. Ma, F.L.G. Hsu, M.D.J. Sung, G.W. Plackmann, Flow of concentrated non-newtonian slurries: 2. Friction losses in bends, fittings, valves and Venturi meters, Int. J. Multiph. Flow. 24 (1998) 243–269. https://doi.org/10.1016/S0301-9322(97)00039-6.

[60] F.M. White, Fluid Mechanichs, 7th Edition, 2011. https://doi.org/10.1016/B978-0-12-546801-5.50017-7.

[61] D.C. Bogue, Entrance Effects and Prediction of Turbulence in Non-Newtonian Flow, Ind. Eng. Chem. 51 (1959) 874–878. https://doi.org/10.1021/ie50595a044.

[62] Y.A. Cengel, J. Cimbala., Fluid Mechanics Fundamentals and Applications, Mc-Graw-Hill International Edition, 2006.

[63] A.H. Shapiro, Pressure fields and fluid acceleration, Plaza & Janés. (1968).

[64] O. Fluid, D. Meeting, Y. Yusuf, R. Sabbagh, D.S. Nobes, Flow convergence model for flow through long aspect ratio rectangular orifices, Okanagan Fluid Dyn. Meet. August 21-24, 2017, Kelowna, Br. Columbia, Canada. (2017).

[65] Y. Yusuf, Flow Convergence and Pressure Loss Characteristics in Viscous Flow through Rectangular Orifices with Applications in Porous Media, University of Alberta, Canada, 2019.

[66] Y. Yusuf, S. Ansari, M. Bayans, R. Sabbagh, M. El Hassan, D.S. Nobes, Study of Flow Convergence in Rectangular Slots using Particle Shadowgraph Velocimetry, in: 5th International Conference on Experimental Fluid Mechanics – ICEFM 2018 Munich, Germany, 2018.

[67] M.S.N. Oliveira, L.E. Rodd, G.H. McKinley, M.A. Alves, Simulations of extensional flow in microrheometric devices, Microfluid. Nanofluidics. 5 (2008) 809–826. https://doi.org/10.1007/s10404-008-0277-5.

[68] V. Zivkovic, P. Zerna, Z.T. Alwahabi, M.J. Biggs, A pressure drop correlation for low Reynolds number Newtonian flows through a rectangular orifice in a similarly shaped micro-channel, Chem. Eng. Res. Des. 91 (2013) 1–6. https://doi.org/10.1016/j.cherd.2012.05.022.

[69] Y. Yusuf, R. Sabbagh, D.S. Nobes, Semi-empirical pressure loss model for viscous flow through high aspect ratio rectangular orifices, Phys. Fluids. 31 (2019). https://doi.org/10.1063/1.5096663.

[70] Handbook A. S. H. R. A. E, HVAC fundamentals, SI Edition, 2001.

[71] D.A. McNeil, J. Addlesee, A. Stuart, An experimental study of viscous flows in contractions, J. Loss Prev. Process Ind. 12 (1999) 249–258. https://doi.org/10.1016/S0950-4230(99)00008-X.

[72] V. Pienaar, Veruscha, Viscous flow through sudden contractions, (2004).

[73] S.-J. Lee, G.-B. Kim, Analysis of Flow Resistance Inside Microchannels With Different Inlet Configurations Using Micro-PIV System, in: Proc. ICMM2003 Microchannels Minichannels April 24-25, 2003, Rochester, New York, USA, 2003: pp. 1–5.

[74] T. Ahmad, I. Hassan, Experimental analysis of microchannel entrance length characteristics using microparticle image velocimetry, J. Fluids Eng. Trans. ASME. 132 (2010). https://doi.org/10.1115/1.4001292.

[75] J. Oak, D. V. Pence, J.A. Liburdy, Flow development of co-flowing streams

in rectangular micro-channels, Microscale Thermophys. Eng. 8 (2004) 111–128. https://doi.org/10.1080/10893950490445289.

[76] B. Atkinson, M.P. Brocklebank, C.C.H. Card, J.M. Smith, Low Reynolds number developing flows, AIChE J. 15 (1969) 548–553. https://doi.org/10.1002/aic.690150414.

[77] J.S. Vrentas, J.L. Duda, K.G. Bargeron, Effect of axial diffusion of vorticity on flow development in circular conduits: Part I. Numerical solutions, AIChE J. 12 (1966) 837–844. https://doi.org/10.1002/aic.690120504.

[78] S.Y. Lee, J. Jang, S.T. Wereley, Effects of planar inlet plenums on the hydrodynamically developing flows in rectangular microchannels of complementary aspect ratios, Microfluid. Nanofluidics. 5 (2008) 1–12. https://doi.org/10.1007/s10404-007-0179-y.

[79] O. Fluid, D. Meeting, Y. Yusuf, R. Sabbagh, D.S. Nobes, Flow convergence model for flow through long aspect ratio rectangular orifices, in: Okanagan Fluid Dyn. Meet. August 21-24, 2017, Kelowna, Br. Columbia, Canada, 2017.

[80] E.M. Sparrow, Experiments on Laminar Flow Development in Rectangular Ducts, (2013).

[81] C.L. Wiginton, C. Dalton, Incompressible Laminar Flow in the Entrance Region of a Rectangular Duct, J. Appl. Mech. Trans. ASME. 51 (1969) 784. https://doi.org/10.2106/00004623-196951040-00021.

[82] L.S. Han, Hydrodynamic entrance lengths for incompressible laminar flow in rectangular ducts, J. Appl. Mech. Trans. ASME. 28 (1960) 314.

https://doi.org/10.1115/1.3641688.

[83] G.F. Muchnik, S.D. Solomonov, A.R. Gordon, Hydrodynamic development of a laminar velocity field in rectangular channels, J. Eng. Phys. 25 (1973) 1268–1271. https://doi.org/10.1007/BF00834770.

[84] H. Li, B. Huang, M. Wu, Experimental and numerical investigations on the flow characteristics within hydrodynamic entrance regions in microchannels, Micromachines. 10 (2019). https://doi.org/10.3390/mi10050317.

[85] R.J. Goldstein, D.K. Kreid, Measurement of laminar flow development in a square duct using a laser-doppler flowmeter, J. Appl. Mech. Trans. ASME. 34 (1964) 813–818. https://doi.org/10.1115/1.3607839.

[86] P.F. Hao, F. He, K.Q. Zhu, Flow characteristics in a trapezoidal silicon microchannel, J. Micromechanics Microengineering. 15 (2005) 1362–1368. https://doi.org/10.1088/0960-1317/15/6/029.

[87] S. Lee, S.T. Wereley, L. Gui, Microchannel Flow Measurement Using Micro Particle Image Velocimetry, ASME 2002 Int. Mech. Eng. Congr. Expo. (2002) 1–8.

[88] B.A. Finlayson, P.W. Drapala, M. Gebhardt, M.D. Harrison, B. Johnson, M. Lukman, S. Kunaridtipol, T. Plaisted, Z. Tyree, J. Vanburen, A. Witarsa, Microcomponent Flow Characterization, Micro Instrum. High Throughput Exp. Process Intensification-a Tool PAT. (2007) 181–208. https://doi.org/10.1002/9783527610624.ch8.

[89] M.F. Edwards, M.S.M. Jadallah, R. Smith, Head Losses in Pipe Fittings At Low Reynolds Numbers., Chem. Eng. Res. Des. 63 (1985) 43–50.

[90] G. Astarita, G. Greco, Excess pressure drop in laminar flow through sudden contraction: Newtonian Liquids, Ind. Eng. Chem. Fundam. 7 (1968) 27–31. https://doi.org/10.1021/i160025a005.

[91] M. Raffael, C. Willert, S.T. Wereley, J. Kompenhans, Particle Image Velocimetry (the Third Edition), 2007. https://doi.org/10.1007/978-3-540-72308-0.

[92] R. Castrej, The shadowgraph imaging technique and its modern application to fluid jets and drops, Rev. Mex. Física. 57 (2011) 266–275.

[93] J. Novotny, L. Manoch, The criterion of choosing the proper seeding particles, Eng. Mech. (2012) 945–954.

[94] J.P. Gustaffson, Visual MINTEQ – a free equilibrium speciation model, Vis. MINTEQ. (2013) 1. https://vminteq.lwr.kth.se/.

[95] U. Shavit, R.J. Lowe, J. V. Steinbuck, Intensity Capping: A simple method to improve cross-correlation PIV results, Exp. Fluids. 42 (2007) 225–240. https://doi.org/10.1007/s00348-006-0233-7.

[96] C. Willert, Stereoscopic digital particle image velocimetry for application in wind tunnel flows, Meas. Sci. Technol. 8 (1997) 1465–1479. https://doi.org/10.1088/0957-0233/8/12/010.

[97] LaVision, Product Manual for DaVis 8.2: FlowMaster, 2014.

[98] L. Johansson, H. Wettergren, Computation of the pressure distribution in hydrodynamic bearings using Newton's method, J. Tribol. 126 (2004) 404–406. https://doi.org/10.1115/1.1631009.

[99] B.W. Van Oudheusden, PIV-based pressure measurement, Meas. Sci. Technol. 24 (2013). https://doi.org/10.1088/0957-0233/24/3/032001.

[100] S. Ansari, Y. Yusuf, R. Sabbagh, D.S. Nobes, Determining the pressure distribution of a multi-phase flow through a pore space using velocity measurement and shape analysis, Meas. Sci. Technol. 30 (2019). https://doi.org/10.1088/1361-6501/ab0afc.

[101] S. Ansari, Y. Yusuf, R. Sabbagh, H. Soltani, L. Kinsale, D.S. Nobes, An imaging derivation of the pressure field of a multi-phase flow in a porous media using μ-SPIV, 19th Int. Symp. Appl. Laser Imaging Tech. to Fluid Mech. Lisbon, Port. JULY 16 – 19. (2018).

[102] A. Gilat, V. Subramaniam, Numerical Methods for Engineers and Scientists, Third Edit, 2014.

[103] V.J. Logeeswaran, A. Sarkar, M.S. Islam, N.P. Kobayashi, J. Straznicky, X. Li, W. Wu, S. Mathai, M.R.T. Tan, S.Y. Wang, R.S. Williams, A 14-ps full width at half maximum high-speed photoconductor fabricated with intersecting InP nanowires on an amorphous surface, Appl. Phys. A Mater. Sci. Process. 91 (2008) 1–5. https://doi.org/10.1007/s00339-007-4394-x.

[104] N. Ernst, G. Bozdech, H. Schmidt, W.A. Schmidt, G.L. Larkins, On the full-width-at-half-maximum of field ion energy distributions, Appl. Surf. Sci. 67 (1993) 111–117. https://doi.org/10.1016/0169-4332(93)90301-Q.

[105] A. Kaufmann, Strategy for the elucidation of elemental compositions of trace analytes based on a mass resolution of 100 000 full width at half maximum, Rapid Commun. Mass Spectrom. 24 (2010) 1457–1466.

https://doi.org/10.1002/rcm.

[106] A. Wheeler, G. Ahmad, Introduction to Engineering Experimentation, 3rd editio, Pearson Education, San Francisco, California, 2010.

[107] H. Soltani, Transport of Bubbles and Oil Droplets Rising in a Net Co-Flow through a Rectangular Confinement, University of Alberta, 2018.

[108] J.G. Santiago, S.T. Wereley, C.D. Meinhart, D.J. Beebe, R.J. Adrian, A particle image velocimetry system for microfluidics, Exp. Fluids. 25 (1998) 316–319. https://doi.org/10.1007/s003480050235.

APPENDIX

Appendix A1: Image acquisition code for the scaling experiment in LabView/CVI 2010

(a)

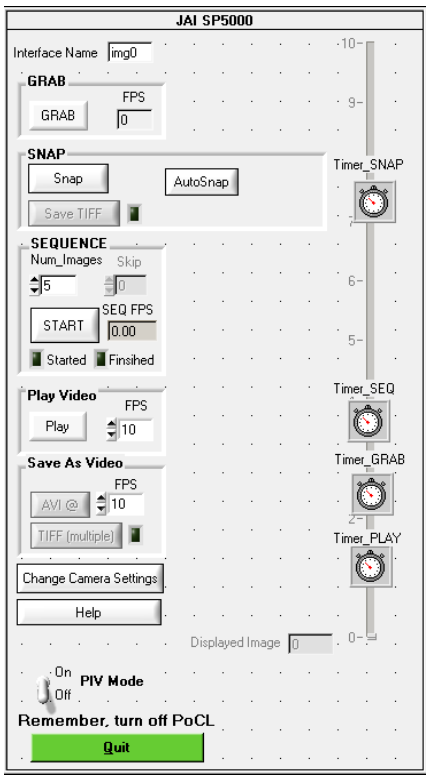

(b)

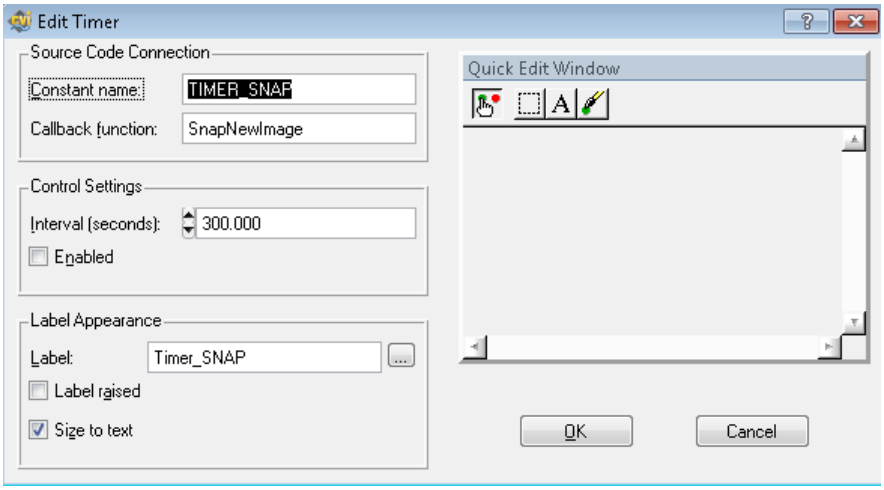

Figure A1: JAI SP5000 (a) GUI (b) Timer options

```
/*************************************************************/
//-------------------------------------------------------------
//                  JAI_SP_5000
//-------------------------------------------------------------
//
// Who:     D.S.Nobes, Dept Mech Eng, University of Alberta


//
// Description:
//          For image collectiona and camera conrol of a single
//          JAI SP-5000 (momochrome) camera
// VERSION:
// 01/03/2014:  - Control of ExpTime, Gain, Triggering
//              - Collect in Grab and Sequence modes
//
// Bianca Angotti
// 5/25/2016:   - Save TIFFs
//              - button alterations, additional panels, code cleanup
// TO DO:       - Error handling
//              - Snap
//              - change settings
/*************************************************************/


/*********************************************************************/
//* SnapNewImage gets the new image*/
//  Modified by: Pavan Kamble, and Yishal Yusuf, Dept Mech Eng, University of
Alberta
//  When:   August 2019
/*********************************************************************/




int CVICALLBACK SnapNewImage (int panel, int control, int event,
              void *callbackData, int eventData1, int eventData2)
{
       static int nbFrame;
```

```
	char filename3[MAX_PATHNAME_LEN];
	switch (event)
	{
		case EVENT_TIMER_TICK:
			t10 = Timer();
			if (!image_snap)  {
				// create an image
				image_snap = imaqCreateImage (IMAQ_IMAGE_U8, 0);

				// snap a picture
				imaqSnap (sid, image_snap,IMAQ_NO_RECT);
				// after this point, image_snap shall be saved as the
file(eg. File_0001)

				// Display using IMAQ Vision
				//imaqSetBorderSize(image, 2);
				//imaqDisplayImage (image_snap, 0, TRUE);

				// allow saving
				//SetCtrlAttribute (panelHandle, PANEL_SAVE_SNAP,
ATTR_DIMMED, 0);
				// Close the interface and the session
				//IMAQdxCloseCamera (session);

			}
			else {
				// dispose of the images and create a new one
				imaqDispose(image_snap);
			    image_snap = NULL;
			    image_snap = imaqCreateImage (IMAQ_IMAGE_U8, 0);

				// snap a picture
				imaqSnap (sid, image_snap,IMAQ_NO_RECT);

				// Display using IMAQ Vision
				//imaqDisplayImage (image_snap, 0, TRUE);

				// allow saving
				//SetCtrlAttribute (panelHandle, PANEL_SAVE_SNAP,
ATTR_DIMMED, 0);
				// Close the interface and the session
				//IMAQdxCloseCamera (session);
			}

			//FileSelectPopup ("", "*.tif", "*.tif", "Name of File to
Save", VAL_SAVE_BUTTON, 0, 1, 1, 1, snap_filename9);


			strcpy(snap_filename,snap_filename);
			strcat(snap_filename,"%d.tif");
			sprintf(snap_filename, snap_filename, NULL);
			imaqWriteTIFFFile(image_snap,snap_filename,0,NULL);
			break;

			// fill in filename2 with filename3 with the number
			// sprintf (filename2, filename3, frame);
			// write the image frame to that filename
```

```
                        // imaqWriteTIFFFile(images[frame],filename2,0,NULL);
        }
        return 0;
}
```

Published with MATLAB® R2017a

Appendix A2: Matlab code for 2D-velocity field

```
%%%%%%%%%%%%%%%%%%%%%%%%%%%%%%%%%%%%%%%%%%%%%%%%%%%%%%%%%%%%%%%%%%%%%%%%%%%%
% Code for 2D-Velocity field
% Original code: By Beatriz Bravo and Hirad Soltani
% Modified by: Pavan Kamble
% The code loads the raw images from the davis and *.VC7 fiels
% Code output: 2D velocity field, streamlines and streamwise velocity
% profile
%%%%%%%%%%%%%%%%%%%%%%%%%%%%%%%%%%%%%%%%%%%%%%%%%%%%%%%%%%%%%%%%%%%%%%%%%%%%
%clearing all variables
clear all;
%closing all figures
close all;
%clearing the command area
clc;
warning('off')
font_size = 20;%font size
f=2000; %Camera frame rate in Hz
%loading the raw images
path =
'C:\MyProjects8.3\PIV_E3_03_8th_September_Straight_empty_1200_30000...\1200_straig
ht_30000_C001H001S0001_old\';
FV = 'B00001.im7';
v = loadvec([path FV]);
v=rotatef(v,angle_rotation,-0.8734,4.341); %rotatef function to rotate the vector

% Displays the raw image in figure-1
figure(1);
set(1,'pos',[70 25 800 700]);
set(gca,'fontsize',font_size);
set(gca,'FontName', 'Times New Roman');
set(gcf,'color','w');
hold on
showf(v); %Displays the raw image

% 2D-Velocity profile plot
%loads the *.VC7 files from Davis
%Path for data
path_vp =
'C:\MyProjects8.3\PIV_E3_03_8th_September_Straight_empty_1200_30000\1200_straight_
30000_C001H001S0001_old\TR_SOC_MP(4x32x32_87%ov)\Smooth(5x,fit=P1,n=16,ouliers=1)\
';
FV_vp = 'B00001.vc7';
v_vp = loadvec([path_vp FV_vp]);

w=0.87;%widht of the channel
v_vp.x=v_vp.x-2.211; %To make the width centre zero
```

```
v_vp.y=v_vp.y+2.0904; %Shows the zero at the entrance
v_vp.vy = v_vp.vy.*f*1; %Conversion to mm/s
v_vp.vx = v_vp.vx.*f*1; %Conversion to mm/s
V_Max = max(max(v_vp.vy(:,:)));%Maximum velocity

Vnorm = vec2scal(v_vp,'norm'); %converts the vector field into scalar field using
sqrt(u.^2+v.^2)
vvv = Vnorm.w; %grabs the magnitude of velocity of scalar field
vvv= imrotate(vvv,-90); %rotates whole field by -90 degrees
vvv = flipdim(vvv ,2); %mirrors whole field %Need to rotate to get the scalar
field

figure(2)
hold on
set(2,'pos',[1000 250 800 700]);
set(gca,'fontsize',font_size);
set(gca,'FontName', 'Times New Roman');
set(gcf,'color','w');
h = imagesc(v_vp.x/w,v_vp.y/w,vvv);
colormap('jet(20)');
c = colorbar;
% set(c,'YTick',0:0.5:4)
hold on;
quiver(v_vp.x(1:3:end)./w,v_vp.y(1:9:end)'./w,v_vp.vx(1:3:end,1:9:end)',v_vp.vy(1:
3:end,1:9:end)', ...
    'color','k', ...
    'AutoScaleFactor',0.8,'LineWidth',1.5);
%plot streamlines
[sx sy] = meshgrid(-4:0.25:4,-3:0.5:5.8);
g = streamline(v_vp.x/w,v_vp.y'/w,v_vp.vx',v_vp.vy',sx(:),sy(:));
set(g,'LineWidth',1.5,'color','w');
hold off
axis tight;
axis([-4 4 -2 7.5]);
yticks([-2 0 2 4 6])
set(gca,'Ydir','normal')
caxis([0 120])
% %Label the axis
xlabel('{\itx/w_0 }','FontSize',font_size,'FontName', 'Times New Roman');
ylabel('{\ity/w_0 }','FontSize',font_size,'FontName', 'Times New Roman');
ylabel(c,'{\itV}{ (mm/s)}','FontSize',font_size,'FontName', 'Times New Roman')

alphamap = zeros(size(vvv,1),size(vvv,2));
for i = 0:size(vvv,1)-1
    for j = 0:size(vvv,2)-1
        if(~(vvv(i+1,j+1) == 0))
            alphamap(i+1,j+1) = 1;
        end
    end
end

set(h, 'AlphaData', alphamap);

%Plots the streamwise centerline velocity for three flow rates
figure(3)
set(3,'pos',[100 200 800 700]);
p1=plot(v_vp_Straight_900.y(12:260)/w_Straight_900,
```

```
mean(v_vp_Straight_900.vy(165:166,12:260))/mean(v_vp_Straight_900.vy(165:166,66)),
...
    'ko','LineWidth',1,'MarkerSize',3);
hold on
p2=plot(v_vp_Straight_1200.y(12:260)/w_Straight_1200,
mean(v_vp_Straight_1200.vy(165:166,12:260))/mean(v_vp_Straight_1200.vy(165:166,66)
),...
    'co','LineWidth',1,'MarkerSize',3);
p3=plot(v_vp_Straight_1500.y(12:260)/w_Straight_1500,
mean(v_vp_Straight_1500.vy(165:166,12:260))/mean(v_vp_Straight_1500.vy(165:166,66)
),...
    'ro','LineWidth',1,'MarkerSize',3);
plot([-2 0], [1 1],'k:','LineWidth',2)
plot([0 0], [1 0],'k:','LineWidth',2)
xlabel('{\ity/w_0} ','FontSize',font_size,'FontName', 'Times New Roman');
ylabel('Centreline velocity, {\itV/V_0} ','FontSize',font_size,'FontName', 'Times
New Roman');
xlim([-2.0 7.0])
ylim([0 1.5])
xticks([-2 -1 0 1 2 3 4 5 6 7])
grid on
% legend([p1,p2,p3],'Straight,900 ml/hr','Straight,1200 ml/hr','Straight,1500
ml/hr','Location','east');
set(gca,'fontsize',font_size)
set(gca,'FontName', 'Times New Roman')
set(gcf,'color','w');
leg1=legend([p1,p2,p3],'{\itQ} = 900 ml/hr','{\itQ} = 1200 ml/hr','{\itQ} = 1500
ml/hr','Location','northeast');
a=axes('position',get(gca,'position'),'Color', 'none', 'Box',
'Off','visible','off');
% leg2=legend(a,[p4 p5 p6],'900 ml/hr','1200 ml/hr','1500
ml/hr','Location','northeast');
set(leg1,'FontSize',font_size*0.9)
set(leg1,'FontName', 'Times New Roman')
% set(leg2,'FontSize',font_size*0.9)
% set(leg2,'FontName', 'Times New Roman')
title(leg1,'Straight slot ', 'fontweight', 'normal','FontSize',font_size*0.9)
% title(leg2,'Rounded', 'fontweight', 'normal','FontSize',font_size*0.9)
hold off

%Theoretical velocity profile
yy_w=(-0.5:0.01:0.5);
VEC_w=(1-(2.*yy_w).^2);

%Straight,900ml/hr
y_w_Straight_900=v_vp_Straight_900.y/w_Straight_900;
y_w_Straight_900_step=((y_w_Straight_900(2)-y_w_Straight_900(1))/2);
%Automatically detects the velocity profiles at y/w=1, y/w=2, etc
y_w_Straight_900_pos_1=find (y_w_Straight_900>(1-y_w_Straight_900_step) &
y_w_Straight_900<(1+y_w_Straight_900_step));
y_w_Straight_900_pos_2=find (y_w_Straight_900>(2-y_w_Straight_900_step) &
y_w_Straight_900<(2+y_w_Straight_900_step));
y_w_Straight_900_pos_3=find (y_w_Straight_900>(3-y_w_Straight_900_step) &
y_w_Straight_900<(3+y_w_Straight_900_step));
y_w_Straight_900_pos_4=find (y_w_Straight_900>(4-y_w_Straight_900_step) &
y_w_Straight_900<(4+y_w_Straight_900_step));
y_w_Straight_900_pos_5=find (y_w_Straight_900>(5-y_w_Straight_900_step) &
```

```
y_w_Straight_900<(5+y_w_Straight_900_step));
y_w_Straight_900_pos_6=find (y_w_Straight_900>(6-y_w_Straight_900_step) &
y_w_Straight_900<(6+y_w_Straight_900_step));
y_w_Straight_900_pos_7=find (y_w_Straight_900>(7-y_w_Straight_900_step) &
y_w_Straight_900<(7+y_w_Straight_900_step));

figure(4)
set(4,'pos',[1000 200 800 700]);
p1=plot((v_vp_Straight_900.x(151:180)/(v_vp_Straight_900.x(180)-
v_vp_Straight_900.x(151))+0.0129),...
    (v_vp_Straight_900.vy(151:180,
91))/(max(v_vp_Straight_900.vy(151:180,91))),...
    'o','MarkerEdgeColor','w','MarkerFaceColor','c','MarkerSize',7);
hold on
p2=plot((v_vp_Straight_900.x(151:180)/(v_vp_Straight_900.x(180)-
v_vp_Straight_900.x(151))+0.0129),...
    (v_vp_Straight_900.vy(151:180,
122))/(max(v_vp_Straight_900.vy(151:180,122))),...
    's','MarkerEdgeColor','w','MarkerFaceColor','c','MarkerSize',7);
p3=plot((v_vp_Straight_900.x(151:180)/(v_vp_Straight_900.x(180)-
v_vp_Straight_900.x(151))+0.0129),...
    (v_vp_Straight_900.vy(151:180,
148))/(max(v_vp_Straight_900.vy(151:180,148))),...
    'o','MarkerEdgeColor','w','MarkerFaceColor','b','MarkerSize',7);
p4=plot((v_vp_Straight_900.x(151:180)/(v_vp_Straight_900.x(180)-
v_vp_Straight_900.x(151))+0.0129),...
    (v_vp_Straight_900.vy(151:180,
176))/(max(v_vp_Straight_900.vy(151:180,176))),...
    's','MarkerEdgeColor','w','MarkerFaceColor','b','MarkerSize',7);
p5=plot((v_vp_Straight_900.x(151:180)/(v_vp_Straight_900.x(180)-
v_vp_Straight_900.x(151))+0.0129),...
    (v_vp_Straight_900.vy(151:180,
197))/(max(v_vp_Straight_900.vy(151:180,197))),...
    'o','MarkerEdgeColor','w','MarkerFaceColor','k','MarkerSize',7);
p6=plot((v_vp_Straight_900.x(151:180)/(v_vp_Straight_900.x(180)-
v_vp_Straight_900.x(151))+0.0129),...
    (v_vp_Straight_900.vy(151:180,
226))/(max(v_vp_Straight_900.vy(151:180,226))),...
    's','MarkerEdgeColor','w','MarkerFaceColor','k','MarkerSize',7);
p7=plot((v_vp_Straight_900.x(151:180)/(v_vp_Straight_900.x(180)-
v_vp_Straight_900.x(151))+0.0129),...
    (v_vp_Straight_900.vy(151:180,
y_w_Straight_900_pos_7))/(max(v_vp_Straight_900.vy(151:180,y_w_Straight_900_pos_7)
)),...
    'o','MarkerEdgeColor','w','MarkerFaceColor','m','MarkerSize',7);
p8=plot(yy_w,VEC_w,'r-');
xlim([-0.5 0.5])
ylim([0 1])
set(gca,'fontsize',font_size)
set(gca,'FontName', 'Times New Roman')
legend([p1,p2,p3,p4,p5,p6,p7,p8],'{\ity/w_0}=1','{\ity/w_0}=2','{\ity/w_0}=3','{\i
ty/w_0}=4','{\ity/w_0}=5','{\ity/w_0}=6',...
    '{\ity/w_0}=7','Theory','Location','best');
xlabel('{\itx/w_0} ','FontSize',font_size,'FontName', 'Times New Roman');
ylabel('Centreline velocity, {\itV/V_{Max}} ','FontSize',font_size,'FontName',
'Times New Roman');
```

```
set(gcf,'color','w');
hold off
```

Published with MATLAB® R2017a

Appendix A3: Matlab code for 2D-pressure field

```
%%%%%%%%%%%%%%%%%%%%%%%%%%%%%%%%%%%%%%%%%%%%%%%%%%%%%%%%%%%%%%%%%%%%%%%%%%%%%%%
%  Code to estimate the 2D-pressure field
%  Reference:
%  Gurka R., Liberzon A., Hefetz D., Rubinstein D. and Shavit U.,
% "Computation of Pressure Distribution Using PIV Velocity Data",
%  3rd International Workshop on Particle Image Velocimetry, Santa Barbara,
%  California, September 16-18, 1999.
%
%  Code modified by: Reza Azadi, Dept of Mech Engg, Uiversity of Alberta
%%%%%%%%%%%%%%%%%%%%%%%%%%%%%%%%%%%%%%%%%%%%%%%%%%%%%%%%%%%%%%%%%%%%%%%%%%%%%%%

clc
clear
close all
font_size=22;
w=0.8441;%slot width

f = 2000; % frame rate in frames per second
ro = 1000 ; % [kg/m^3]

Load the VC7 file and do some scaling

VEC = loadvec('B00001_noscaling.vc7');% Load the data into a variable

VEC = loadvec('B00001.vc7');
% VEC = loadvec('B00001_withscaling.vc7');

x = VEC.x ; % [mm]
y = VEC.y ; % [mm]

dx = x(2) - x(1) ; % [mm]
dy = y(2) - y(1) ; % [mm]

dx = 0.001 * dx ; % [m]
dy = 0.001 * dy ; % [m]

x = x + abs( x(1) ) ;
y = y + abs( y(1) ) ;

% x = x./ dx ;
% y = y./ dy ;

U = VEC.vx ; % [mm/f]
V = VEC.vy ; % [mm/f]

U = ( U .* f )' ./ 1000 ; % [m/s]
V = ( V .* f )' ./ 1000 ; % [m/s]

Size = size( U ) ;
```

```
% gradients

[Uy, Ux] = gradient( U ) ;

Ux = Ux ./ dx ;
Uy = Uy ./ dx ;

[ Vy, Vx ] = gradient( V ) ;

Vx = Vx ./ dy ;
Vy = Vy ./ dy ;

Umag = sqrt( U.^2 + V.^ 2 ) ;

rhs = (Ux.^2 + Vy.^2 + 2*Uy.*Vx);

% Pressure matrix initialization with boundary conditions:
P1 = zeros(Size);
P2 = zeros(Size);
PP1 = P1;
PP2 = P2;
% Optimal lambda:
% Ref: http://www.enm.bris.ac.uk/admin/courses/ANA&PDEs/pde-lect8.pdf
tmpc = cos(pi/(31+1)) + cos(pi/(30+1));
lambda = 4/(2+sqrt(4-tmpc^2));
% lambda = 1.8; % weighting factor

% Poisson equation solution by Liebmann's (iterative) method

tol = 1e-6;            % error is 1%
maxerr = inf;   % initial error
iter = 0;

while maxerr > tol
    iter = iter + 1;

    disp(['Iteration no. ',num2str(iter)]);
    for c = 2:Size(2)-1

        for r = 2:Size(1)-1

            if Umag( r, c ) ~= 0

                A = P1(r-1,c);
                B = P1(r+1,c);
                C = P1(r,c-1);
                D = P1(r,c+1);
                E = ro*rhs(r,c).*(dx^2);
                F = ro*9.81*y(r)/1000;

                A2 = P2(r-1,c);
                B2 = P2(r+1,c);
                C2 = P2(r,c-1);
                D2 = P2(r,c+1);
                E2 = ro*rhs(r,c).*(dx^2);
                F2 = ro*9.81*y(r)/1000;
```

```
                P1(r,c) =F-0.25*( A+B+C+D+E);
                P2(r,c) =0.25*( A2+B2+C2+D2+E2);
                P1(r,c) = lambda*P1(r,c) + (1-lambda)*PP1(r,c);
                P2(r,c) = lambda*P2(r,c) + (1-lambda)*PP2(r,c);

            end
        end

    end

    maxerr = max(max(abs((P1-PP1)./P1)));
    disp(['Maximum error is  ',num2str(maxerr)]);
    PP1 = P1;

    maxerrp = max(max(abs((P2-PP2)./P2)));
    disp(['Maximum error is  ',num2str(maxerrp)]);
    PP2 = P2;
    % as long the error larger than tolerance, continue

end

    for c = 2:Size(2)-1

        for r = 2:Size(1)-1
            if P1( r, c ) ~= 0
               P1( r, c ) =  -P1( r, c ) ;

            else
               P1( r, c ) = NaN ;

               Umag( r, c ) = NaN ;
            end
        end

    end

        for c = 2:Size(2)-1

        for r = 2:Size(1)-1
            if P2( r, c ) ~= 0
               P2( r, c ) =  -P2( r, c ) ;
            else
               P2( r, c ) = NaN ;

            end
        end

        end

% Plot the velocity-field

[X, Y] = meshgrid( x, y ) ;
figure (1)
set(1,'pos',[100 250 800 700]);
set(gca,'fontsize',font_size);
set(gca,'FontName', 'Times New Roman');
set(gcf,'color','w');
```

```
contourf( (x/w-4.3), (y/w-1.452), Umag*1000, 20, 'edgecolor', 'none' ) ;
colormap jet
cb=colorbar;
axis([-3 3 -1 5]);
set(gca,'Ydir','normal')
caxis([0 90])
daspect auto
xlabel('{\itx/w_0 }','FontSize',font_size,'FontName', 'Times New Roman');
ylabel('{\ity/w_0 }','FontSize',font_size,'FontName', 'Times New Roman');
ylabel(cb,'{\itV}{ (mm/s)}','FontSize',font_size,'FontName', 'Times New Roman')

% Plot the pressure-field
figure (2)
set(2,'pos',[1000 250 800 700]);
set(gca,'fontsize',font_size);
set(gca,'FontName', 'Times New Roman');
set(gcf,'color','w');
contourf( (x/w-4.3), (y/w-1.452), P1, 20, 'edgecolor', 'none' ) ;
colormap jet
cb=colorbar;
axis([-3 3 -1 5]);
set(gca,'Ydir','normal')
caxis([-40 0])
daspect auto
xlabel('{\itx/w_0 }','FontSize',font_size,'FontName', 'Times New Roman');
ylabel('{\ity/w_0 }','FontSize',font_size,'FontName', 'Times New Roman');
ylabel(cb,'{\it\DeltaP}{ (Pa)}','FontSize',font_size,'FontName', 'Times New
Roman')

% Plot the pressure-field
figure (3)
set(3,'pos',[450 250 800 700]);
hold on
set(gca,'fontsize',font_size);
set(gca,'FontName', 'Times New Roman');
set(gcf,'color','w');
contourf( (x/w-4.3), (y/w-1.452), P2, 12,'edgecolor', 'none' ) ;
colormap jet(12)
cb=colorbar;
axis([-3 3 -1 5]);
xticks([-2 0 2])
set(gca,'Ydir','normal')
caxis([-5 0])
daspect auto
xlabel('{\itx/w_0_i }','FontSize',font_size,'FontName', 'Times New Roman');
ylabel('{\ity/w_0_i }','FontSize',font_size,'FontName', 'Times New Roman');
hold off
ylabel(cb,'{\it\DeltaP}{ (Pa)}','FontSize',font_size,'FontName', 'Times New
Roman')
```

Published with MATLAB® R2017a

Appendix A4: Matlab code for slot width estimation with time

```
%%%%%%%%%%%%%%%%%%%%%%%%%%%%%%%%%%%%%%%%%%%%%%%%%%%%%%%%%%%%%%%%%%%%%%%%%%%%%%%
% Estimate the slot width w.r.t build-up on side walls
% Who: Pavan Kamble
% April, 2019
% pkamble@ualberta.ca
%%%%%%%%%%%%%%%%%%%%%%%%%%%%%%%%%%%%%%%%%%%%%%%%%%%%%%%%%%%%%%%%%%%%%%%%%%%%%%%

clear all;
close all;
clc;
warning('off')
font_size=22;

%%Inputs nedded to be changed before executing the code
%Flow rate
%PeakProminence
%Y_entrance/exit and X_left/right
%load matlab data
%Path to DaVis images
%Scaling, no.of pixels corresponding to 1mm
density=1000;%Water density
% flow_rate=2.5*10^-7;%m3/s for 900 ml/hr
flow_rate=3.33*10^-7;%m3/s for 1200 ml/hr
% flow_rate=4.17*10^-7;%m3/s for 1500 ml/hr
depth=6.35;%slot depth in mm
height=80;%delta_z in mm
viscosity=0.00089274;% Water viscosity in Ns/m3 at 25 dec celcius
PeakProminence=75;%Peak threshold
y_entrance=519;%Slot entrance
y_exit=2048;%Slot exit
x_left=1;
x_right=2560;

%Load the matlab data from the Matlab Data Acquisition Toolbox 3.14
load('matlab_2nd_September.mat')
y=[DAQ_1_2nd_September.ai2];%Retrive the voltage
%Get maximum pressure drop value and location
[Max_volt_pressuredrop b]=max(DAQ_1_2nd_September.ai2),DAQ_1_2nd_September.Time;
x=duration(DAQ_1_2nd_September.Time,'Format','h');%Retrive the time
y=(y*17.2369)/6.5;%Convert voltage into pressure with pressure transducer
calibration
xnew=(0:b)'/360000;
xnew=xnew(1:b,1);
ynew=y(1:b,1);
n=29;
p = polyfit(xnew,ynew,n);%Fit the pressure drop curve
offset=p(1,n+1);
%Curve fitting
y_offset = polyval(p,xnew)-offset;%sets the pressure drop zero at the start of the
expt.

%To estimate Scaling time corresponding to 2.5 psi or 17.24 kPa
```

```
[Min_pressuredrop Min_location]=min(y_offset),xnew;
%If pressure drop is negative, makes it zero
if le(Min_pressuredrop,0)
    y_offset=y_offset-Min_pressuredrop;
    y_offset(1:Min_location)=0;
end
[Max_pressuredrop Max_location]=max(y_offset),xnew;
%Limit the pressure drop at 17kPa
if Max_pressuredrop>17
    locs_17=find(y_offset>17 & y_offset<17.1);
    y_offset(locs_17:size(y_offset,1))=NaN;
    xnew(locs_17:size(y_offset,1))=NaN;
    [Max_pressuredrop Max_location]=max(y_offset),xnew;
end
Scaling_time=xnew(Max_location(1,1));%Scaling time corresponding to 17kPa
last_image_no=fix(((Max_location-1)/30000)+1);%Gets last image number in the expt
based on scaling time
fprintf('The scaling time is %5.4f hrs\n',Scaling_time)%Display the scaling time

j=1;%loop the code from image 1 to the last image
for im=1:last_image_no

%Path for the raw images
path =
'C:\MyProjects8.3\E2_007_Straight_1200mlph_2nd_September\2nd_September_19\';
filenameim=['B00' num2str(im,'%03i') '.im7'];
FV = filenameim;
v = loadvec([path FV]);

count=1;

%Runs the code from slot entrance to exit to get the slot width for a
%single image
for i=y_entrance:y_exit

%Adds a small number to the intesity count of raw image
intensitynew=v.w(:,i)+(linspace(0, 1, length(v.w(:,i)))*1E-3)';
position=1:length(v.w(:,i));%intensity vecotr position
step_size=v.x(1,2)-v.x(1,1);
Slot_length=v.y(y_exit)-v.y(y_entrance);

%Gets the slot width at half peak prominence
[pksnew,locsnew,wdthsnew,promsnew]=findpeaks(intensitynew,position,'MinPeakPromine
nce',PeakProminence);

%Checks for any duplicates peaks
anyDuplicates = ~all(diff(sort(promsnew(promsnew ~= 0))));
locsnew=locsnew(find(promsnew==max(promsnew)));
pksnew=pksnew(find(promsnew==max(promsnew)));

if anyDuplicates==1
    wdthsnew=sum(wdthsnew);
else
    wdthsnew=max(wdthsnew);
end

if ~isempty(pksnew)==0
```

```
    wdthsnew=0;
    promsnew=0;
    pksnew=0;
    x_slot_left=0;
else
%Interpolation to get slot width at a specific peak prominence e.g. at 80% of the
%peak prominence instead of half prominence
fnInterpL=@(pksnew,locsnew,wdthsnew)
interp1(intensitynew(1:locsnew),1:locsnew,0.5*max(promsnew)+(max(pksnew)-
max(promsnew)));
fnInterpH=@(pksnew,locsnew,wdthsnew)
interp1(intensitynew(locsnew:2560),locsnew:2560,0.5*max(promsnew)+(max(pksnew)-
max(promsnew)));
% w50=[arrayfun(fnInterpH,pksnew,locsnew.',wdthsnew.')-
arrayfun(fnInterpL,pksnew,locsnew.',wdthsnew.') ]*step_size;
x_slot_left=(fix(arrayfun(fnInterpL,pksnew,locsnew.',wdthsnew.')))*step_size;
end

locsnew=v.x(locsnew);
wdthsnew=wdthsnew*step_size;

width_arrayki(count,1)=wdthsnew;
width_all(count,im)=wdthsnew;
x_slot_left_array(count,im)=x_slot_left;
promsnew_array(count,im)=max(promsnew);
pksnew_array(count,im)=max(pksnew);
Min_Proms(count,im)=max(pksnew)-max(promsnew);
anyDuplicates_array(count,im)=anyDuplicates;

Growth_array_verti(count,im)=abs((width_all(count,1)-width_all(count,im))/2);
Growth_array_horri(count,im)=x_slot_left_array(count,1)+abs((width_all(count,1)-
width_all(count,im))/2);

count=count+1;
end

%Avergaing the width for a single image from slot entrance to slot exit
avg_width=mean(width_arrayki(:,1));
%Stores width in an array
avg_width_array(j,1)=avg_width;

%Get pressure drop value at certain time i.e.every 5 minutes
pressure(j,1)=y_offset((1+(30000*(im-1))),1);
time(j,1)=(im-1)*(5/60);%time at every 5 minutes
pressure(last_image_no,1)=y_offset(Max_location,1);
time(last_image_no,1)=Max_location/(3600*100);
diameter_array(j,1)=(2*depth*avg_width_array(j,1))/(depth+avg_width_array(j,1));%H
ydraulic diameter
AR(j,1)=depth/avg_width_array(j,1);%Aspect ratio
velocity=flow_rate/(depth*avg_width*10^-6);%Avg.velocity to calculate the loss
coefficient
velocity_array(j,1)=velocity;
Re(j,1)=(density*velocity_array(j,1)*diameter_array(j,1)*10^-
3)/viscosity;%Reynolds number
L=25*10^-3;%slot length
loss_coe_array(j,1)=(((pressure(j,1)*1000/(density*9.81))+height*10^-
3)/((velocity_array(j,1)*velocity_array(j,1))/(2*9.81)));
```

```
j=j+1;
end

%Linear curve fitting to obtain the growth rate
size=size(nonzeros(avg_width_array),1);
avg_width_array_no_zeros=nonzeros(avg_width_array);
p_slot_width = polyfit(time(1:size,1),avg_width_array_no_zeros,1);
slot_width_fit=polyval(p_slot_width,time(1:size,1));
Growth_rate_slot_width=abs(p_slot_width(1))/2;
fprintf('The average growth rate is %5.4f mm/hr\n',Growth_rate_slot_width)

%Compute  the coefficient of determination or r-square
resid=avg_width_array_no_zeros-slot_width_fit;
SSresid=sum(resid.^2);
SStotal=(length(avg_width_array_no_zeros)-1)*var(avg_width_array_no_zeros);
rsq=(1-SSresid/SStotal)*100;
fprintf('The r-square is %5.2f %%\n',rsq)

%Plot pressure drop vs time
figure(4)
set(4,'pos',[100 200 800 700]);
plot(xnew,y_offset,'k','LineWidth',1)
set(gca,'fontsize',font_size)
set(gca,'FontName', 'Times New Roman');
ylim([-2 18])
% xlim([0 5])
xlabel('{\itt} {(hrs)}','FontSize',font_size,'FontName', 'Times New Roman');
ylabel('{\it\DeltaP} {(kPa)} ','FontSize',font_size,'FontName', 'Times New
Roman');

%Plot reduction in slot width
figure(5)
set(5,'pos',[100 200 800 700]);
plot(time,avg_width_array/avg_width_array(1,1),'k-o')
xlabel('{\itt} {(hrs)} ','FontSize',font_size,'FontName', 'Times New Roman');
ylabel('{\itw/w_0}','FontSize',font_size,'FontName', 'Times New Roman');
set(gca,'fontsize',font_size)
set(gca,'FontName', 'Times New Roman')

%Plot reduction in slot width and linear fit
figure(6)
set(6,'pos',[1000 200 800 700]);
plot(time,avg_width_array/avg_width_array(1,1),'k-o')
hold on
plot(time(1:size,1),slot_width_fit,'b-o')
xlabel('{\itt} {(hrs)}','FontSize',font_size,'FontName', 'Times New Roman');
ylabel('{\itw/w_0}','FontSize',font_size,'FontName', 'Times New Roman');
set(gca,'fontsize',font_size)
set(gca,'FontName', 'Times New Roman')

%Plot K vs Re
figure(10)
set(10,'pos',[1000 200 800 700]);
loglog(Re,loss_coe_array,'b-o')
xlabel('{\itRe} ','FontSize',font_size,'FontName', 'Times New Roman');
ylabel('{\itK} ','FontSize',font_size,'FontName', 'Times New Roman');
set(gca,'fontsize',font_size)
```

```
set(gca,'FontName', 'Times New Roman')
hold off

%Plot K vs AR
figure(11)
set(11,'pos',[100 200 800 700]);
plot(AR,loss_coe_array,'b-o');
xlabel('{\itAR} ','FontSize',font_size,'FontName', 'Times New Roman');
ylabel('{\itK} ','FontSize',font_size,'FontName', 'Times New Roman');
set(gca,'fontsize',font_size)
set(gca,'FontName', 'Times New Roman')
hold off

%Plot delta_p vs AR
figure(12)
set(12,'pos',[1000 200 800 700]);
plot(AR,pressure,'r-o')
xlabel('{\itAR} ','FontSize',font_size,'FontName', 'Times New Roman');
ylabel('{\it\DeltaP} {(kPa)}','FontSize',font_size,'FontName', 'Times New Roman');
set(gca,'fontsize',font_size)
set(gca,'FontName', 'Times New Roman')

%Display binarized image with intensity count threshold < 95
v.x=(v.x+1.28)/0.8877;  %Non-dimensionalize with initial width (width at t=0)
v.y=(v.y+2.1)/0.8877;   %Non-dimensionalize with initial width (width at t=0)
v.w=v.w(:,:);

for ki = 1 : 2560

   for kj = 1 : 2048
       if v.w(ki,kj)>95
           v.w(ki,kj) = 1;
       else
           v.w(ki,kj) = 0;
       end
   end
end

figure(17);
set(17,'pos',[100 200 800 700]);
showf(v);
set(gca,'fontsize',font_size);
set(gca,'FontName', 'Times New Roman');
xlabel('{\itx/w_0 }','FontSize',font_size,'FontName', 'Times New Roman');
ylabel('{\ity/w_0 }','FontSize',font_size,'FontName', 'Times New Roman');
```

Published with MATLAB® R2017a

Appendix A5: Data repeatability

(a)

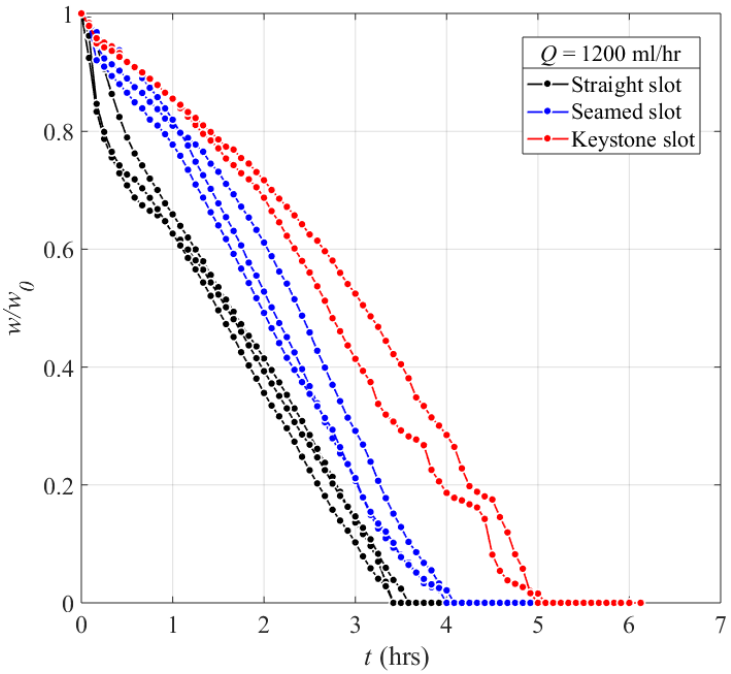

(b)

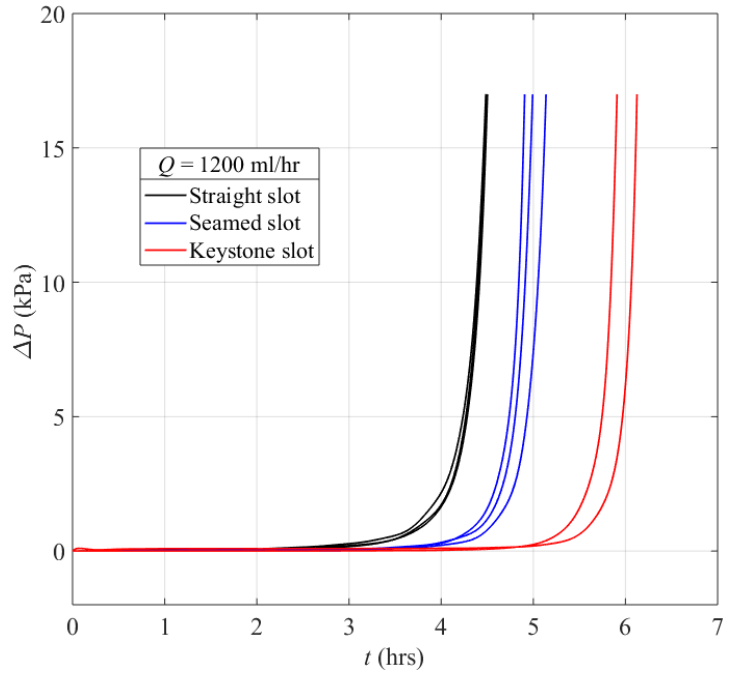

Figure A5: Repeatability of (a) Change in slot width and (b) pressure drop for straight, seamed and keystone design at Q = 1200 ml/hr

(a)

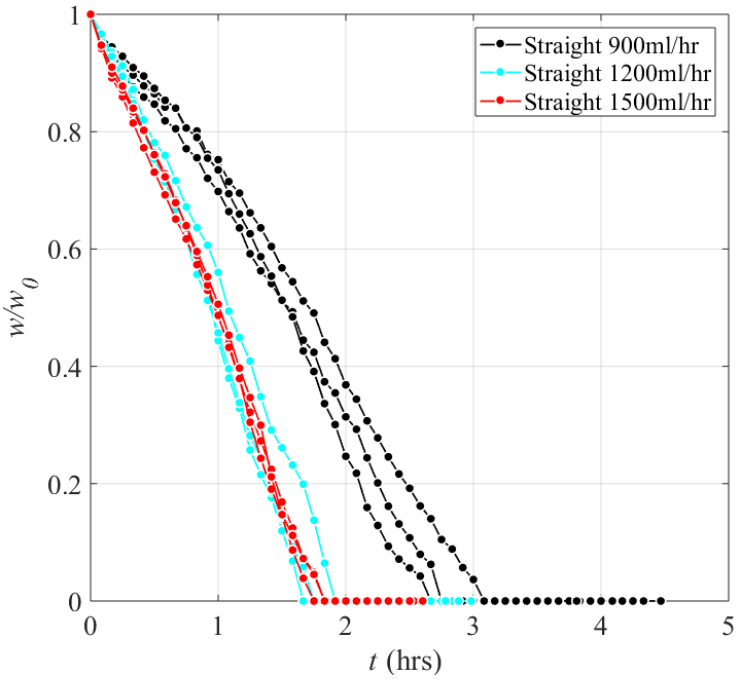

(b)

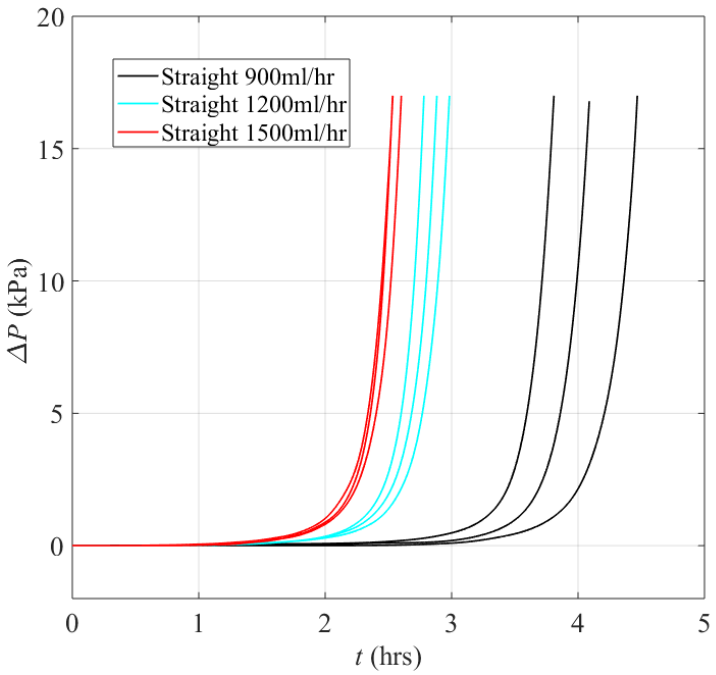

Figure A5: Repeatability of (a) Change in slot width and (b) pressure drop for straight slot at Q = 900, 1200 and 1500 ml/hr

(a)

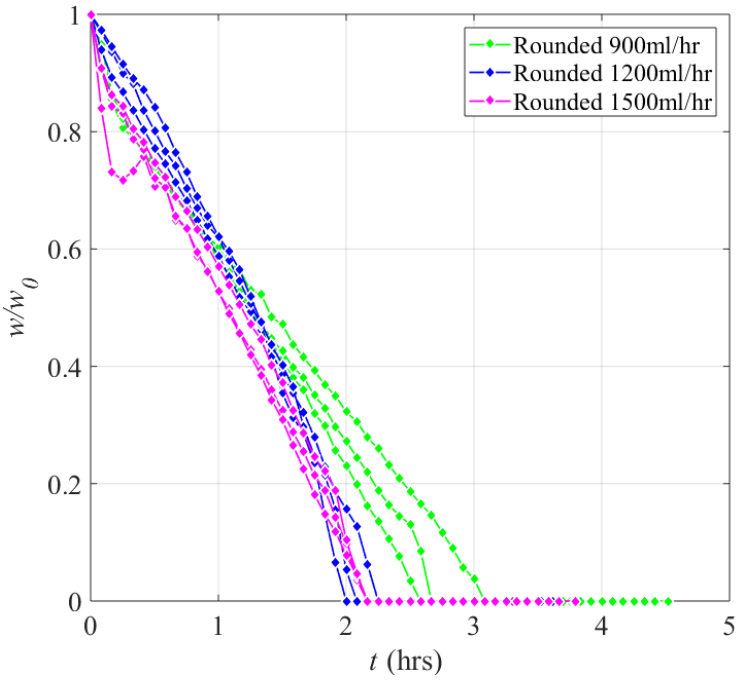

(b)

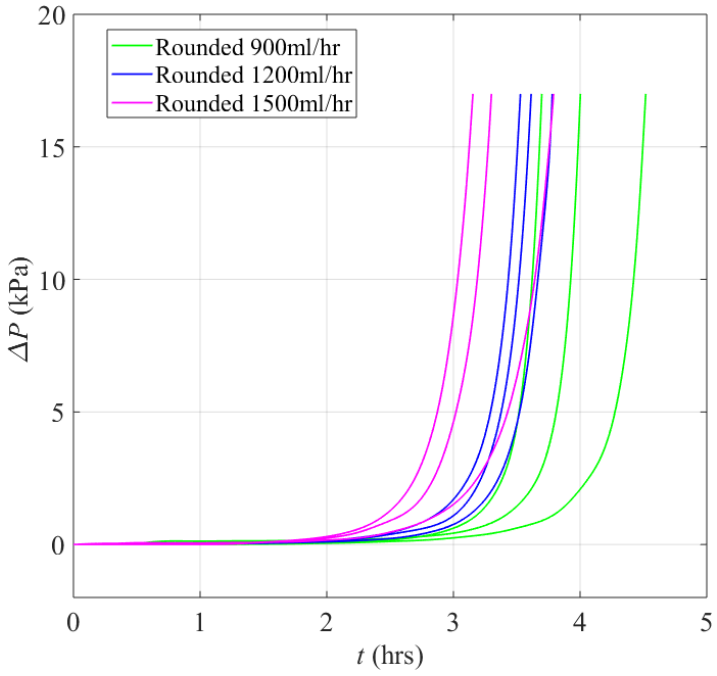

Figure A5: Repeatability of (a) Change in slot width and (b) pressure drop for rounded slot at Q = 900, 1200 and 1500 ml/hr

Appendix A6: Slot width comparison of straight slot geometries from Chapter-4 and Chapter-5

Figure A5 shows the slot width comparison along the length for straight slot geometries of Chapter-4 and Chapter-5. Where, w is the local slot width and w_{oi} is the slot width at the entrance. The slot width in straight slot geometry of Chapter-5 is consistence along the length. Whereas, the slot width in straight slot geometry of Chapter-4 is wider at slot entrance and decreases along the slot length.

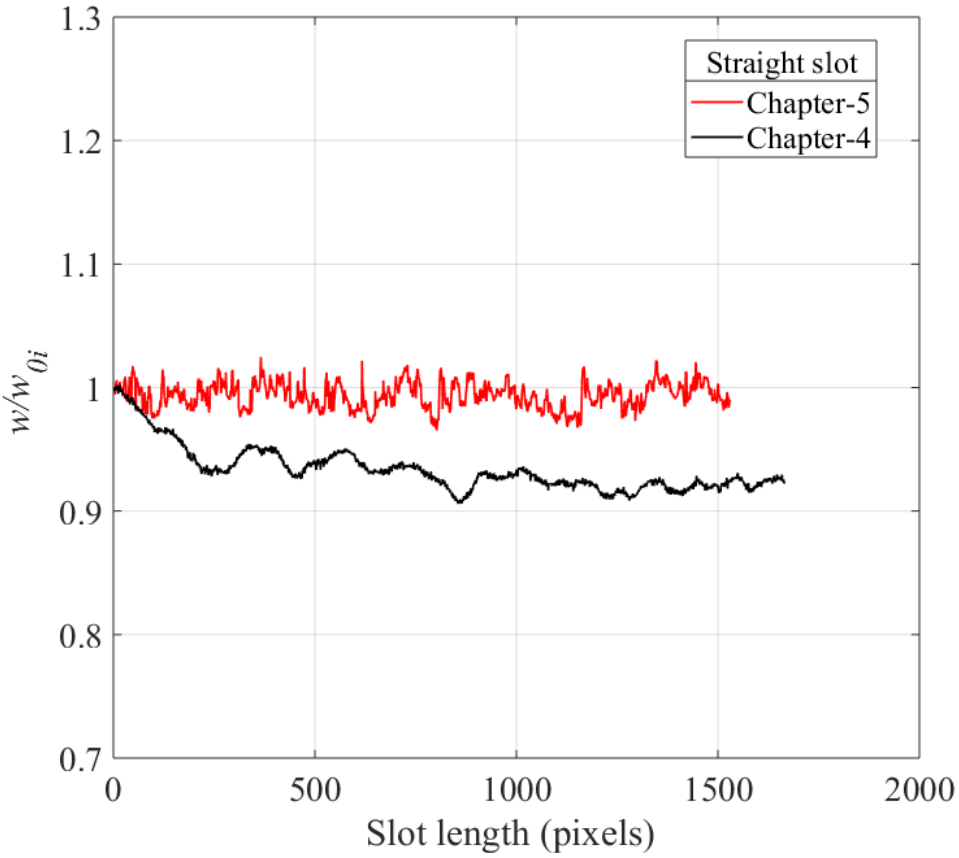

Figure A6: Slot width comparison along the length for straight slot geometry of Chapter-4 and Chapter-5, where w is local slot width and w_{oi} is the slot width at the entrance

Appendix A7: Shadow images for the straight and rounded design at 900 ml/hr

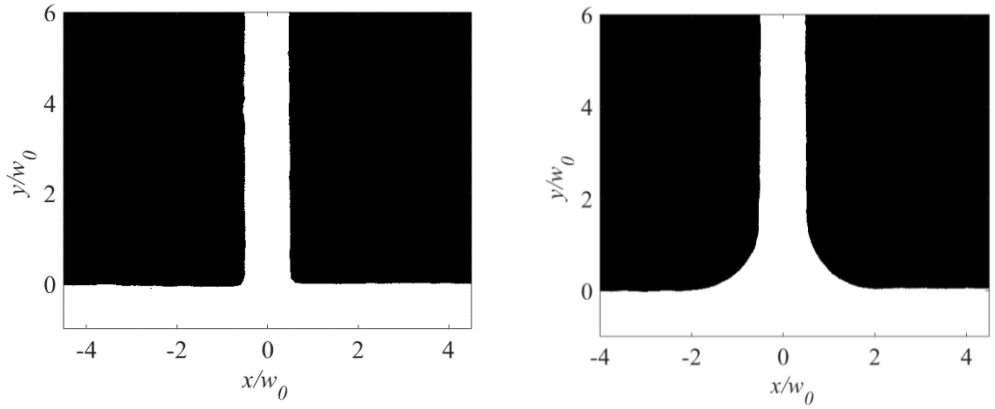

(a) t = 0 hrs

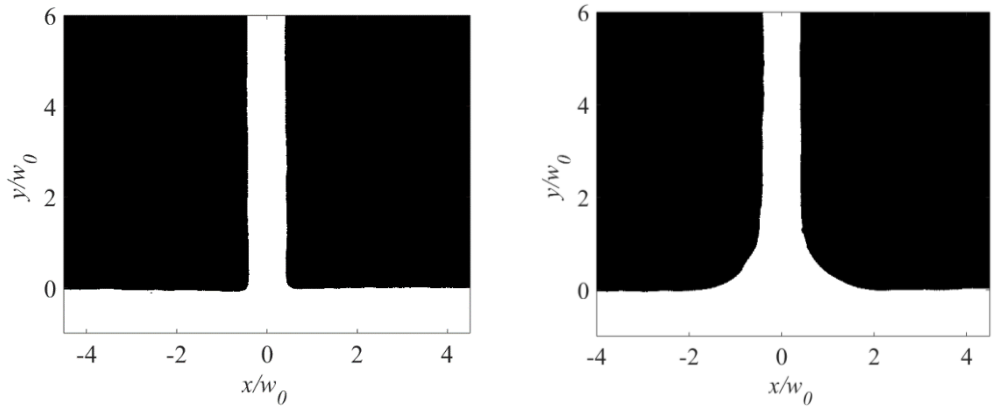

(b) t = 0.5 hrs

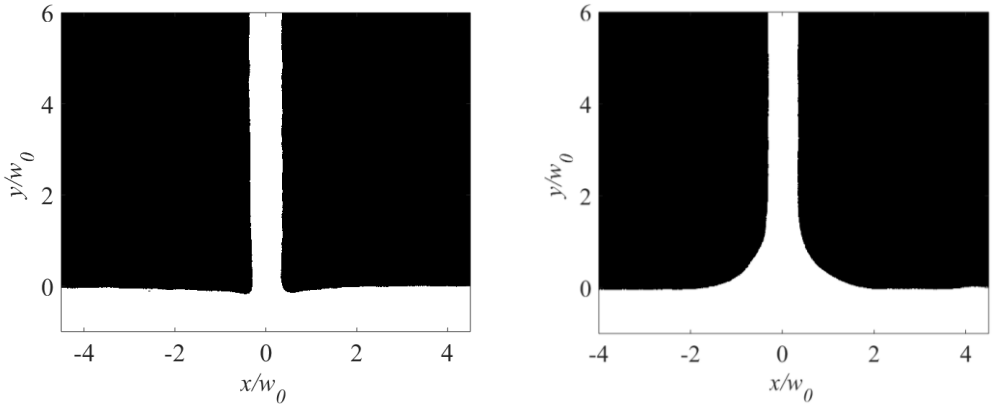

(c) t = 1 hrs

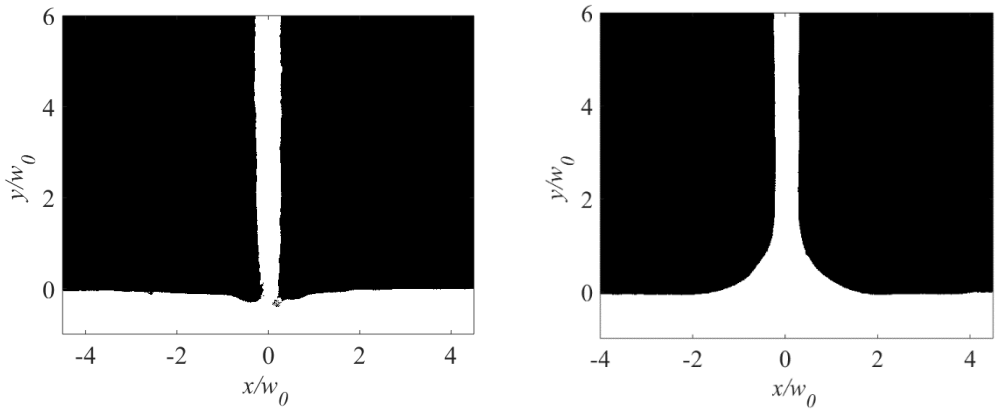

(d) t = 1.5 hrs

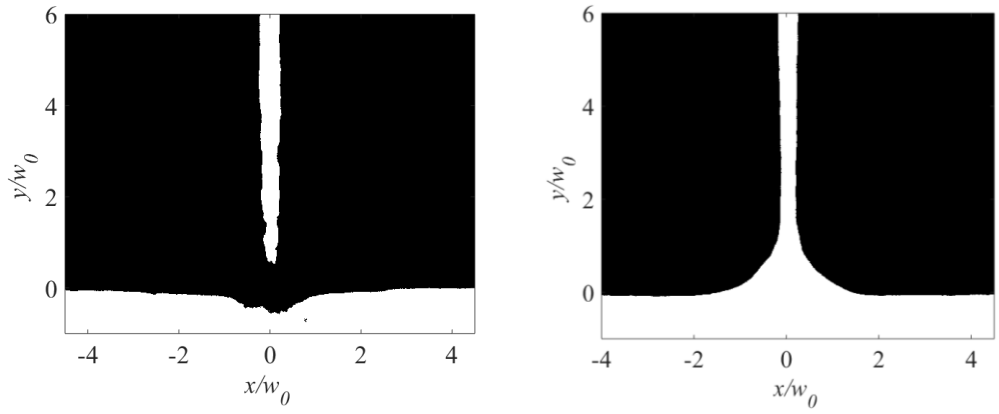

(e) t = 2 hrs

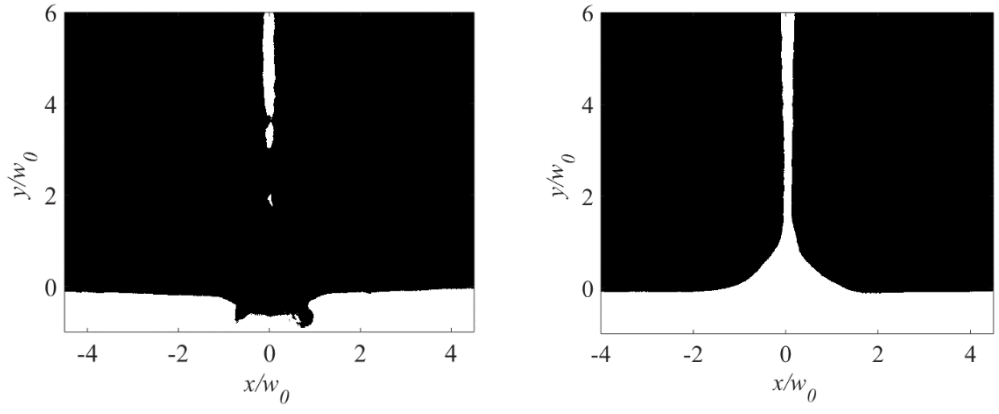

(f) t = 2.5 hrs

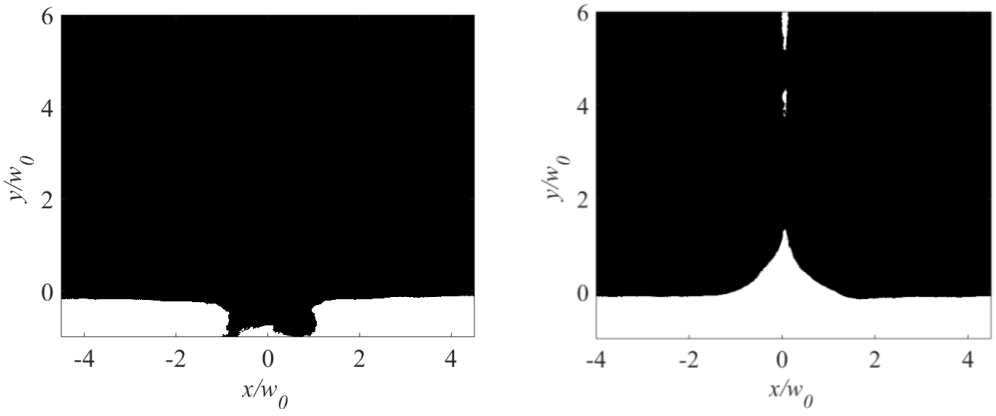

(g) t = 3 hrs

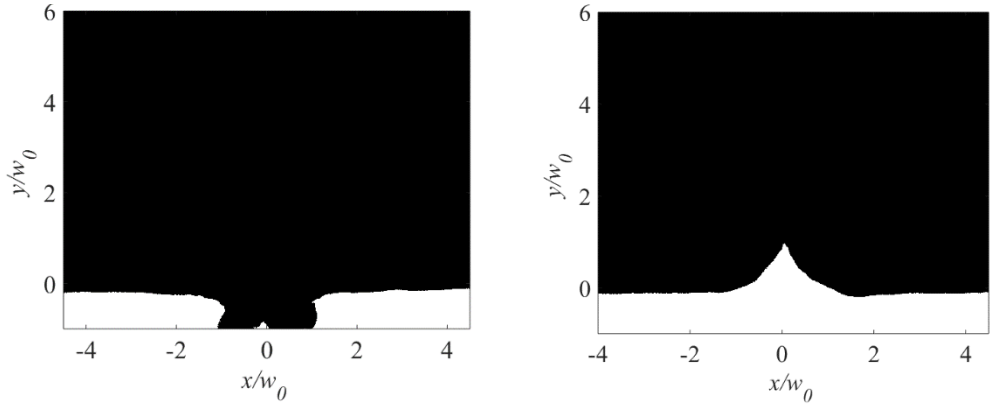

(h) t = 3.5 hrs

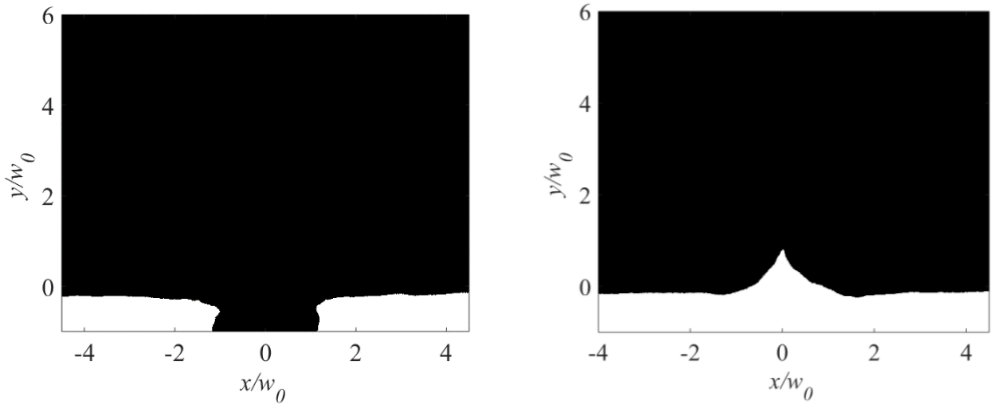

(i) t = 4 hrs

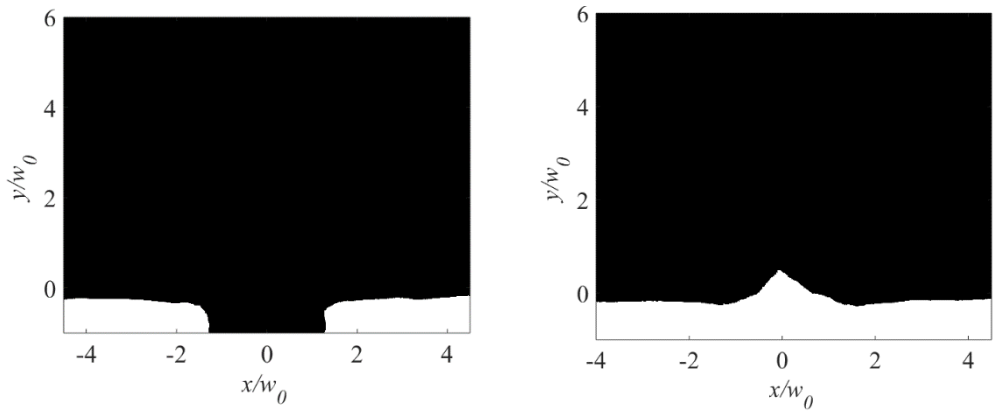

(j) t = 4.5 hrs

Figure A7: Calcium carbonate growth in the straight and rounded slot for Q = 900ml/hr, (a)-(j) at intervals in the experiment

Appendix A8: Shadow images for the straight and rounded design at 1200 ml/hr

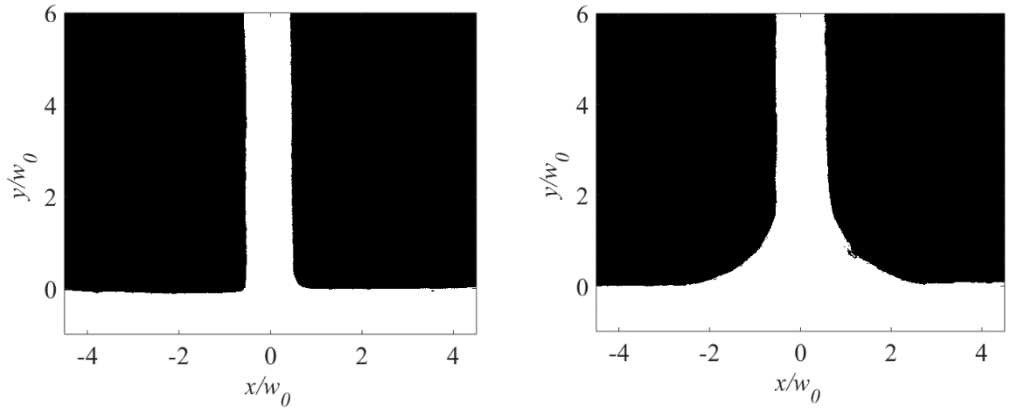

(a) t = 0 hrs

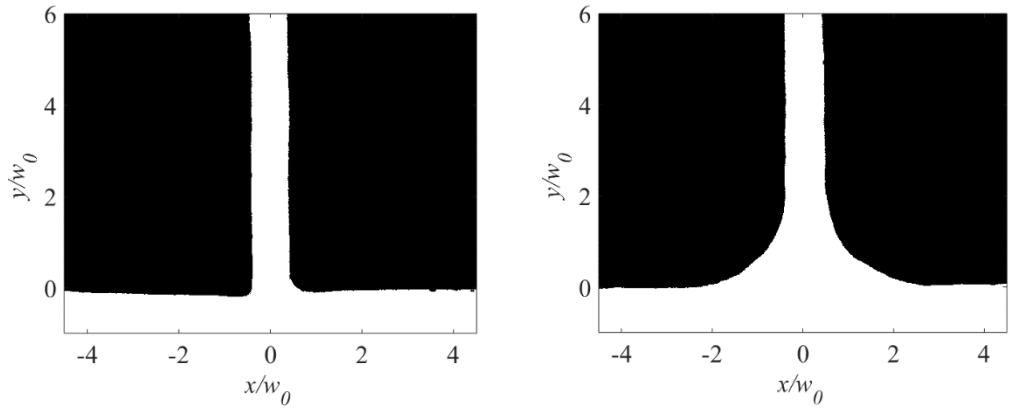

(b) t = 0.5 hrs

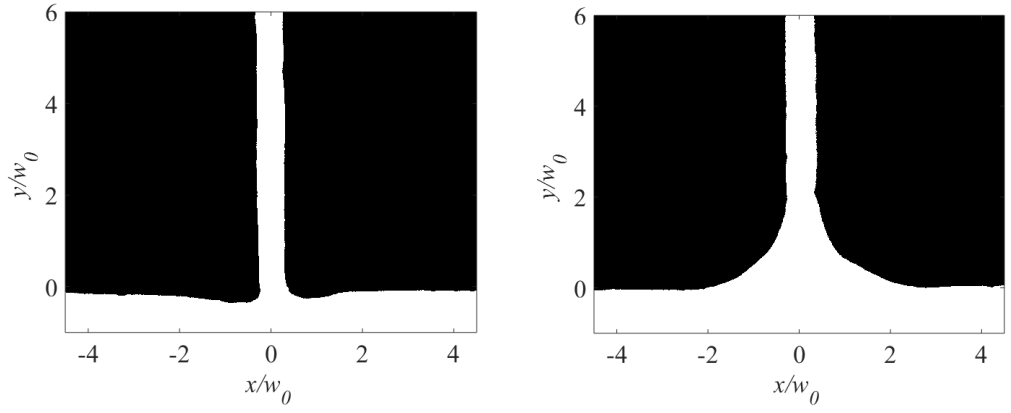

(c) t = 1 hrs

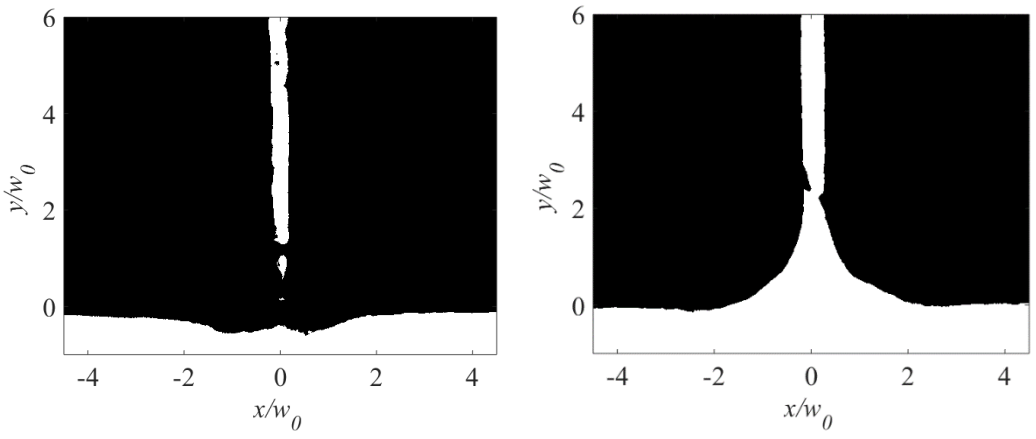

(d) t = 1.5 hrs

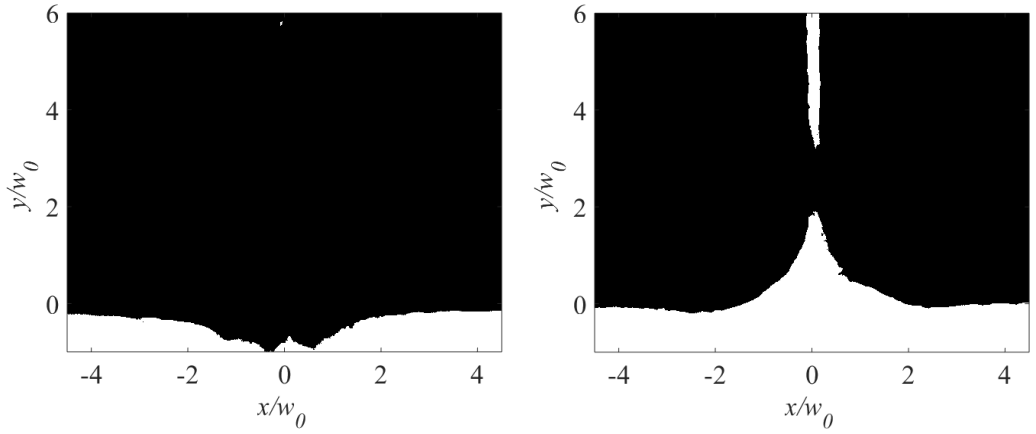

(e) t = 2 hrs

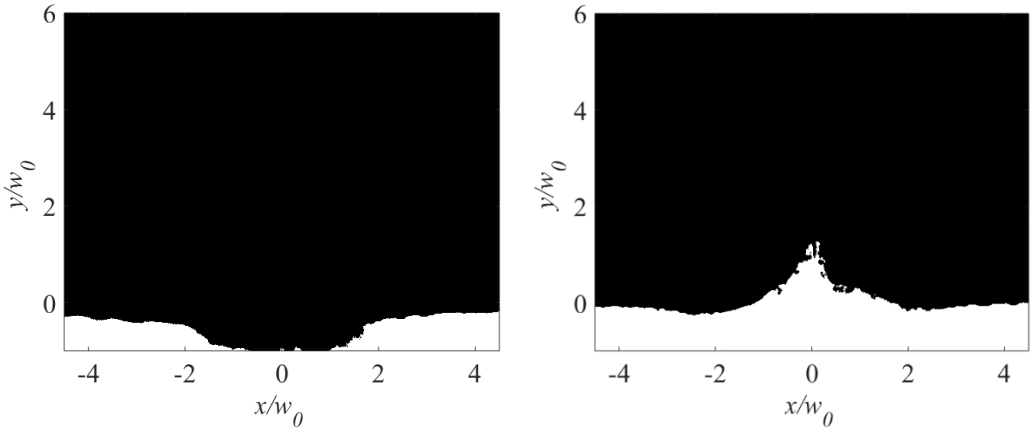

(f) t = 2.5 hrs

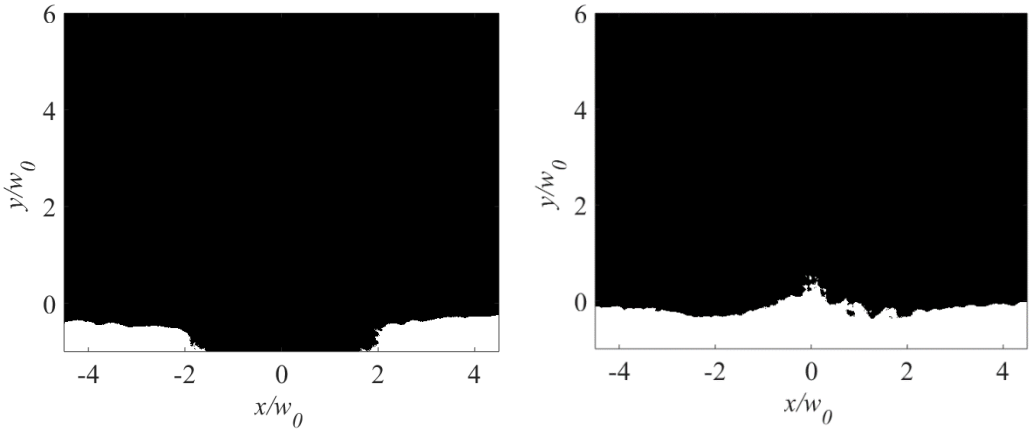

(g) t = 3 hrs

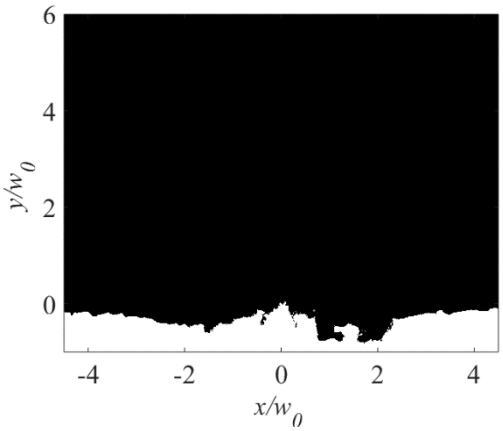

(h) t = 3.7 hrs

Figure A8: Calcium carbonate growth in the straight and rounded slot for Q = 1200ml/hr, (a)-(h) at intervals in the experiment

Appendix A9: Straight slot drawing

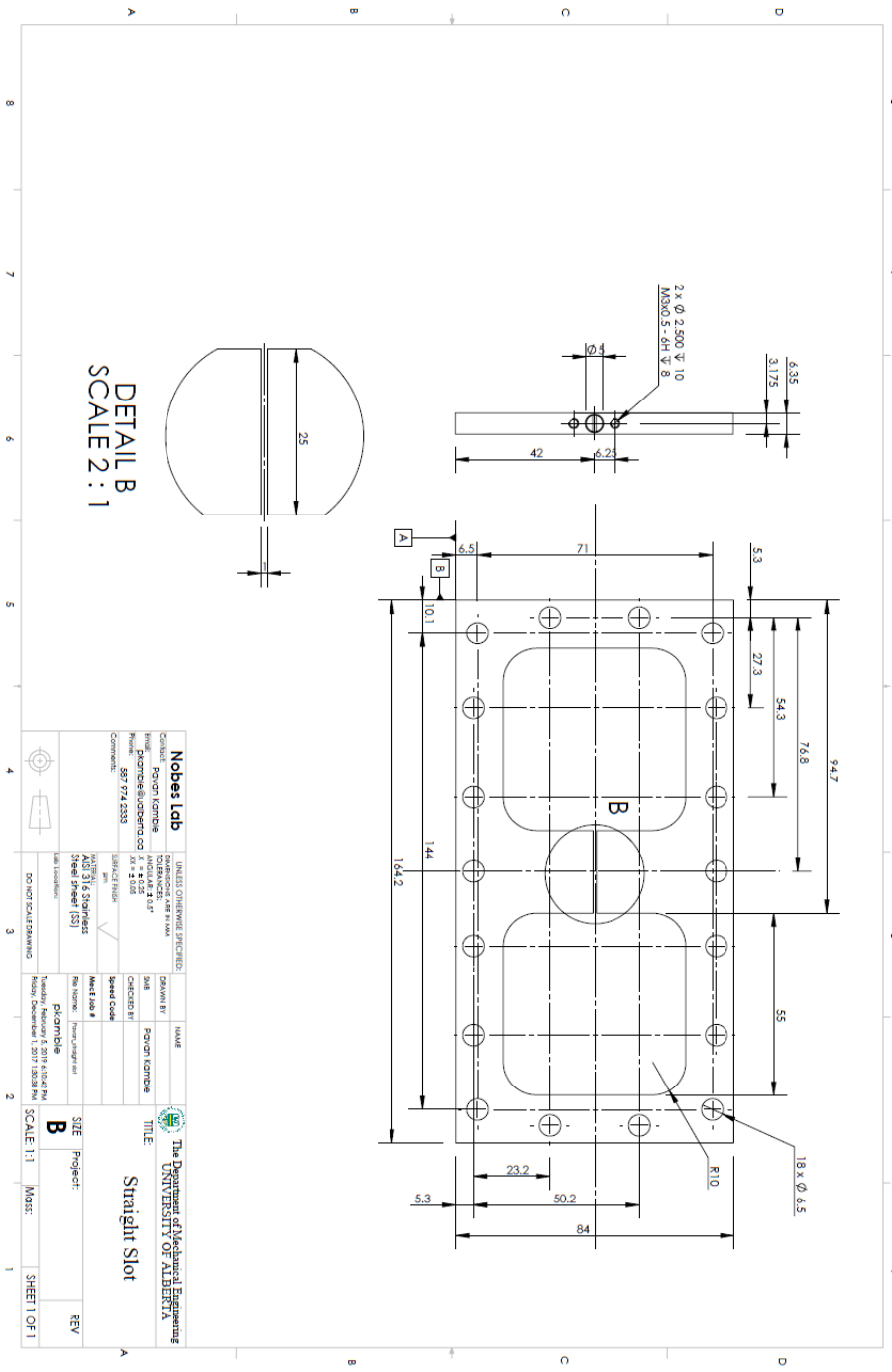

Figure A9: Straight slot drawing

Appendix A10: Seamed slot drawing

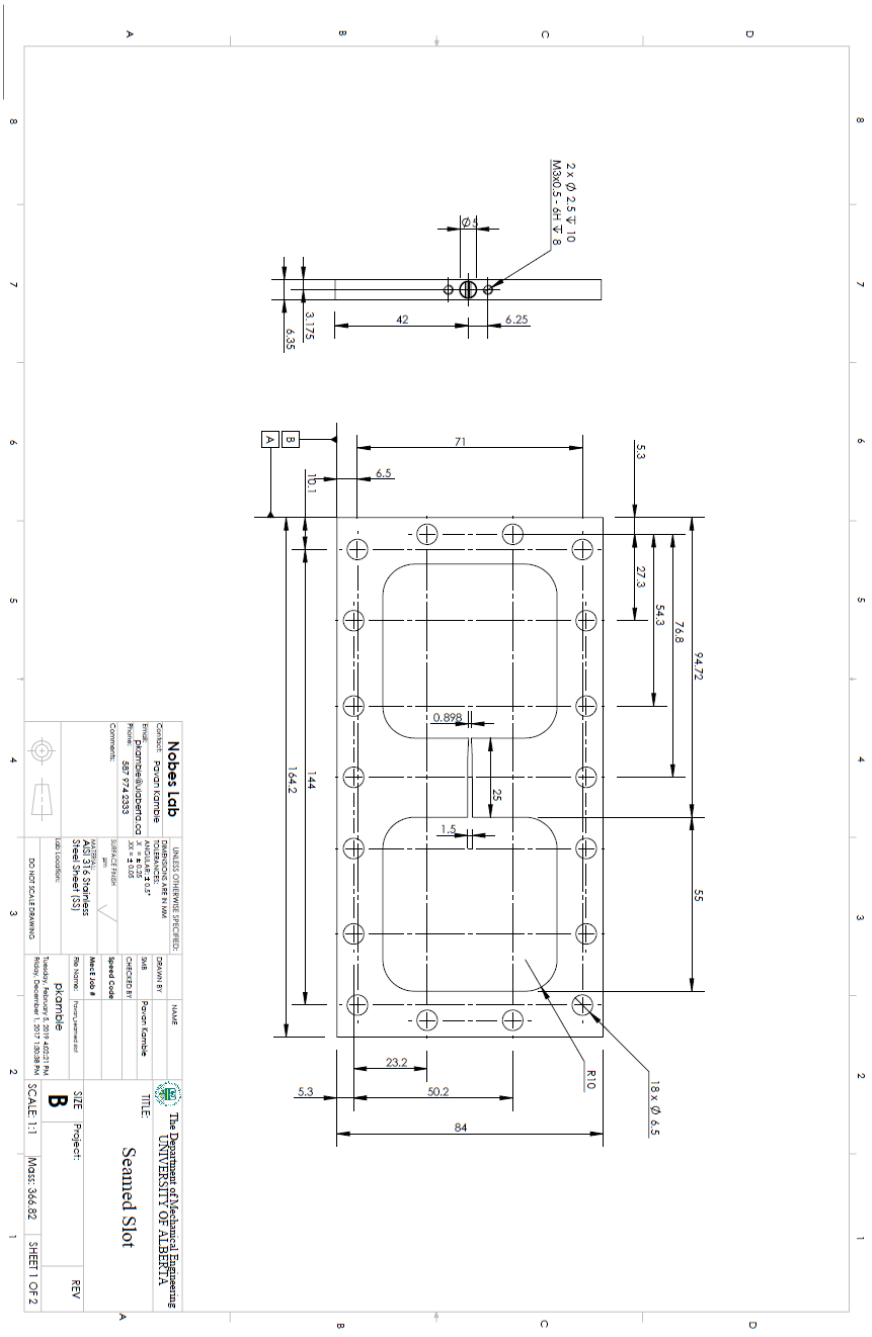

Figure A10: Seamed slot drawing

Appendix A11: Keystone slot drawing

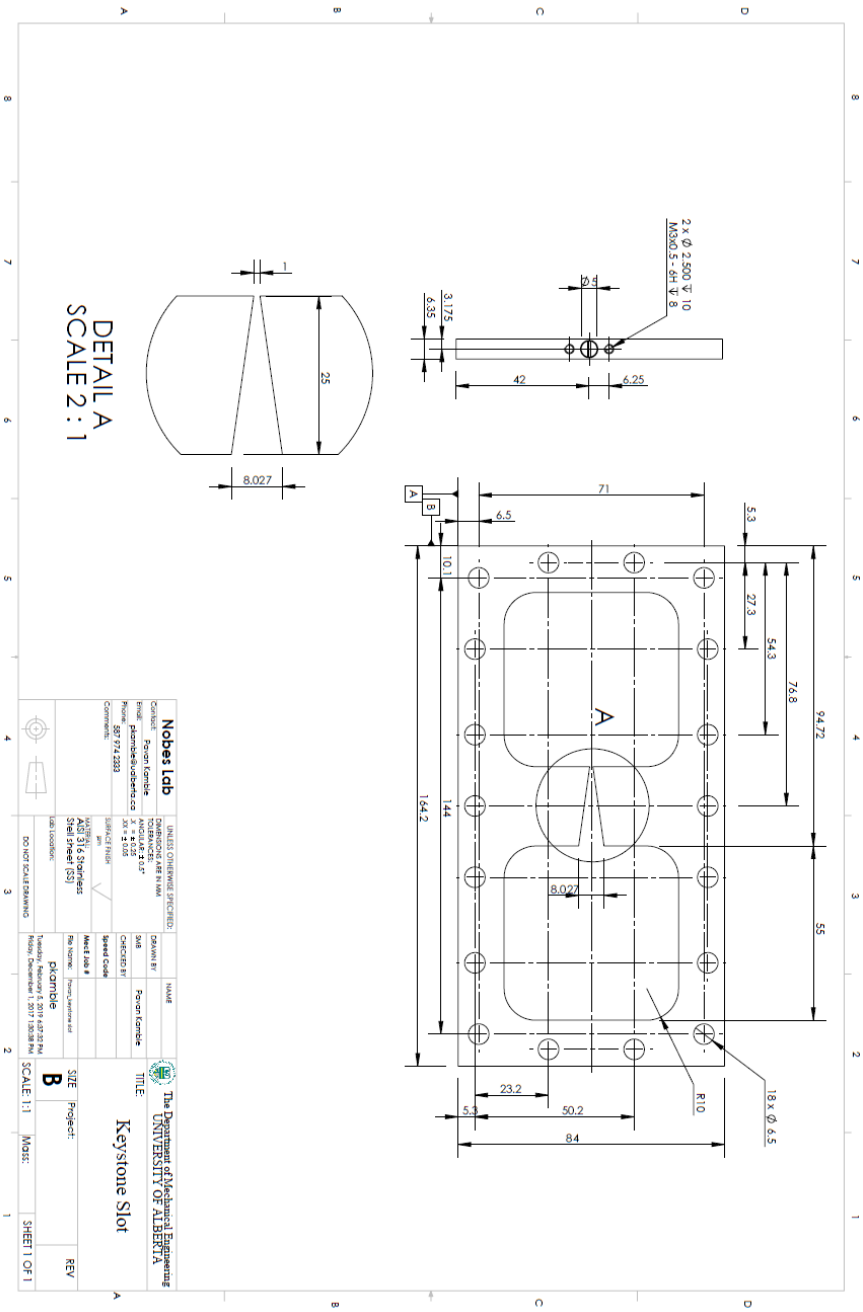

Figure A11: Keystone slot drawing

Appendix A12: Rounded slot drawing

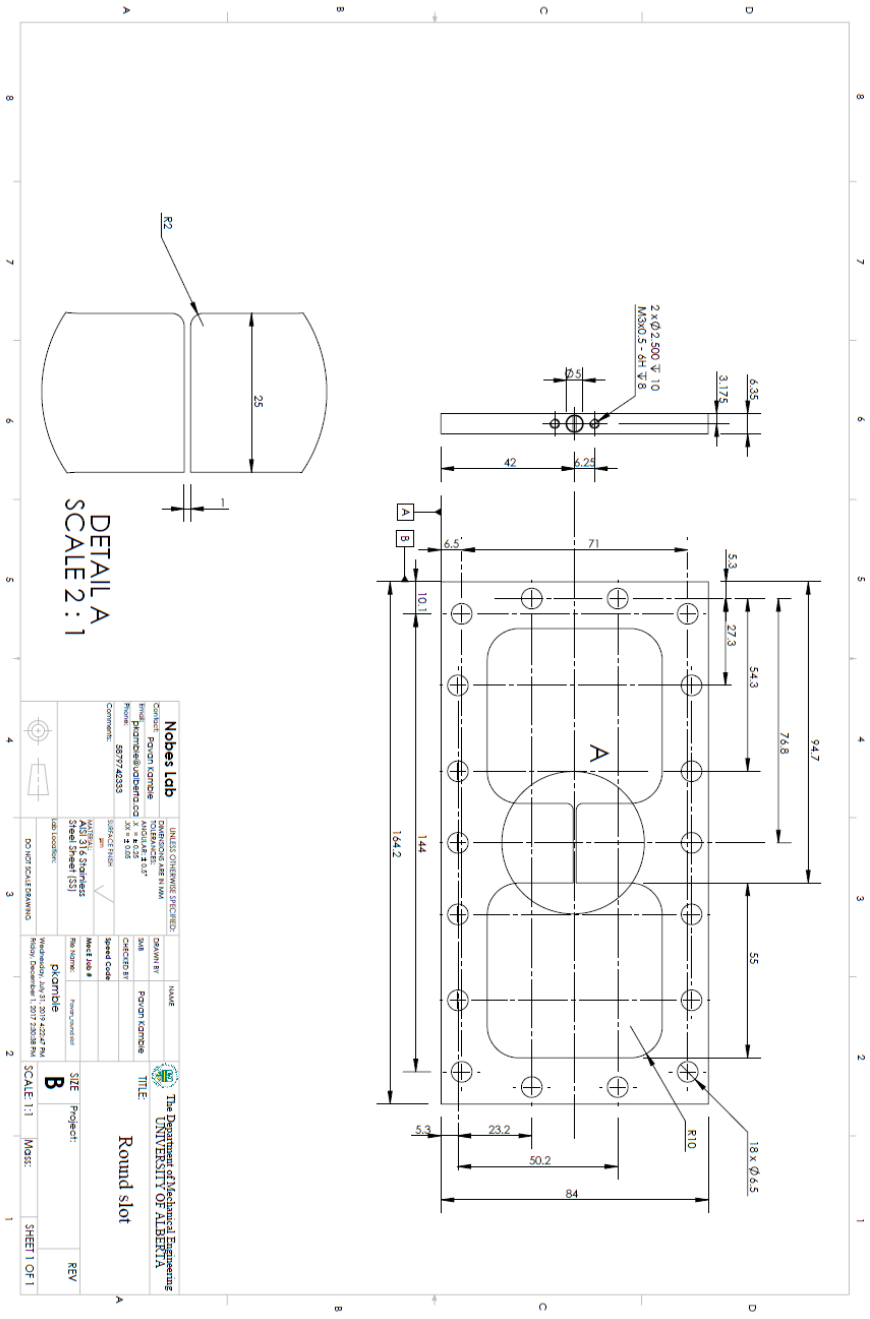

Figure A12: Rounded slot drawing